Annaclaudia Montanino

Estimation of hip contact forces by means of three musculoskeletal models of the lower limb

Tesi di Laurea Magistrale

Relatore: Prof. Nicola Petrone
Correlatore: Dr. Luca Modenese

Università degli Studi di Padova

Dipartimento di Ingegneria dell'Informazione

Corso di Laurea Magistrale in Bioingegneria

Aprile 2015

Contents

A papi e Vitty.

Abstract

Musculoskeletal models are numerical tools that allow a biomechanical investigation of human locomotion with many possible aims: analyzing sports performances, simulating the effects of orthopedic surgical procedures, etc. For these models to be reliable – and hence to be used in clinical practise– a validation step is necessary.

The purpose of this study was to assess the performances of three musculoskeletal models (gait2392, LLLM and LLLM2) in predicting magnitude and direction of hip joint contact forces (HCFs) – resultant vector of all the forces acting at the hip joint centre– during the dynamic simulation of two daily living activities: level walking and stairs climbing.

At a qualitative level, predicted muscle activations from both activities have been compared with electromyographic activation recorded during the experimental session of one subject (SM7). Moreover, a quantitative direct comparison has been performed to assess predicted HCFs against in vivo measurements from instrumented prostheses of HIP98 dataset (gold standard). To draw this comparison, complete dynamics simulation were run for three subjects (SF1, SM4 and SM7) each performing 10 walking trials and 10 stair climbing trials.

This thesis consists of: an Introduction (Chapter 1) in which a general overview of musculoskeletal models and more specifically of the three models under study is provided; the Experimental chapter (Chapter 2) where the data collection and processing are described; the Numerical Methods chapter (Chapter 3) in which all the steps followed to run the dynamic simulation are presented; the Results and Discussion chapters (Chapters 4 and 5) that include all the subjects' results respectively for the walking and stairs climbing tasks; and finally Chapter 6 where conclusions that can be drawn from the study are summarized and directions for future research directions are presented.

Chapter 1

Introduction

1.1 Musculoskeletal models

Several models of the lower extremity as a musculoskeletal system have been previously developed to investigate human locomotion. What all these models have in common is the way of representing the human musculoskeletal system as a multibody system made of rigid bodies (the bones) linked by mechanically defined joints (spherical, hinge, etc) that are spanned by line-actuators (the musculotendon units).

Numerous are the applicative aims of musculoskeletal models. In [Anderson and Pandy,1999], for example, a musculoskeletal model was developed to investigate on sports performances and in particular to calculate the pattern of muscle excitations that produces a maximal vertical jump. Another possible application is the investigation of if-then scenarios to address clinical and surgical questions such as in [Delp,1990] where the effects of a tendon-transfer and lengthening procedure were analyzed.

These models, in combination with dynamics simulations, can also be a useful tool for the estimation of internal loads acting on the musculoskeletal system. Bringing as example the hip joint, these loads are represented by the hip joint contact forces (HCFs): magnitudes and orientation of HCFs need to be known to test and optimize the design of implants and it was with this purpose that they have been measured with instrumented prostheses by [Bergmann,2001]. However, when studying processes such as bone fracture or bone remodelling, another important contribution to the loading of the bone structure is given by the hardly measurable set of muscle forces. This quantity can be estimated using musculoskeletal models. For example, it has recently been shown in [Phillips,2015] how the complex problem of bone adaptation can be simulated knowing the loads (predicted using a muscu-

loskeletal model) acting on the femoral bone structure, and using a bone-adaptation algorithm. Musculoskeletal models in the future could, therefore, also be used to plan a subject-specific physical activity with the aim of promoting bone formation in a desired area of the bone to prevent its fracture.

1.2   The gait2392 Model

The original gait2392 model [Delp,1990] shown in Figure 1.1 is a 23 degrees of freedom musculoskeletal model including both lower limbs and the head and torso which are considered as a single segment. The model features 92 muscolotendon units representative of 76 muscles: all main leg muscles are included and also few muscles spanning from the limbs to the torso as *erector spinae*, *Internal* and *external oblique* of the abdomen. The unscaled version of the model is representative of a subject $1.8m$ tall and with a mass of $75.16Kg$.

For our study, the unilateral and lower limb portion of the original model was used: to implement this simplification, the torso segment and connected muscles were eliminated. The resulting unilateral lower limb model (Figure 1.2)– **that from now on will be referred to as gait2392 model**– consists of seven rigid body segments: pelvis, femur, patella, tibia/fibula, talus, foot and toes. All segments are defined by an embedded reference frame.
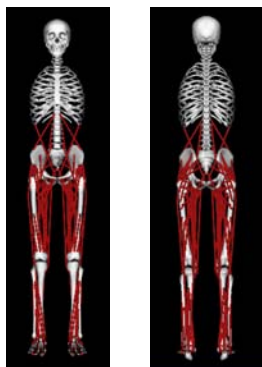

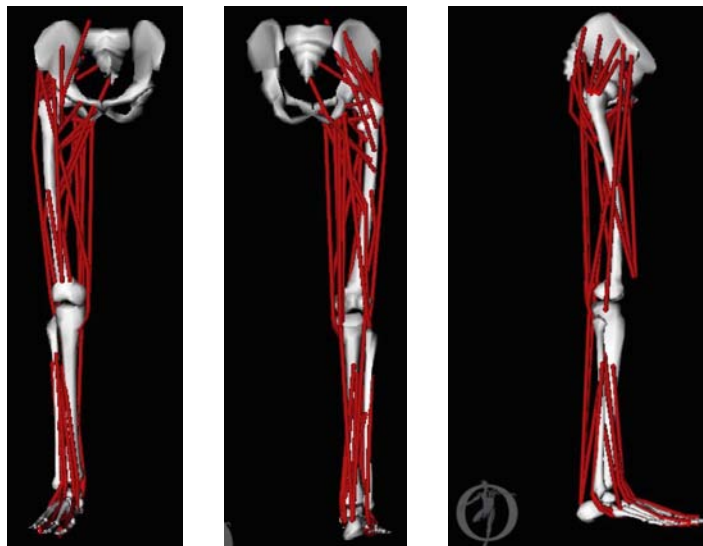**Figure 1.1:**   Original gait2392 model

Figure 1.2: Frontal, posterior and lateral view of gait2392 model i.e. unilateral lower limb portion included in the original gait2392

The gait2392 model includes five joints. The hip joint is modelled as a ball-socket joint thus accounting for all three anatomical rotation (ab-adduction, intra-

extra rotation and flexion-extension). The knee joint, instead, has been modeled as in [Yamaguchi,1989]: this single-degree-of-freedom model describes the tibio-femoral and patello-femoral kinematics in the sagittal plane and the patellar lever mechanism, all specified as functions of the knee flexion-extension angle. However, in the model the patella [Delp,1990] has been removed to avoid kinematic constraints and replaced with appropriate muscle paths at high flexion angles. The ankle, subtalar and metatarsophageal joints are characterized as revolute joints with axes specified in [Inman,1976]. In the default configuration pelvis reference frame and ground reference frame are aligned, thus resulting in zero pelvic tilt.

The muscle paths (lines of action) are defined based on anatomical landmarks on the bone surface models. Each musculotendon actuator is represented either as a single straight line segment spanning from the origin to the insertion (ex. *soleus* in Figure 1.3.a) or includes via-points to better represent the muscle path (ex. *peroneus longus* in Figure 1.3.b) Conditional via-point that become active at a certain range of motion have also been defined for some muscles, preventing it from passing through the bone.
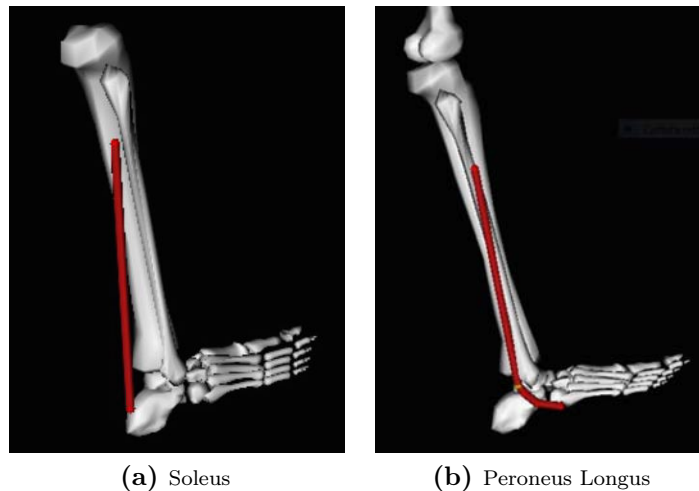

(a) Soleus   **(b)** Peroneus Longus

Figure 1.3: Two different types of muscle paths defined in gait2392 model: in (a) the *soleus* is represented as a single straight line going from the origin to the insertion; in (b) the *peroneus longus* path includes via-points to take into account the wrapping of this muscle around the lateral malleolus.

It is worth remarking that in this model there are some inaccuracies in the specification of the muscle paths. As shown in Figure 1.4, for example, the gluteus maximus path, even if in the default pose assumes an admissible shape, at the increase of hip flexion degrees some of its bundles pass through the ischial tuberosity.
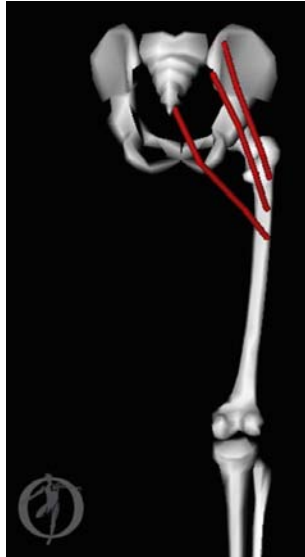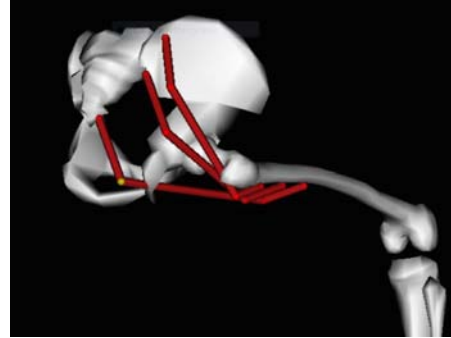
Figure 1.4: Gluteus maximus at 0° and at 60° of hip flexion where is evident that the lowest bundle of the muscle passes through the ischial tuberosity.

Muscle parameters such physiological cross-sectional area (PCSA, determining to maximum isometric force), optimal fiber length and pennation angle were first taken from literature [Friederich,1990] [Wickiewicz,1983] and adjusted with a trial-and-error approach to match muscle strength data in [Anderson,1999] [Carhart,2000]. Inertial properties (masses and moments of inertia of all segments) have been taken from an adaptation of antropometric data in [Dempster,1955].

1.3   The London Lower Limb Model (LLLM)

The London Lower Limb Model [Modenese,2011] – based on the dataset published in [Klein Horsman,2007] –, is a 12 degrees of freedom model that includes six segments: pelvis, femur, patella, tibia/fibula, hindfoot and midfoot (with phalanges). Segment reference frames are defined after [Wu,2002].

The model includes five joints that have been implemented ad in [Klein Horsman,2007], thus representing the hip as a ball-socket joint (3 degrees of freedom), while the tibio-femoral joint and the ankle joint complex (talocrural and subtalar joints) as hinges (1 degree of freedom). The patello-femoral joint, its axis and mechanism was created following [Klein Horsman,2007]. Regarding the ankle joint, as explained in section 2.2.2.1 of [Modenese,2013], given the unnatural position of the foot achieved in the default position using raw data from [Klein Horsman,2007], the hind food segment had been relocated and the subtalar joint locked in the simulations.
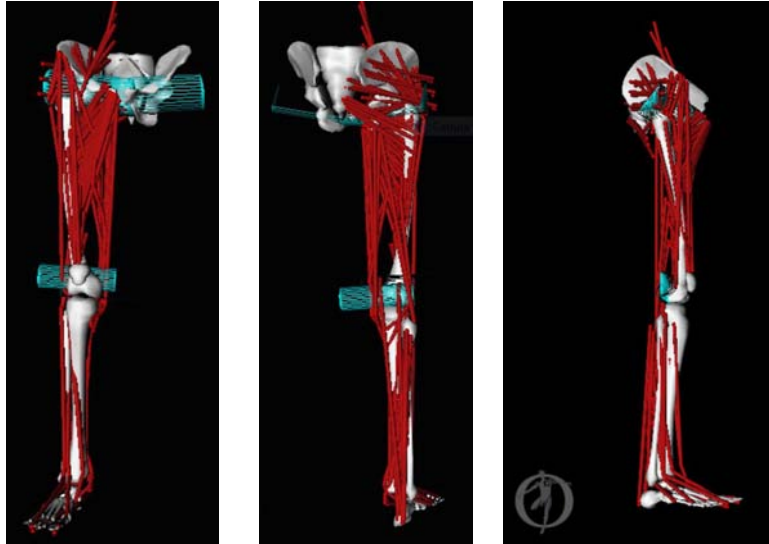
Figure 1.5: Frontal, posterior and lateral view of LLLM.

The model features 38 muscles represented by 163 actuators (one muscle part can be described by a number bundles up to six based on the size of the muscle attachments in [Van del Helm,1991]). Actuators have been described either with straight lines between origin and insertion or including via-points and wrapping surfaces. In the latter case, via-points and wrapping surfaces have been described consistently with what reported in [Klein Horsman,2007] with the addition of a cylindrical wrapping surface representing the femoral anterior surface and patellar groove. Regarding the muscle geometry, it is worth commenting on the gluteus maximus superior bundles path visible in Figure 1.6 (a). Even though the attachment points may seem incorrect, this is only due to the absence of the iliotibial band in which they insert. The other gluteal muscles paths are shown in Figures 1.6 (b), (c), (d) and (e) to be able to draw a comparison with the correspondent muscles representation in next model.

Maximum isometric force was calculated based on the measurements reported in [Klein Horsman,2007] choosing a muscle tensile stress of 37 N/cm^2. Muscle dynamics was not defined by [Modenese,2011] despite optimal fiber length was measured for all muscles by [Klein Horsman,2007]. With the aim of adopting segments inertial parameters characteristic of a young subjects population rather than of elderly subjects as in [Klein Horsman,2007], it was chosen to use regression equations provided by [Dumas,2007].
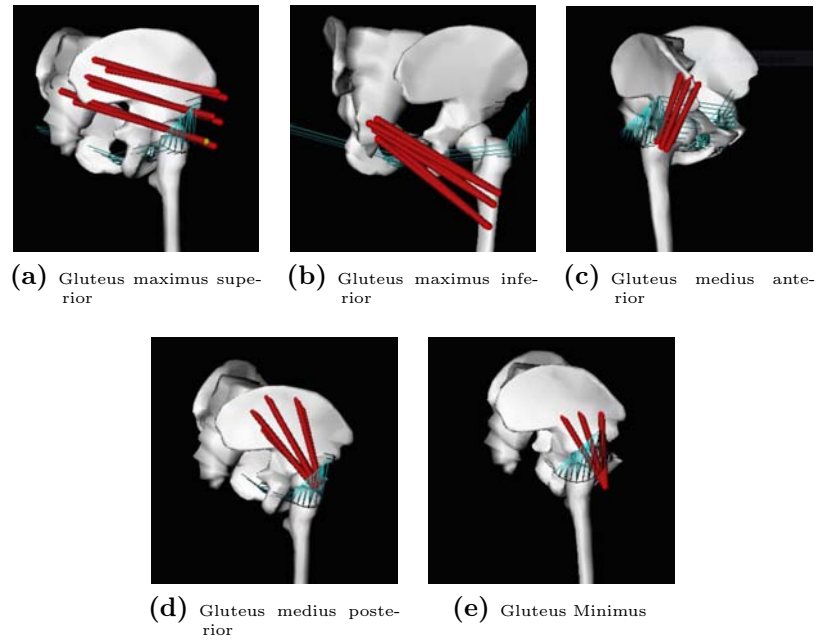
(a) Gluteus maximus superior

(b) Gluteus maximus inferior

(c) Gluteus medius anterior

(d) Gluteus medius posterior

(e) Gluteus Minimus

Figure 1.6: Gluteal muscles complex in LLLM. Please be aware that bone geometry was not provided by K-H, hence the muscle attachment do not appear on the bone surfaces.

1.4   The London Lower Limb Model 2 (LLLM2)

The London Lower Limb Model 2 (not published yet) has been developed with the aim of enhancing the anatomical accuracy of LLLM and the model estimation of the loads to be applied in finite element analysis of bone structure. This model, shown in Figure 1.7, includes the same set of segments and the joint definition used in LLLM. Having achieved a good default position even without the locking of subtalar angle, for the simulation with LLLM2 this coordinate was not locked.
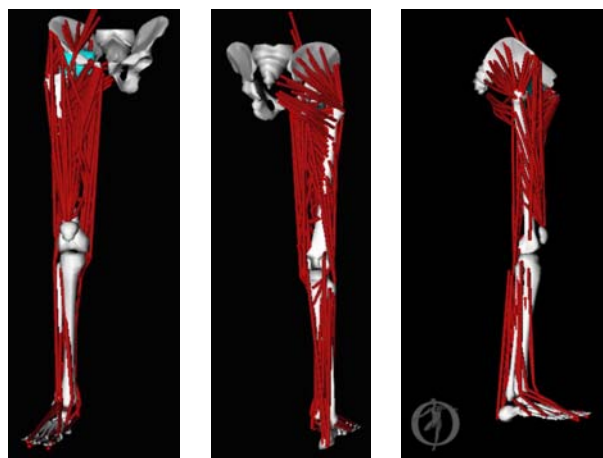

Figure 1.7: Frontal, posterior and lateral view of LLLM

To be able to give a good representation of local loads on bone, the femoral geometry of LLLM was replaced with the solid model presented in [Phillips,2012] and all muscle attachment points were moved in order to be on the surface of the bone mesh. In addition wrapping surfaces shown in Figure 1.8 were added to prevent muscle bundles to pass through the bone structure in the range of motion.
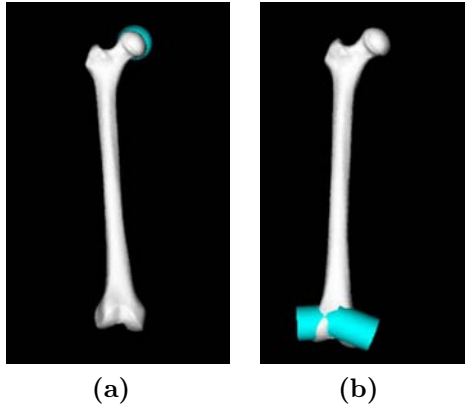

(a)   (b)

Figure 1.8: In (a) a spherical wrapping surface representing the hip joint capsule, in (b) two cilindrical wrapping surfaces at the femoral condyles

Persuaded of its important contribution to the hip joint loading, special attention was paid to the change in the design of the *gluteus maximus*. The representation of this muscle in the previous model was not suitable for finite element applications because its insertions were not connected with the femur. Therefore, based on images from the Living Human Digital Library dataset [Viceconti,2008], insertions were mapped onto the new femoral geometry and wrapping surfaces were added to give a volumetric representation of the gluteal muscles and to capture their layered disposition. As it can be seen in Figure 1.9, both the superior and the inferior set of bundles of the gluteus maximus have been divided in six actuator arranged in two layers. For each layer of the superior portion of the *gluteus maximus*, an ellipse was fitted as shown in Figure 1.10. The same approach was chosen to give better representation to the two layers of the inferior portion of the *gluteus maximus*, fitting, this time, half of an ellipse (Figure 1.11).
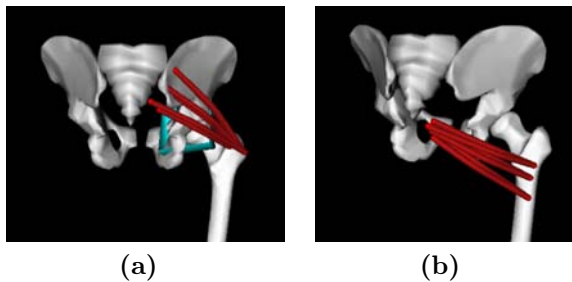

(a)   (b)

Figure 1.9: (a) Superior bundles of gluteus maximus arranged on two layers: bundles 1 to 3 at the inner layer, bundles 4 to 6 at the outer layer; (b) Inferior bundles of *gluteus maximus* arranged on two layers: bundles 1 to 3 at the inner layer, bundles 4 to 6 at the outer layer.
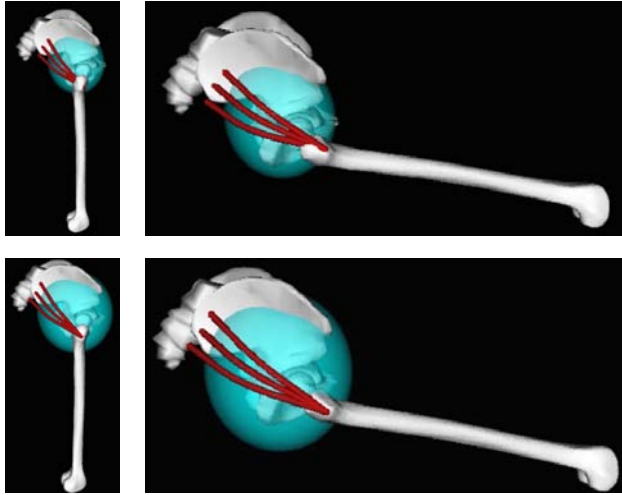
Figure 1.10: Gluteus maximus superior bundles 1 to 3 at the top and 4 to 6 at the bottom in default position of the hip joint and at 80° of flexion.
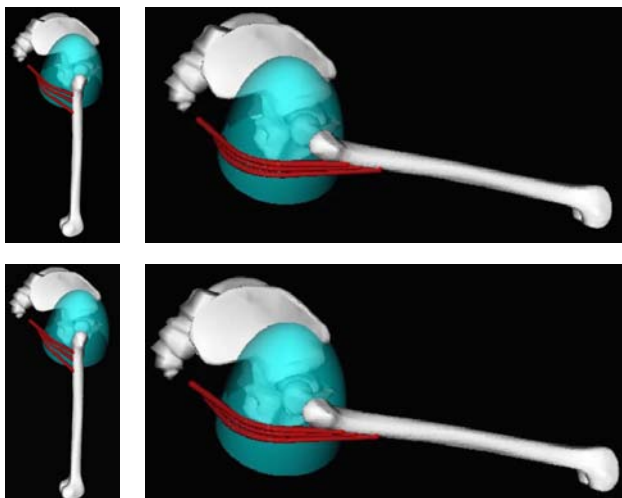

Figure 1.11: Gluteus maximus inferior bundles 1 to 3 at the top and 4 to 6 at the bottom in default position of the hip joint and at 80° of flexion.

1.5 Research Question

In the literature it is possible to find two different validation methods for musculoskeletal models. The first consists of comparing the computed hip contact forces against measurements from instrumented prosthesis [Bergmann,2001]. The second validation method qualitatively compares superficial electromyographic (EMG) signals with predicted muscle forces. However, as clearly explained in [Lund,2012], while the first method can be described as a direct validation (the model output can be compared with the experimental measurement of the same quantity), the latter is just an indirect, or qualitative validation. In this case the model output – the muscle forces or activations– and the measured EMG signals are different physical quantities. Even though efforts have been made to identify a transfer function between these two quantities [LLoyd,2003], it is still unpracticable to quantitatively compare them. To answer the research question "Which of the three musculoskeletal models better predict hip contact forces and muscle activations?"

an assessment based on two steps was chosen.

In addition to an already available dataset [Modenese,2013], including data (marker trajectories and force plates recordings) collected during 10 walking trials and 10 stair climbing trials of two healthy subjects (named SF1 and SM4), another experimental session was planned to collect data of the same set of trials from another subject, SM7, additionally equipped with EMG sensors. For subject SM7 it was possible to perform the aforementioned qualitative comparison between muscle-activations (predicted using the three models under study) and recorded EMG. For all the involved subjects, instead, a quantitative assessment was performed: mean direction and magnitude of hip contact forces were computed with the three different models and compared against the values published in [Bergmann,2001], considered as golden standard.

Chapter 2

Experimental Methods

The aim of this chapter is to describe in detail the experimental data collection and the processing leading from the collected raw data -including motion data and EMG recordings needed to answer to our research question- to the processed data to be analyzed at a later stage. The following sections will discuss the following topics: the experimental protocol (Marker set, EMG sensors placement and tasks) and the data processing.

2.1 Experimental protocol

In order to extend an already available dataset [Modenese,2013] with the data collected from a young healthy male subject additionally equipped with EMG sensors, a trial session was conducted at the Biodynamics Lab in the Hospital of Charing Cross, London. The full body kinematics of the subject (male, age: 23, mass: 90.8 Kg, height: 186 cm) for two daily living activities (i.e. walking and stair climbing) was recorded using a 10-cameras Vicon system (Oxford Metrics, Oxford, UK, sampling frequency: 100Hz). In addition to the stereophotogrammetric system, three Kistler 9286BA force platforms with sampling frequency of 1000Hz were arranged in the motion capture volume to measure the ground reaction forces and moments exerted by the subject on the ground or on the steps of an instrumented staircase depending on the tasks.

2.1.1 Marker set

A set of 57 reflective markers was placed on the subject as shown in Figure 2.1. On each body segment al least three non-collinear markers (mainly placed on body landmarks recommended in [Wu,2002]) were positioned, in order to be able to determine its position and orientation in the space (6 degrees of freedom). Given

Figure 2.1: Marker set

that in further evaluation only the kinematics of the lower limb will be taken into account, only the marker placement on the following segments will be described in detail: pelvis, thigh and shank.

As shown in Figure 2.2, four markers were placed on the pelvis and specifically on the Left Anterior Superior Iliac Spine (LASIS), on the Right Anterior Superior Iliac Spine (RASIS), Left Posterior Superior Iliac Spine (LPSIS) and Right Posterior Superior Iliac Spine (RPSIS). Knowing the position of these markers, not only it is possible to locate the pelvis in the space, but also to compute its rotation with respect to the anatomical axes.
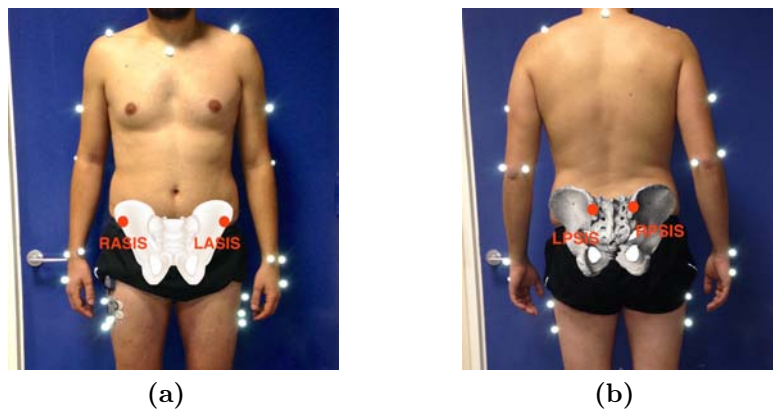

(a)   (b)

Figure 2.2: Markers on the front of the pelvis (a) and at the back (b).

To be able to locate the thigh segment in space, markers were placed on the Femoral medial (ME) and lateral (LE) epicondyles and a cluster of three markers on the lateral part of the mid thigh.
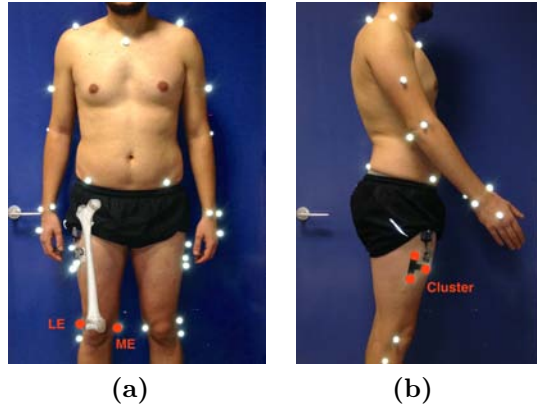
Figure 2.3: Markers on the front of the thigh (a) and on the side (b).

(a)   (b)

On the shank, markers were placed on the head of the fibula (FH), on both medial and lateral malleoli (MM and LM) and a cluster of three markers was placed on the medial part of the mid-shank.
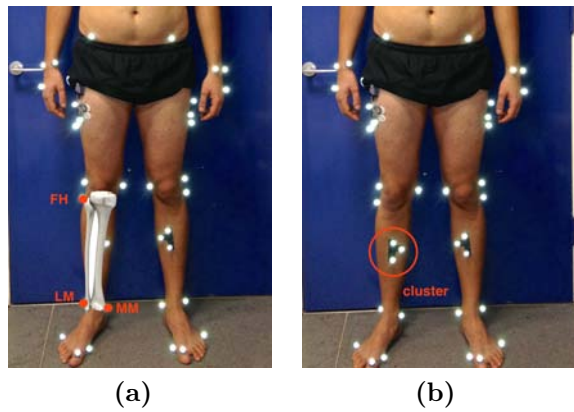

Figure 2.4: Markers on the shank: LM, MM and FH in (a), cluster of markers in (b).

(a)   (b)

Finally, markers were put on the most prominent part of the heel, on the distal extremities of the 5th and 1st metatarsi (5M and 1M) and on the big toe (BT) of the foot.
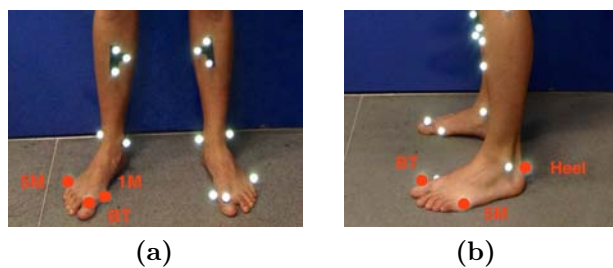

Figure 2.5: Frontal view of the markers on the foot (a) and side view (b).

(a)   (b)

2.1.2   EMG sensors

Using Myon 320 wireless system, muscular electrical activity was recorded for few superficial muscles known to be among the main actuators in walking and

stairs climbing. Following the SENIAM recommendations [Hermens,1999], after cleaning the underlying skin, electrodes were placed in positions minimizing the cross-talk between adjacent muscles and correct location was tested before starting data collection. The electrical activity was recorded for the muscles indicated in Figures 2.6 and 2.7 whose action is briefly described in the caption. Maximum voluntary contractions were collected at the end of the session in order to normalize EMG voltages and thus roughly compare them to muscle activations.

Figure 2.6: On the anterior part of the lower limb we recorded the activity of *vastus lateralis* and *medialis* (knee extensors), of *rectus femoris* which has the double role of knee extensor and hip flexor, of *tensor fascia latae* which is a hip flexor and, through the stretching of the iliotibial band, also a hip abductor and of the tibialis anterior which mainly dorsi-flexts the ankle joint.

Figure 2.7: On the posterior part of the lower limb we recorded the activity of the *semitendinosus* and *biceps femoris long head*, which are both a hip extensors and knee flexors. On the shank four main ankle plantaflexors were recorded: two *gastrocnemii*, *soleus*, and *peroneus brevis*.
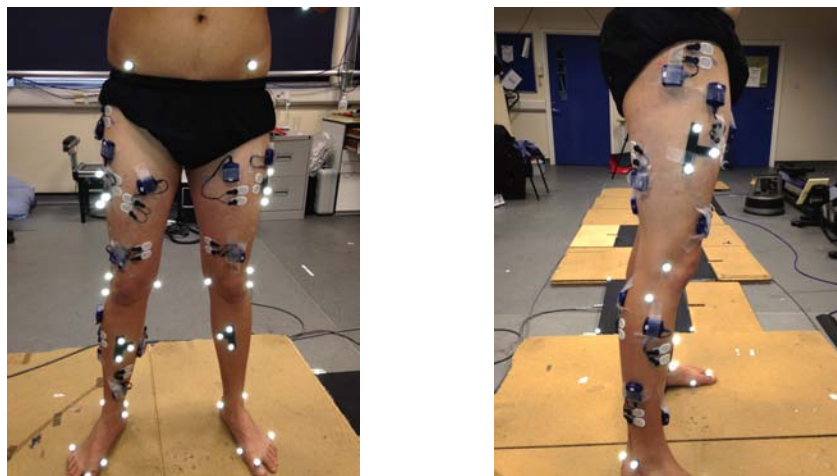

Figure 2.8: Position of EMG sensors and markers on the subject.

2.1.3 Tasks

The daily living activities that have been simulated in this thesis are: walking at a self selected speed and stair climbing. For the walking task, the three Kistler force platforms were placed in a walkway as shown in Figure 2.9 so that an entire gait cycle could be captured. For the stair climbing task, they were positioned in an instrumented staircase (shown in Figure 2.10) and the selected cycle starts with the first right heel strike (on the first step) and ends with second right heel strike on the top step of the stairs. In both situations the subject was asked to walk thorough the path few times before the recording in order to make the execution of the task as natural as possible.
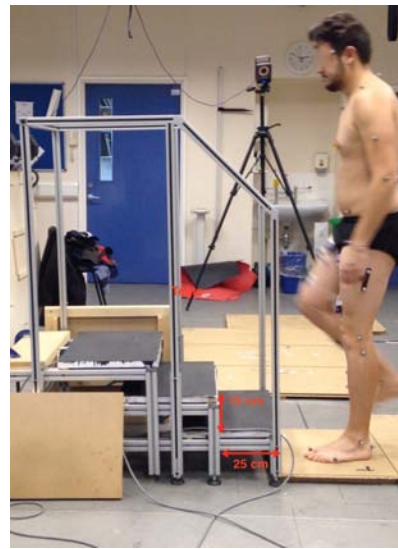

Figure 2.9: Walking Lab setup.

Figure 2.10: Stair climbing Lab setup.

2.2 Data Processing

2.2.1 Motion capture data

The c3d files generated during the recording of 10 walking trials and 10 stair climbing trials were processed with the software Vicon Nexus 1.8. Marker trajectories, first manually labelled and gap filled, were then processed using the default Butterworth low-pass filter with cut-off frequency 6 Hz [Winter,1974]. It was verified that a more theoretically correct approach such smoothing [Alonso,2004] did not give statistically different results in terms of joint moments (this check has been submitted to the XXV Congress of the International Society of Biomechanics (Glasgow 2015) as a poster presentation). The needed gait cycle events were identified using the automatic tools *'find event'* and *'autocorrelate event'* provided by

Nexus. The threshold for the measured vertical force to define a *Heel strike* event was set to 20N. The modified .c3d files were then processed in Matlab in order to transform the marker coordinates from the Vicon reference frame to the standard ISB reference frame for gait trial: X axis in the walking direction, Y in the vertical direction and Z in the medio-lateral direction [Wu,1995]. To be able to access and modify the content of the .c3d file and save the final version in the .trc format, the Biomechanical Toolkit (BTK) was used [Barre,2014].

2.2.2   Force data

Regarding the post-processing of force plate data, i.e. recorded forces and moments, Matlab code was written in order to compute the coordinates of the centre of pressure (x_{COP}, y_{COP}) and the value of the free moment M_z. Using BTK functions, it was possible to read the transduced ground reaction forces [N] and moments [Nm], move them to the upper plate of the platform and compute the COP as the point (x_{COP}, y_{COP}) on the surface of the platform such that the moments around the platform axes M_x and M_y in that point are zero:

$$x_{COP} = \frac{-M_y}{F_z} \qquad y_{COP} = \frac{M_x}{Fz} \qquad (2.1)$$

At this stage, both the free moment M_z and the coordinates of the COP (x_{COP}, y_{COP}) were expressed in the global reference frame and processed. The selected approach, to process these data is based on the singular spectrum analysis (SSA) [Golyandina,2001] and particularly on its sequential version [Alonso,2004]. Relying on this smoothing approach it was not anymore necessary to make any assumption on the original signal and, moreover, it was not required to set any arbitrary parameter, but only the choose a stopping criterion. The algorithm will hereafter briefly described for a generic force F.

Let each component of the force F be a time series S of length N. At the first iteration the time series S is transformed into a Hankel matrix H using a window of length L such that $N/L = 60$ (it has been shown in [Alonso,2004] that results are not sensitive to the window length L in the sequential version of the algorithm). With the singular value decomposition performed on H, the latter can be expressed as a sum of elementary matrices. The algorithm then truncates this sum in order to keep the 99% of the original total variance by the elimination of the elementary matrices that least contribute to the norm of the original matrix. The obtained new matrix $\hat{H}$ is therefore an approximation of the original H and the smoothed

time series $\hat{S}$ can be reconstructed by averaging the diagonals of $\hat{H}$. The second iteration of the algorithm will follow these same steps starting from the time series $\hat{S}$. The algorithm stops when the difference between the RMS of two consecutively computed $\hat{S}$ is less then 1% (to limit the oversmoothing).

2.2.3 EMG data

The digitalized EMG signals were processed with MATLAB following directions cited in [Buchanan,2004]: firstly, the raw signals underwent a full wave rectification, secondly they were filtered with a zero lag Butterworth low-pass filter with cut-off frequency of 4 Hz in order to get their linear enveloped version. At the end these new signals were divided by the peak EMG value selected from the maximum voluntary contraction task for the corresponding muscle, yielding the experimental muscle activation.
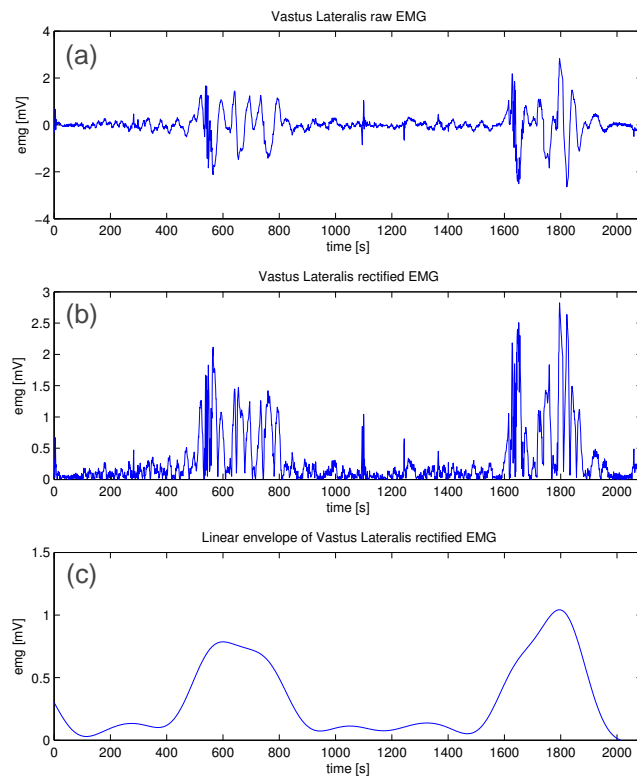

Figure 2.11: **(a)** Raw EMG signal of Vatus Lateralis, **(b)** EMG signal after full-wave rectification,**(c)**, EMG signal after final low-pass filtering.

Experimental motion capture data and force data have been used as inputs to the numerical methods described in the following chapter, while EMG signals were used at the validation stage.

Chapter 3

Numerical Methods

In this chapter the adopted numerical methods will be outlined. In the first section the open source software OpenSim will be briefly presented. Using this software, the musculoskeletal models described in the introduction were developed by the respective authors and in this study it was possible to perform all the dynamic simulations and estimate the loads in the musculoskeletal system. In the following sections it will be given a description of the five steps necessary to complete a dynamic simulation and the choices made for our specific case of study.

To run the dynamic simulation of all subjects' trials, a dedicated pipeline was written in Matlab, with the aim of limiting the operator dependent tasks and reducing the time otherwise needed to perform the simulation manually from the software graphical user interface.

3.1   Opensim software

OpenSim [Delp,2007] is an open-source modelling and simulation environment that was established to supply the biomechanics community with functionalities complementary to those coming with the already existing SIMM [Delp,1995]. Moreover, by giving full access to source code, researchers have been involved in its development. The user interface provides a broad set of tools useful to run a simulation. The included features are Scaling, Inverse Kinematics, Inverse Dynamics, Static Optimization and a set of Analyses, including the Joint-Reaction tool.

3.2   Scaling and Marker Placement

The first step to run a dynamic simulation is to scale the mass properties and the model segments dimensions so that they match the subject's segments i.e.

the distances between virtual marker belonging to the model match the distances between experimental markers for couple of markers representative of the bone lengths. In the OpenSim scaling tool, used in this thesis, it is possible to divide the scaling procedure in two different but consequent steps: the scaling of segments sizes and the markers adjustment.

Segment sizes scaling

In the first step, scaling factors need to be specified for each segment: they can be either be based on measurements or manually set. In our case, the measurement-based method was used to scale the thigh, shank and foot segments. For each of these segments the following set of marker pairs was detected:

- $(RASIS, R.FemEpic.Lat) \rightarrow thigh$

- $(R.FibHead, R.TibiaMal, Lat) \rightarrow shank$

- $(R.Heel, R.BigToe) \rightarrow foot$

Figure 3.1: $\hookleftarrow$ Set of virtual markers on the model. m_t is the distance between the virtual markers $RASIS$ and $R.FemEpic.Lat$.

Figure 3.2: $\hookrightarrow$ Set of experimental markers on the subject. e_t is the average distance between the experimental markers $RASIS$ and $R.FemEpic.Lat$.

Let, for example, be m_t the distance between the virtual markers $RASIS$ and $R.FemEpic.Lat$ in the model's default configuration. Let e_t be the average distance between the corresponding experimental markers computed across a certain number of frames of the static trial. The scaling factor for the thigh segment is therefore $s_{thigh} = \frac{e_t}{m_t}$. This way of scaling is effective for the aforementioned segments because they are mainly developed in one direction which is also the dimension necessary to capture the segment kinematics.

The pelvis, on the other hand, is a complex structure developed in three dimensions without any preferential direction. To overcome the limit given by the

impossibility of detecting scaling factors in the three dimension X, Y, Z using the four available markers, this segment was scaled manually. Dedicated Matlab functions were written to compute the scaling factors for pelvis depth (PD), width (PW) and height (PH) giving as input one time the experimental position of RASIS LASIS RPSIS and LPSIS and the other time the corresponding virtual positions. The PD was computed as the height of the triangle connecting the two ASIS and the SACRUM (virtual marker placed in the middle the two PSIS) with respect of the line connecting the two RASIS (Figure 3.3). Regarding PW, it was calculated as the distance between the RASIS and LASIS. To compute the PH the *pelvic_tilt* was first calculated as the angle between the segment previously defined to get the PD and the horizontal plane. At this stage it was possible to get the PH as $PH = PD\sin(pelvic\_tilt)$(Figure 3.4). Let PD_{mod} PW_{mod} PH_{mod} be the model pelvis characteristic dimensions and PD_{exp} PW_{exp} PH_{exp} be the experimental pelvis dimensions. The scale factors for the 3 axes of the pelvis were computed as $S_{pelvis,X} = \frac{PD_{exp}}{PD_{mod}}$, $S_{pelvis,Y} = \frac{PH_{exp}}{PH_{mod}}$, $S_{pelvis,Z} = \frac{PW_{exp}}{PW_{mod}}$.
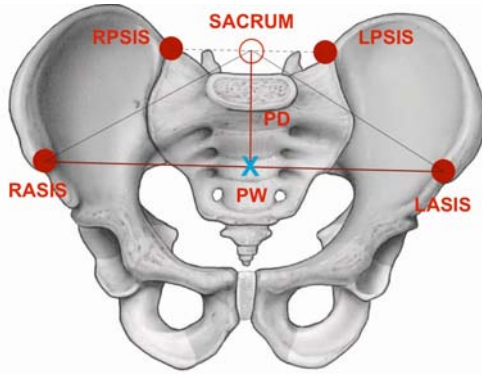

Figure 3.3: The Pelvis width (PW) is computed as the distance between the two ASIS; the Pelvis depth (PD) is equal to the height of the triangle connecting the two ASIS and the SACRUM.
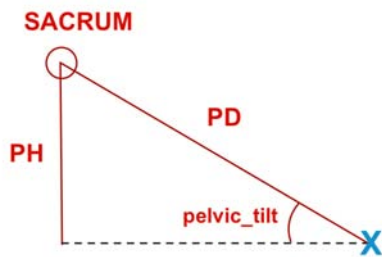

Figure 3.4: In this side view of Figure 3.3, the Pelvis height (PH) coincides with the vertical distance between the SACRUM and the point indicated with a blue cross.

Mass scaling

To scale the mass of the original model the mass of the subject's lower limb (including pelvis, right thigh, right shank, right foot) was computed. From the

subject's total mass the segments masses were derived according to parameters in [Dumas,2007] (Table 3.1) and summed. Giving the subject's lower limb mass as

Segment	weight	unit
Pelvis	14.2	%total mass
Thigh	12.3	%total mass
Shank	4.8	%total mass
Foot	1	%total mass

Table 3.1: Segments mass parameters

an input to the scaling tool and choosing not to preserve the mass distribution, the scaling algorithm automadjiacentatically scales the masses of each model's segment (body) from the body scale factor previously used to scale its size. This procedure gives as a result a lower limb total mass slightly different from the one given as input.

Markers Adjustment

At this stage the model is scaled to best match the subject lower limb, but the virtual markers inevitably do not overlap the experimental ones. It is therefore necessary to make the virtual markers move to match the experimental locations. The *Adjust Model Markers* section of the scaling tool allows specifying the static trial file based on which a step on inverse kinematics (that will be described in the following section) is accomplished: the locations of experimental markers are averaged over the selected set of frames of the static trial, and a step of inverse kinematics is solved to find the joint angles that minimize the error between the model markers and the corresponding average experimental markers. A higher weight was given to markers placed on anatomical landmarks and on the lateral side of the limb (because less affected by soft tissue movement). A Matlab code was written to calculate the default pelvic tilt for both the model and the subjects and the difference between these two was used to fix the pelvic tilt coordinate. When a satisfying pose match was reached, the model markers were moved to exactly match the experimental markers. Markers of the of the thigh and shank cluster were not used in the IK step, but just positioned based on average position once the model pose was established via global optimization.

3.3 Inverse Kinematics

The inverse kinematics in the mechanics field is commonly referred to as the inverse problem that, given the configuration of a kinematic chain, determines the joint angles achieving that configuration. The musculoskeletal model is the kinematic chain for which, given the markers trajectories, we are able to extract joint angles trajectories (coordinate trajectories) through an inverse kinematic problem.
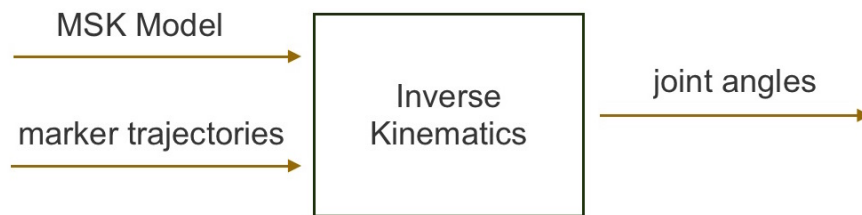

Figure 3.5: Inverse Kinematics block diagram

A generic approach to retrieve joint kinematics is available in the literature. For each body segment a cartesian coordinate system (CCS) can be placed following the recommendations of the International Society of Biomechanics [Wu,1995] [Wu,2002]. Based on the two adjiacent CCSs it is possible, for each joint, to determine a non-orthogonal joint coordinate system as first suggested in [Grood,1983], so that two of its axes are fixed to the adjacent bodies and the other one is floating. Through the decomposition of the rotation matrices, and knowing the distance between the origins of the two CCSs, the joint motion in its three rotational al three translational degrees of freedom is defined.

However, it must be noted that this method (called in [Lu,1999] Direct Method) treats each segment as a separate body and solves the inverse problem without taking into account joint constraints and rigid body hypothesis. In [Lu,1999] it is proposed an optimization method to determine, from the marker coordinates, the optimal pose of a multilink musculoskeletal model. The algorithm (Global Optimization Method, GOM) is based on global minimization (in a least squares sense) of the overall differences between experimental and virtual marker coordinates (virtual markers are markers belonging to the model). Let the general pose of the r-degree of freedom n-link chain be described by the vector of generalized

coordinates $\xi = [\xi_0, \xi_1, ..., \xi r]$. For each segment let $P^* = [P_1^*, P_2^*, ..., P_N^*]$ be the vector of the segments reference frames and $P_i^* = [p_1^*, p_2^*, ..., p_N^*]$ the marker position in the reference frame i. The GOM aims at minimizing over ξ the function

$$f(\xi) = [P - P'(\xi)]^T W[P - P'(\xi)] \tag{3.1}$$

where W is a diagonal defined positive weighting matrix and $P'(\xi) = T(\xi)P^*$ where $T(\xi)$ is the transformation matrix from the segment reference frame to the global frame, given the model pose ξ. This algorithm guarantees the rigid body hypothesis and takes advantage of the joint constraints, embedded in the model, to compute the optimal pose. Moreover, by wisely filling the matrix W it is possible to take into account each marker's degree of skin movement: markers whose position is more reliable should have higher weightings, whereas markers with higher level of artifacts should have smaller weightings.

To perform inverse kinematics in our study, the dedicated OpenSim tool was used. It implements the GOM with the additional possibility of adding in the objective function a term accounting for coordinates to track if experimental values for joint angles measurements were available. Giving as inputs the scaled model and the .trc file of maker trajectories to the IK tool it was possible to obtain the joint angles (generalized coordinates) for all the involved joints (Figure 3.5): hip, knee and ankle. To evaluate IK results, root mean squared error (RMSE) and maximum marker errors were checked to be respectively less than $2cm$ and between 2 and $4cm$.

3.4 Inverse Dynamics

Given the multi-link model, its kinematics and the external forces acting on it, it is possible to solve the inverse dynamics problem and calculate the moments acting on each joint by solving the following equation for τ:

$$M(q)\ddot{q} + C(q, \dot{q}) + G(q) + E = \tau; \tag{3.2}$$

where $q, \dot{q}$ and $\ddot{q} \in \mathbb{R}^N$ (N being the number of degrees of freedom) are the generalized coordinates position, velocity and acceleration, $M(q) \in \mathbb{R}^{N \times N}$ is the mass matrix, $C(q, \dot{q}) \in \mathbb{R}^N$ represents Coriolis and centrifugal force, $G(q) \in \mathbb{R}^N$ is the gravitational force and E is the external load given by the force plate. $\tau \in \mathbb{R}^N$, the unknown of the problem, is the vector of generalized forces acting on the coordinates.
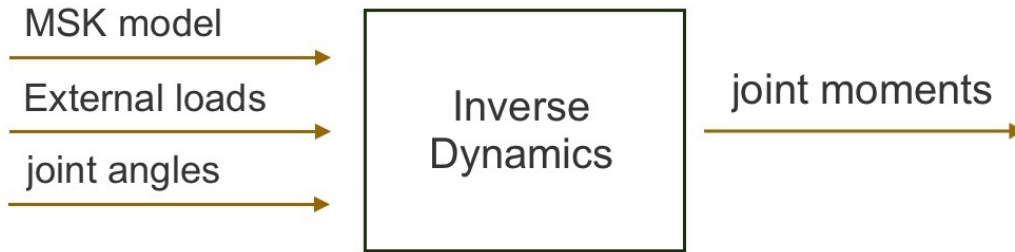
Figure 3.6: Inverse Dynamics block diagram

In this study the inverse dynamics problem was solved using the OpenSim dedicated tool, giving as inputs the scaled model, the external loads file and the filtered kinematics resulting from previous IK step (Figure 3.6). Ground reaction forces, processed as described in 2.2.2, were applied to the calcaneal segment.

3.5 Static Optimization

The static optimization is a further step in the inverse dynamics evaluation. In particular, at this stage we would like to estimate the muscle activation pattern that generated the net moment τ in equation (3.2). In formulas, the static optimization aims to solve for a vector $F \in \mathbb{R}^M$ (F being the vector of muscle force magnitudes and M the number of muscles) the following system of equations :

$$\begin{cases} r(q)F = \tau \\ 0 \le F_i^{(M)} \le F_{ISO,i}^{(M)}, i \in \{1, ..., n^M\} \end{cases}$$

where $r(q)$ is the set of muscle moment arms: the scalar value representing the perpendicular distance between the joint centre and the muscle line of action. However, it is evident that the solution to previous system is indeterminate: the dimension of F is greater than the number of equations and, hence, than the degrees of freedom of the model ($M > N$). The physiological reason for this indeterminacy is the fact that the human muscular system is extremely redundant (the number of muscles exceeds the minimum number necessary to perform a motion task). Nevertheless, the central nervous system (CNS) is able to solve this indeterminacy through a criterion that has been hypothesized to find muscle forces F_m as the solution to the generic optimization problem:

$$\min_{F_m} \Phi(F_m) \qquad \text{subject to} \qquad \begin{cases} r(q)F = \tau \\ 0 \leq F_i^{(M)} \leq F_{ISO,i}^{(M)}, i \in \{1, ..., n^M\} \end{cases} \qquad (3.3)$$

To be able to find a unique solution, as reported in [Rasmussen,2001], several methods have been proposed in literature that try to mimic CNS choice criterion by using minimization/maximization of different quantities: the maximization of muscle endurance through minimization of muscle stress cubed has been proposed in [Crowninshield,1981]; **Polynomial criteria** aims at minimizing a weighted average of muscle forces; **Soft saturation criteria** minimize, instead, the average distance from the maximum load. Finally, the **min-max criterion** maximizes the distribution of the forces among all the muscles, thus minimizing the maximum relative muscle force.

Figure 3.7: Static optimization block diagram

To perform this calculation, the OpenSim Static Optimization tool was used. This algorithm implements the minimization of the following objective function:

$$\Phi(F_m) = \sum_{m=1}^{n} \left(\frac{F_m}{F_{m,ISO}} \right)^P = \sum_{m=1}^{n} (a_m)^P \qquad (3.4)$$

where n is the number of muscle in the model, a_m is the activation level of muscle m (being F_m and $F_{m,ISO}$ respectively the muscular force and its maximum isometric force) and P is a scalar that can be defined by the user. Considering the evaluations in [Modenese,2011], the latter was set to $P = 2$.

3.6   Joint Contact Forces

The muscular forces - output of the static optimization step - produce compressive and shear forces across the joint contact surfaces. To compute the joint

reactions in this study, the OpenSim Joint Reaction Analysis tool was used. It computes joint forces and moments transferred between adjiacent body segments as a result of all loads acting on the model. To perform the analysis, in addition to the same inputs of the static optimization tool, a muscle force file need to be inputted. The resulting reaction loads act at the joint centres and correspond to the internal loads carried by the joint structure i.e. by all unmodelled structures such as ligaments, cartilage and anatomical constraints.

Chapter 4

Walking task: results and discussion

In this chapter the results obtained following the methods described in Chapter 3 will be presented for each subject performing the walking trials. For each subject the coordinate trajectories, the moments at the joints and, finally, the hip joint contact forces will be shown. For subject SM7, also the qualitative comparison between muscle activation and EMG signals will be presented. Finally, in the Discussion section an overall analysis of the results will be outlined.

4.1   Subject SF1

The subject SF1 (female, weight: $54.1Kg$, height: $165.5cm$) performed the walking trials with an average speed of $1.39m/s$, close to the speed of $1.46m/s$ classified in [Bergmann,2001] as fast walking.

Inverse Kinematics results

The coordinate trajectories for ankle, knee and hip joints computed with the three musculoskeletal models are shown in Figures 4.1, 4.2 and 4.3. It can be observed that for all the models there is a good similarity in the trends of the resulting joint angle, while the ranges do not match. An interpretation on these results will be given in the Discussion section.
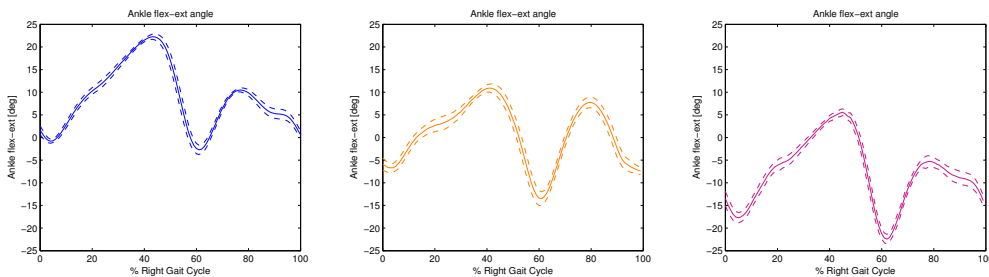
Figure 4.1: Average ankle joint dorsi-plantar flexion angle trajectory (solid line) through the gait cycle with relative standard deviations (dashed line) obtained using gait2392, LLLM, LLLM2.
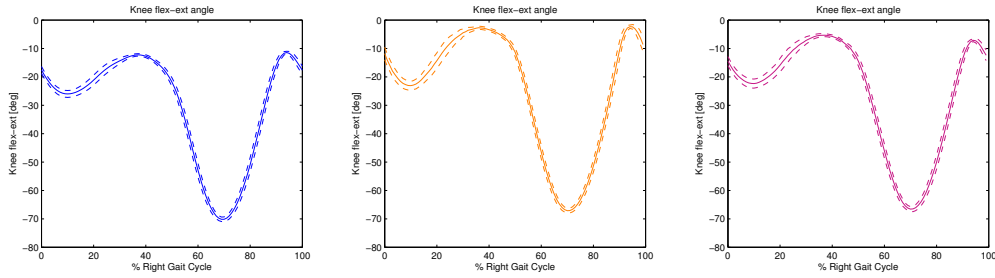
Figure 4.2: Average knee joint flexion-extension angle trajectory (solid line) through the gait cycle with relative standard deviations (dashed line) obtained using gait2392, LLLM, LLLM2.
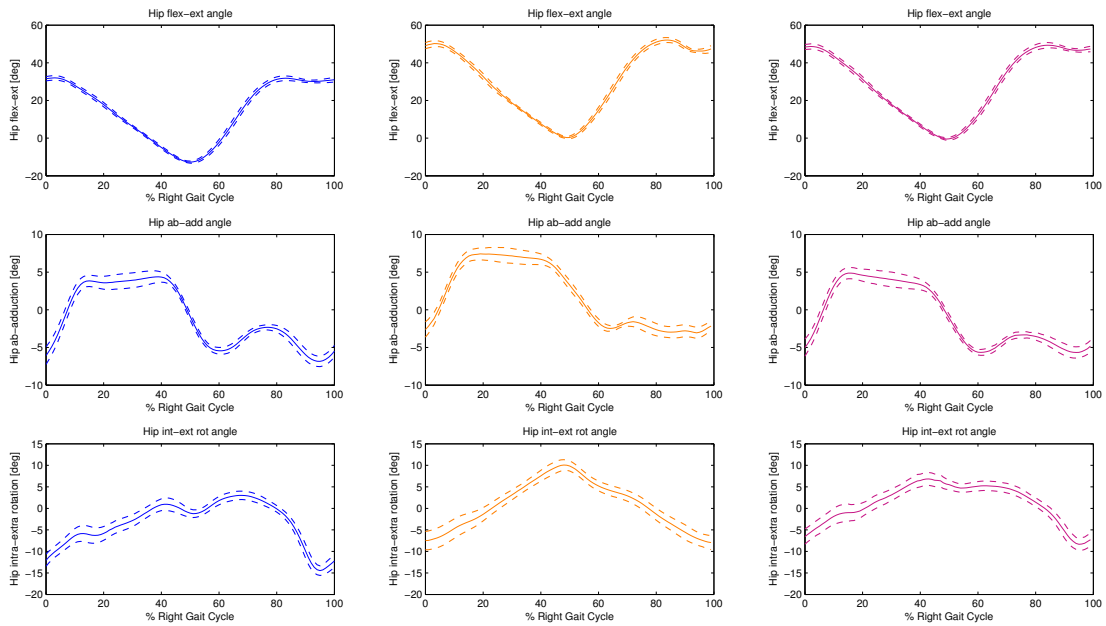

Figure 4.3: Average hip joint flexion-extension, ab-adduction and intra-extra rotation angles trajectories (solid line) through the gait cycle with relative standard deviations (dashed line) obtained using the three models under study: gait2392, LLLM, LLLM2.

Inverse Dynamics results

The moments acting at the ankle, knee and hip joint are shown in Figures 4.4, 4.5 and 4.6. Observing the results – and in particular the ranges reported in Table 4.1–, it can be stated that the resulting moments are almost independent from the model used to perfrom the evaluation. Small differences can be spotted at the lowest peaks of the ankle dorsi-plantar flexion and knee flexion-extension moments and at the hip intra-extra rotation moment whose magnitude is however negligible with respect to the other degrees of freedom.
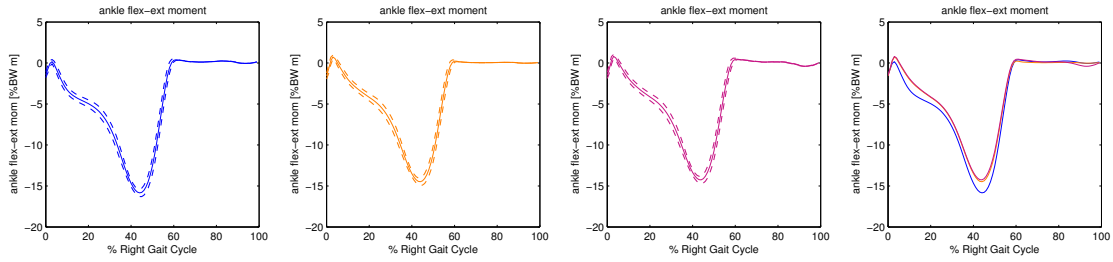
Figure 4.4: Average ankle joint dorsi-plantar flexion moments (solid line) with relative standard deviations (dashed line) obtained using the three models under study: gait2392, LLLM, LLLM2.
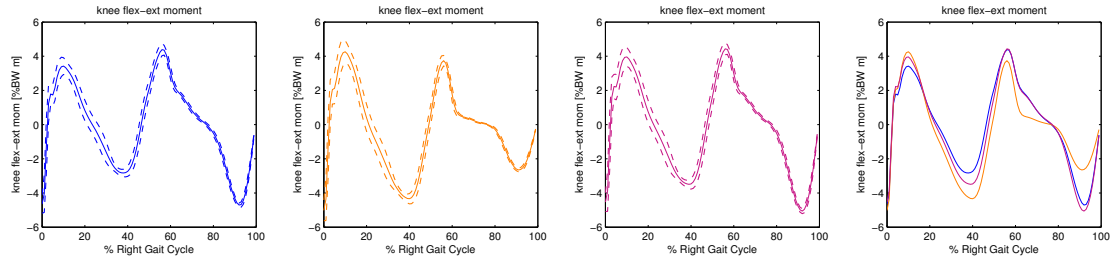
Figure 4.5: Average knee joint dorsi-plantar flexion moments (solid line) with relative standard deviations (dashed line) obtained using the three models under study: gait2392, LLLM, LLLM2.In last column the mean values obtained with the three models have been overlapped to ease the visual comparison.
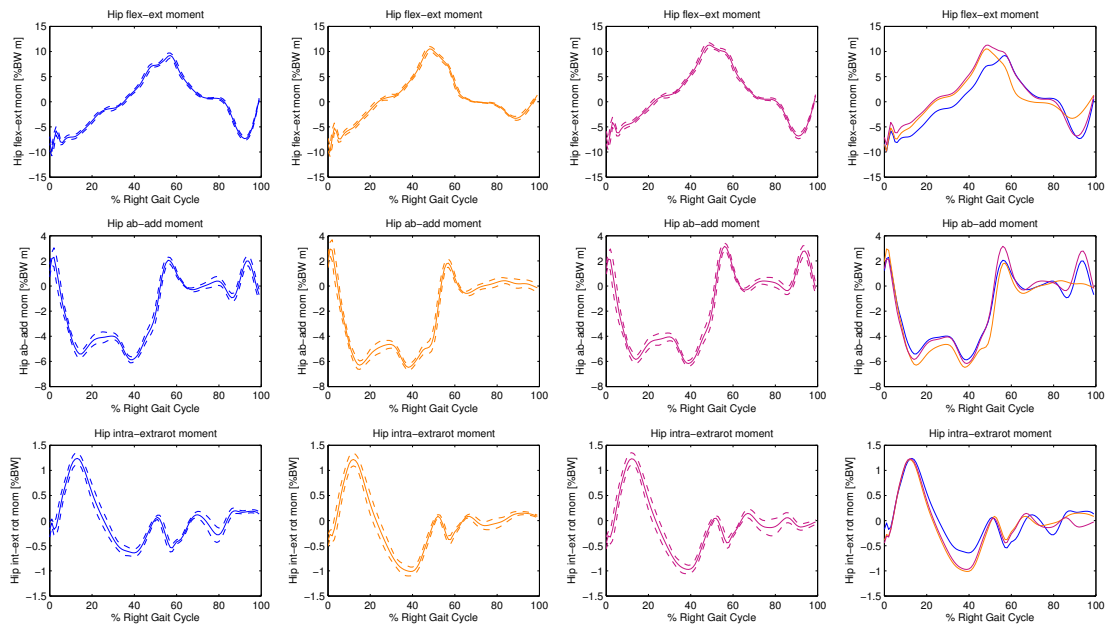
Figure 4.6: On the rows the average hip joint flexion-extension, ab-adduction and intra-extra rotation moments (solid line) with relative standard deviations (dashed line) obtained using the three models under study: gait2392, LLLM, LLLM2.In last column the mean values obtained with the three models have been overlapped to ease the visual comparison.

Table 4.1: Ranges [min max] reached by the moments acting on the hip, knee and ankle when computed with the three different models

	gait2392	LLLM	LLLM2
hip flexion-extension moment [%Bw m]	[-9.88 9.21]	[-9.83 10.51]	[-8.58 11.28]
hip ab-adduction moment [%Bw m]	[-5.87 2.29]	[-6.47 2.95]	[-6.16 3.16]
hip intra-extra rotation moment [%Bw m]	[-0.64 1.24]	[-1.01 1.22]	[-0.97 1.23]
knee flexion-extension moment [%Bw m]	[-4.71 4.39]	[-5.02 4.26]	[-5.06 4.43]
ankle dorsi-plantar flexion moment [%Bw m]	[-15.84 0.39]	[-14.48 0.72]	[-14.25 0,8]

Joint Reaction Analysis results

The resultant of hip contact forces (HCFs) computed using the three models is shown in Figure 4.7. To further analyze the HCFs , Matlab code was written to detect automatically for each trial the occurrence time of the two main peaks. At these two time instants the mean orientation and magnitude of the resultant components in the sagittal, frontal and transversal planes were extracted (Figures 4.9 and 4.10). Finally, in the boxplots of Figure 4.8 is examined the distribution of the magnitudes of predicted HCF (with the three models) at the two peaks over the entire set of walking trials. It can be observed that while at the first peak the gait2392 prediction of HCFs exceeds the prediction of LLLM and LLLM2 respecitvely by 15 and 30%BW, at the second peak gait2392 predicts the lowest HCF among the models. At the second peak the highest value, 480%BW, is reached by LLLM2 model that predicts a HCF 110%BW and 160%BW higher than the values predicted by LLLM and gait2392.
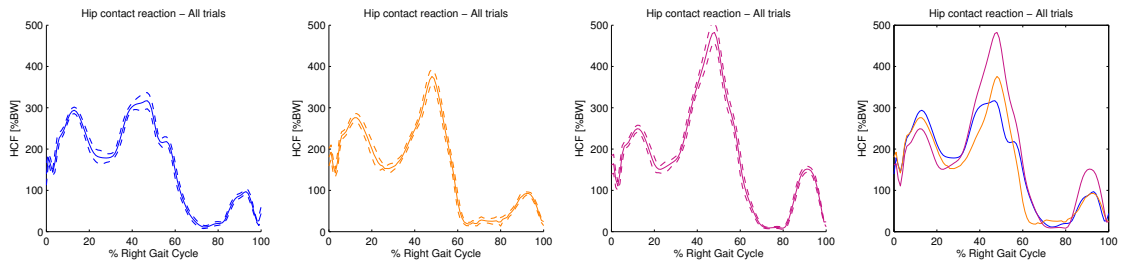
Figure 4.7: Average hip contact forces resultant (solid line) through the gait cycle with relative standard deviations (dashed line). On each column the resultant obtained using one of the three models under ivestigation is shown: gait2392, LLLM, LLLM2. In the last column the mean values obtained with the three models have been overlapped to ease the visual comparison.

Regarding the orientation of HCF at the first peak (Figure 4.9), the component on the sagittal plane of HCF predicted using gait2392 is the most posteriorly oriented (negative direction of X components) while the other two prediction are overlapped; on the frontal and transversal planes the most laterally oriented (positive direction of
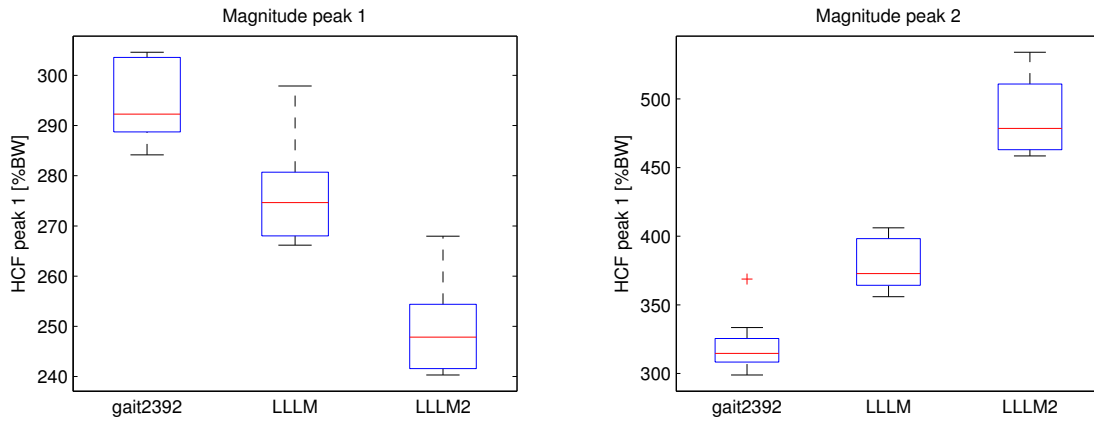
Figure 4.8: Boxplots showing the distribution of the magnitudes of predicted HCF (with gait2392, LLLM and LLLM2 models) at the two main peak instants. The central mark is the median value, the edges of the box are the 25th and 75th percentiles, the whiskers extend to the most extreme data points not considered outliers, and outliers are plotted individually with red +.

Z component)is the LLLM prediction followed in turn by the gait2392 and LLLM2. At the second peak the HCF predicted by LLLM is both the most anteriorly and laterally oriented.
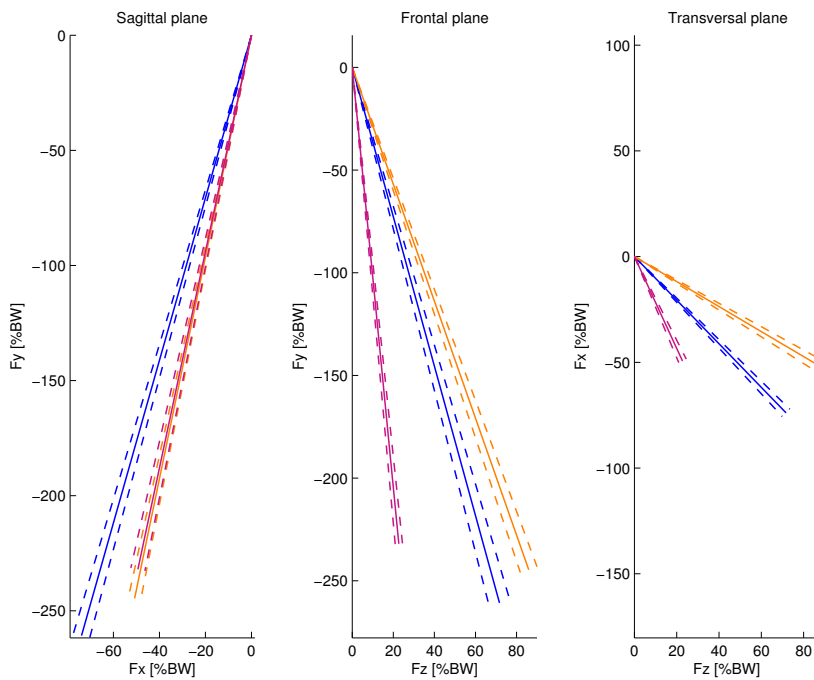
Figure 4.9: Average orientation (± standard deviation in dashed line) and magnitude of the components of HCF in the sagittal, frontal and transversal plane **at the first peak**. Computed using gait2392, LLLM, LLLM2. Positive orientations of X,Y and Z components correspond respectively to posterior-anterior, distal-proximal and medio-lateral direction.
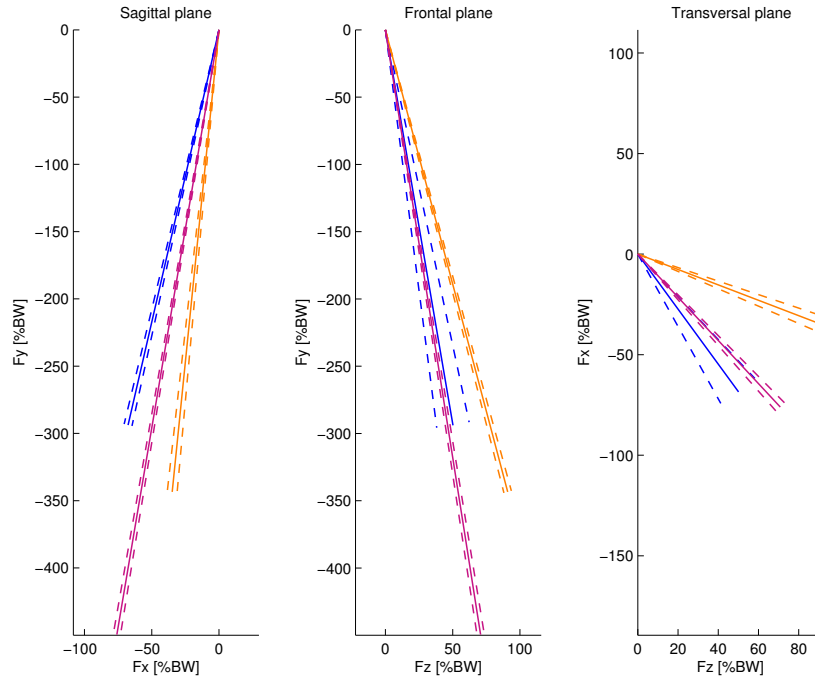
Figure 4.10: Average orientation (± standard deviation in dashed line) and magnitude of the components of HCF in the sagittal, frontal and transversal plane **at the second peak**. Computed using gait2392, LLLM, LLLM2. Positive orientations of X,Y and Z components correspond respectively to posterior-anterior, distal-proximal and medio-lateral direction.

4.2   Subject SM4

The subject SM4 (male, weight: $84.5Kg$, height: $192cm$) has performed the walking trials with an **average speed** of $1.06m/s$, close to the speed $1.09m/s$ classified in [Bergmann,2001] as normal walking.

Inverse Kinematics results

The coordinate trajectories for ankle, knee and hip joints computed with the three musculoskeletal models are shown in Figures 4.11, 4.12 and 4.13. With respect to the same results but relative to subject SF1, it must be noted the higher standard deviation at the lowest peak ok ankle dorsi-plantar angle trajectory, probably due to a less natural walking of SM4 subject through the trials (less repeatability). It can be observed that for all models there is a good similarity in the trends of the resulting joint angle, while the ranges do not match perfectly. An interpretation on these results will be given in the Discussion section.
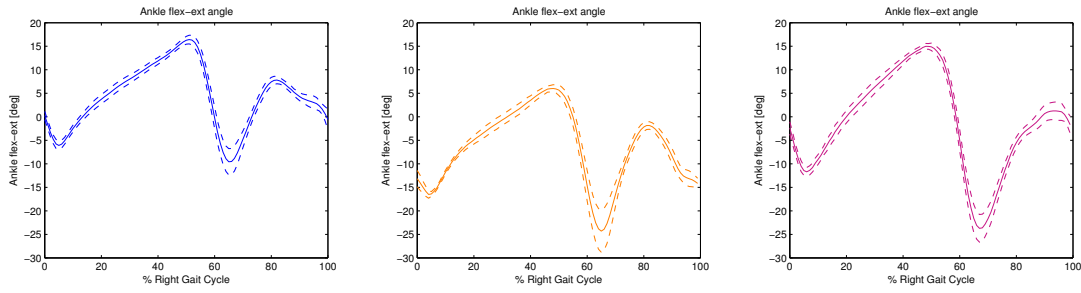
Figure 4.11: Average ankle joint dorsi-plantar flexion angle trajectory (solid line) through the gait cycle with relative standard deviations (dashed line) obtained using the three models under study: gait2392, LLLM, LLLM2.
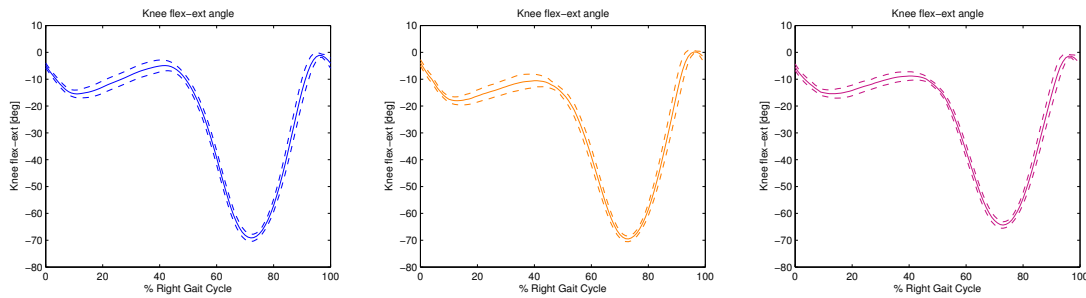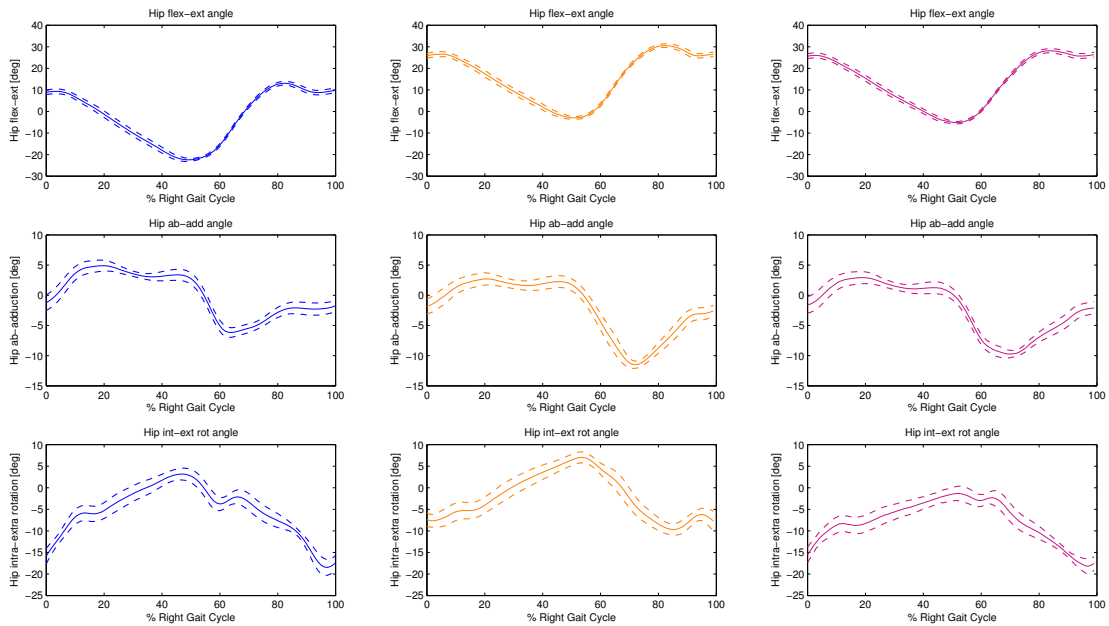

Figure 4.12: Average knee joint flexion-extension angle trajectory (solid line) through the gait cycle with relative standard deviations (dashed line) obtained using the three models under study: gait2392, LLLM, LLLM2.

Figure 4.13: On the rows the average hip joint flexion-extension, ab-adduction and intra-extra rotation angles trajectories (solid line) through the gait cycle with relative standard deviations (dashed line) obtained using gait2392, LLLM, LLLM2.

Inverse Dynamics results

The moments acting at the ankle, knee and hip joint are shown in Figures 4.14, 4.15 and 4.16. Observing the results – and in particular the ranges reported in Table 4.2–, it can be stated that, also for this subject, the resulting moments are almost independent from the model used to perfom the evaluation. The most evident differences are the higher value reached by LLLM2 at the hip flexion-extension moment and especially the discrepancy between gait2392 knee flexion-extension moment and the same moment computed with the other two models.
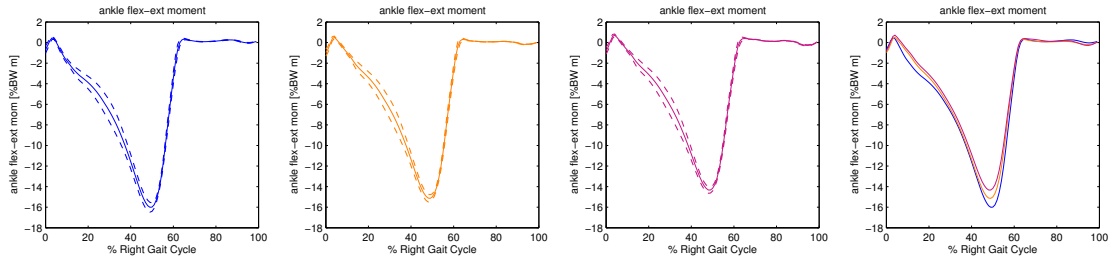
Figure 4.14: Average ankle joint dorsi-plantar flexion moment through the gait cycle with relative standard deviations. On each column is shown the result obtained using the three models under study: gait2392, LLLM, LLLM2.
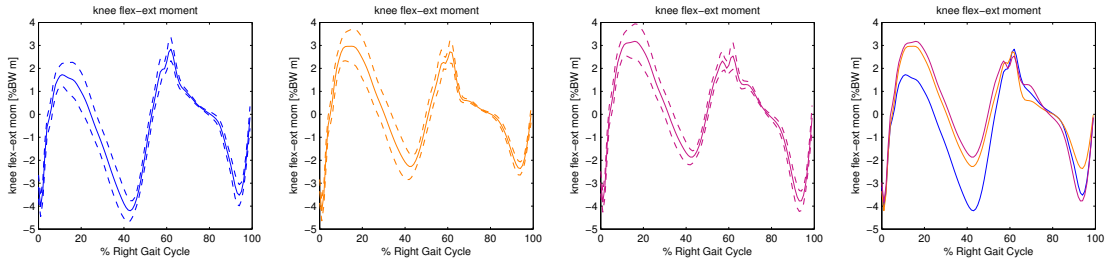

Figure 4.15: Average knee joint flexion-extension moment through the gait cycle with relative standard deviations. On each column is shown the result obtained using gait2392, LLLM, LLLM2.

Table 4.2: Ranges [min max] reached by the moments acting on the hip, knee and ankle when computed with the three different models

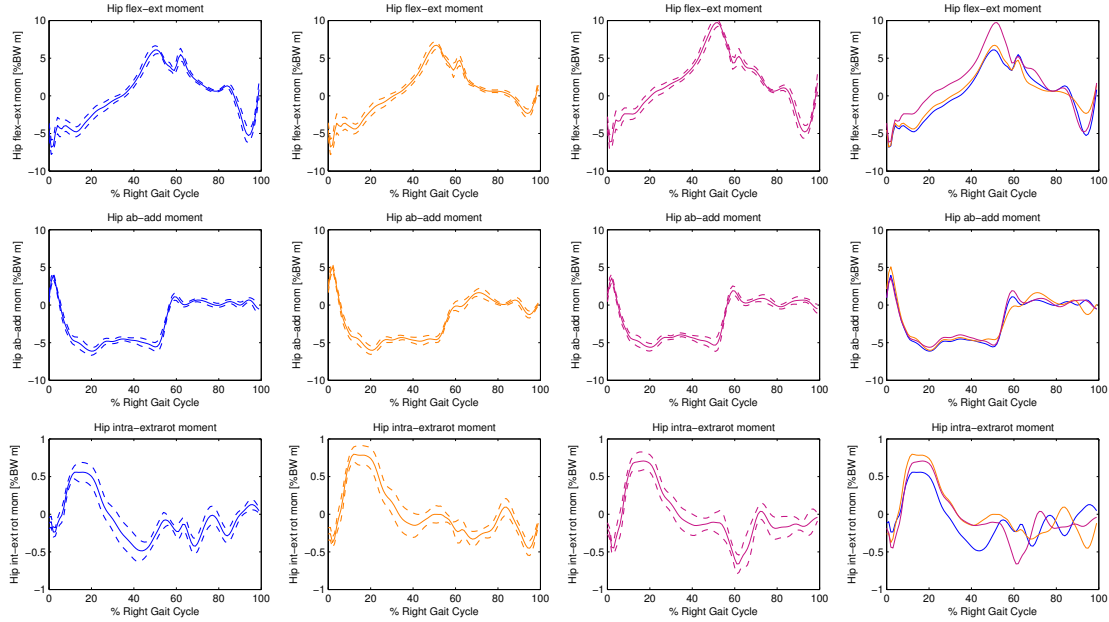|	gait2392	LLLM	LLLM2
hip flexion-extension moment [%Bw m]	[-6.83 6.09]	[-6.80 6.71]	[-6.14 9.73]
hip ab-adduction moment [%Bw m]	[-6.13 3.94]	[-6.01 5.08]	[-5.61 3.60]
hip intra-extra rotation moment [%Bw m]	[-0.49 0.56]	[-0.45 0.8]	[-0.66 0.71]
knee flexion-extension moment [%Bw m]	[-4.2 2.84]	[-4.2 2.96]	[-3.82 3.18]
ankle dorsi-plantar flexion moment [%Bw m]	[-16.01 0.45]	[-15.14 0.51]	[-14.33 0.72]

Figure 4.16: On the rows the average hip joint flexion-extension, ab-adduction and intra-extra rotation moments (solid line) with relative standard deviations (dashed line) obtained using the three models under study: gait2392, LLLM, LLLM2.

Joint Reaction Analysis results

The resulting hip contact forces (HCFs) computed using the three models is shown in Figure 4.17. As for subject SF1, mean orientation and magnitude of the resultant components in the sagittal, frontal and transversal planes were extracted at the two peak instants (Figures 4.19 and 4.20). Finally, in the boxplots of Figure 4.18 the distribution of the magnitudes of predicted HCF (with the three models) at the two peaks over the entire set of walking trials is examined. It can be observed that while at the first peak the median predictions of HCF are in a range of $30\%BW$, at the second peak LLLM2 prediction exceeds gait2392 and LLLM prediction respectively of $130\%BW$ and $230\%BW$.

Regarding the orientation of HCF at the first peak shown in Figure 4.19, it can be observed that on the sagittal and on the transversal planes the orientation of the predictions do not differ. Among the frontal plane components prediction, the LLLM2 is the most medially oriented. At the second peak (Figure **??**) the HCF predicted by LLLM is both the most anteriorly and laterally oriented, while gait2392 prediction results as the most posteriorly and medially oriented.
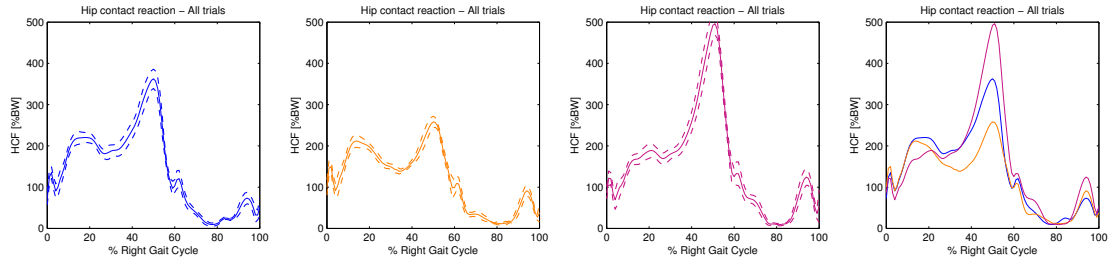
Figure 4.17: Average hip contact forces resultant through the gait cycle with relative standard deviations. On each column is shown the resultant obtained using one of the three models under study: gait2392, LLLM, LLLM2. In last column the mean values obtained with the three models have been overlapped to ease the visual comparison.
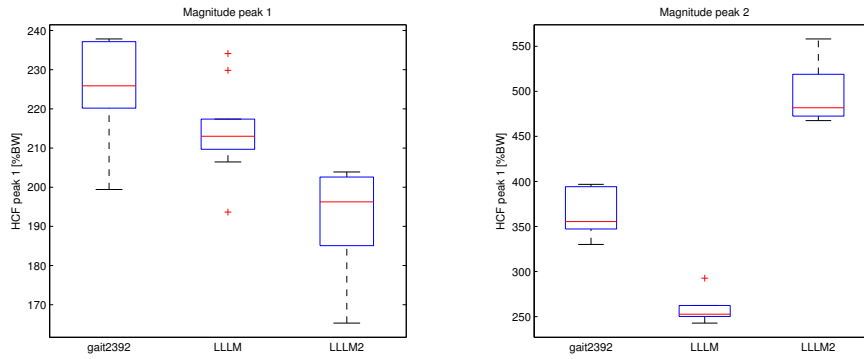

Figure 4.18: Boxplots showing the distribution of the magnitudes of predicted HCF (with gait2392, LLLM and LLLM2 models) at the two main peak instants.
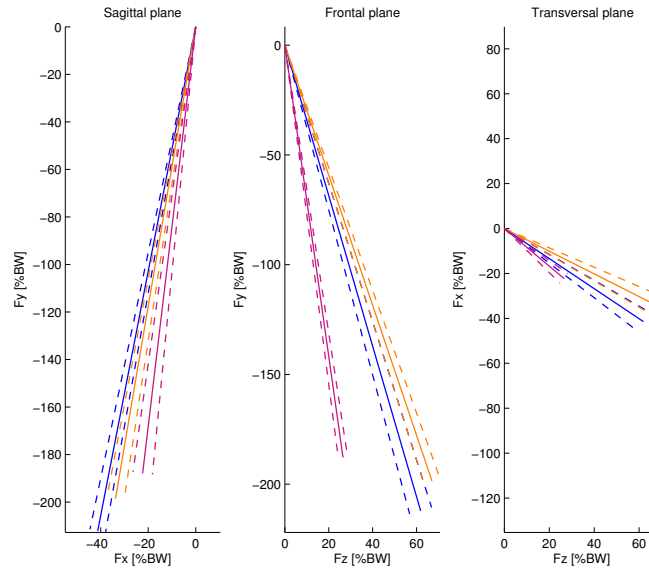

Figure 4.19: Average orientation ($\pm$ standard deviation in dashed line) and magnitude of the components of HCF in the sagittal, frontal and transversal plane **at the first peak**. Computed using gait2392, LLLM, LLLM2. Positive orientations of X,Y and Z components correspond respectively to posterior-anterior, distal-proximal and medio-lateral direction.
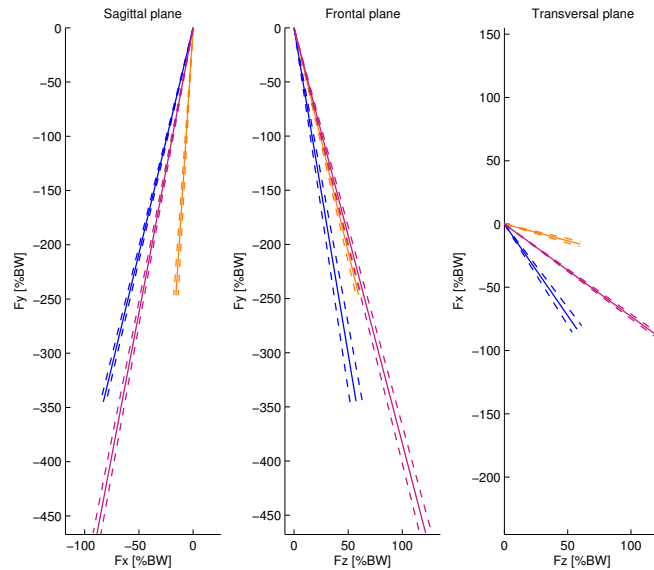
Figure 4.20: Average orientation (± standard deviation in dashed line) and magnitude of the components of HCF in the sagittal, frontal and transversal plane **at the second peak**. Computed using gait2392, LLLM, LLLM2. Positive orientations of X,Y and Z components correspond respectively to posterior-anterior, distal-proximal and medio-lateral direction.

4.3 Subject SM7

The subject SM7 (male, weight: $90.8Kg$, height: $186cm$), whose experimental session has been described in Chapter 2, has performed the walking trials with an **average speed** of $1.30m/s$, close to the speed $1.46m/s$ classified in [Bergmann,2001] as fast walking. It is worth stressing that the subject's walking during the experimental session was particularly compelled by the disposition of the platforms in the laboratory, thus causing a not completely consistent way of walking among the ten trials.

Inverse Kinematics results

The coordinate trajectories for ankle, knee and hip joints computed with the three musculoskeletal models are shown in Figures 4.21, 4.22 and 4.23. It can be observed also for this subject that for all the models there is overall a good similarity in the trends of the resulting joint angles, while the ranges do not match. An interpretation on these results will be given in the Discussion section.
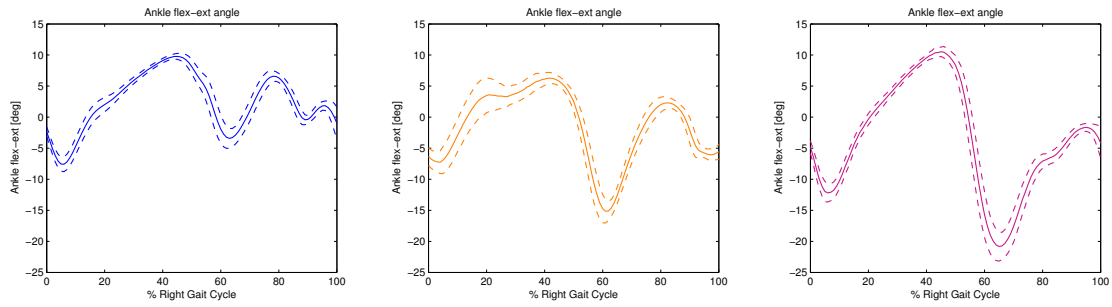
Figure 4.21: Average ankle joint dorsi-plantar flexion angle trajectory (solid line) through the gait cycle with relative standard deviations (dashed line) obtained using the three models under study: gait2392, LLLM, LLLM2.
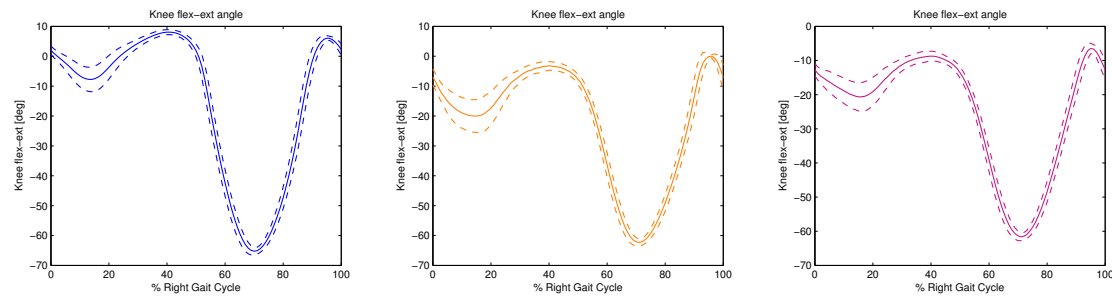

Figure 4.22: Average knee joint flexion-extension angle trajectory (solid line) through the gait cycle with relative standard deviations (dashed line) obtained using the three models under study: gait2392, LLLM, LLLM2.
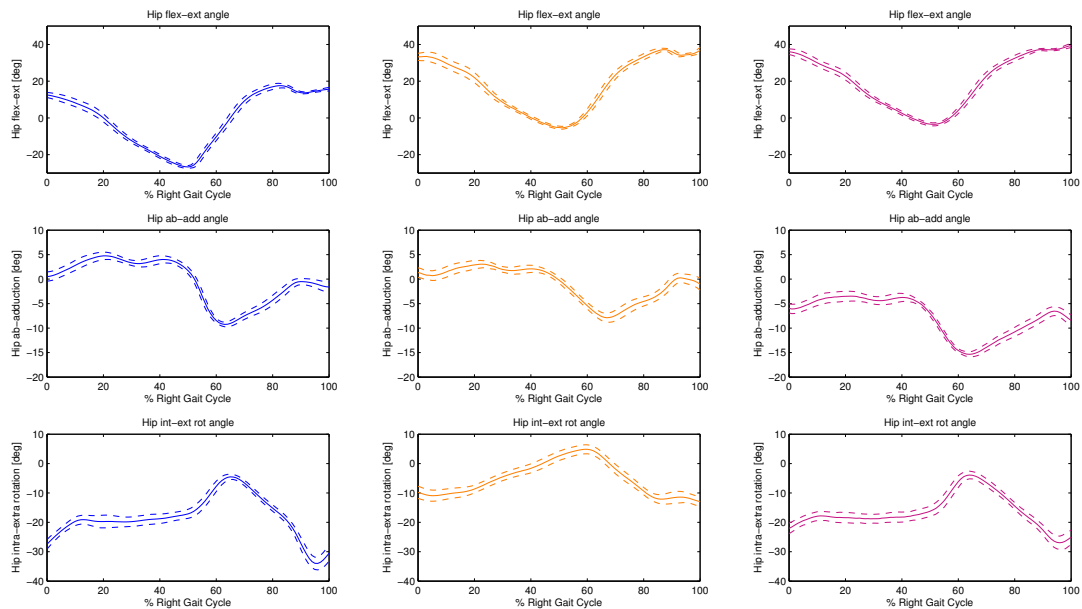

Figure 4.23: On the rows the average hip joint flexion-extension, ab-adduction and intra-extra rotation angles trajectories (solid line) through the gait cycle with relative standard deviations (dashed line) obtained using gait2392, LLLM, LLLM2.

Inverse Dynamics results

The moments acting at the ankle, knee and hip joint are shown in Figures 4.24, 4.25 and 4.26. It can be observed, with respect to the ankle joint moment results shown for the other subjects (Figure 4.4 and Figure 4.14), that for subject SM7 there is a wide distribution of the results yielding standard deviation up to $3.71\%BWm$, $3.46\%BWm$ $3.29\%BWm$ respectively for gait2392, LLLM and LLLM2. It is worth noticing the difference in the amplitude of the knee flexion moment at the 20% of the gait cycle: $0.7073\%BWm$ for gait2392 against the $6.77\%BWm$ of LLLM2 and the $7.52\%BWm$ of LLLM.
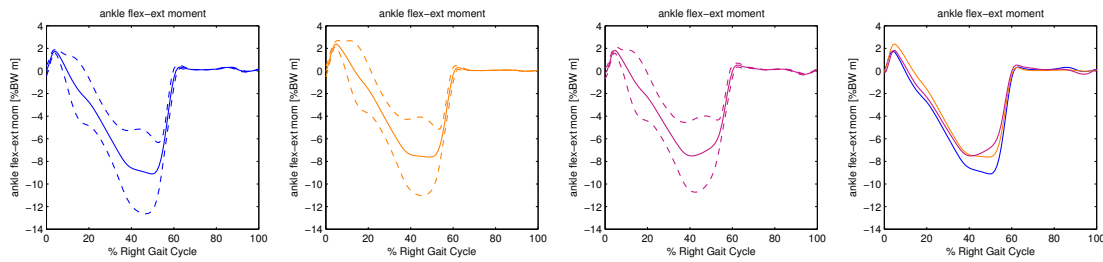

Figure 4.24: Average ankle joint dorsi-plantar flexion moment through the gait cycle with relative standard deviations. On each column is shown the result obtained using the three models under study: gait2392, LLLM, LLLM2.
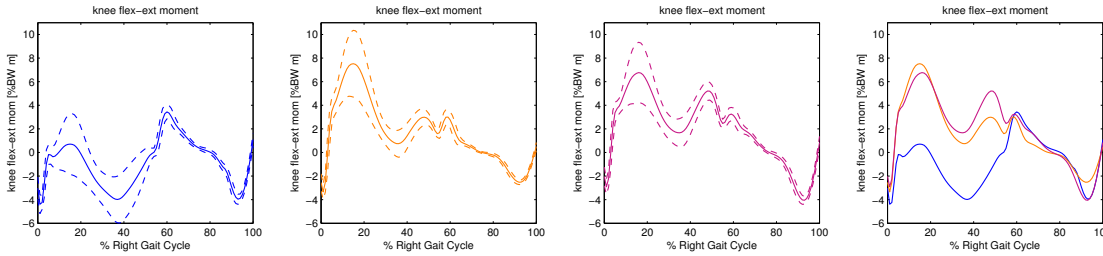

Figure 4.25: Average knee joint flexion-extension moment through the gait cycle with relative standard deviations. On each column is shown the result obtained using gait2392, LLLM, LLLM2.

Table 4.3: Ranges [min max] reached by the moments acting on the hip, knee and ankle when computed with the three different models

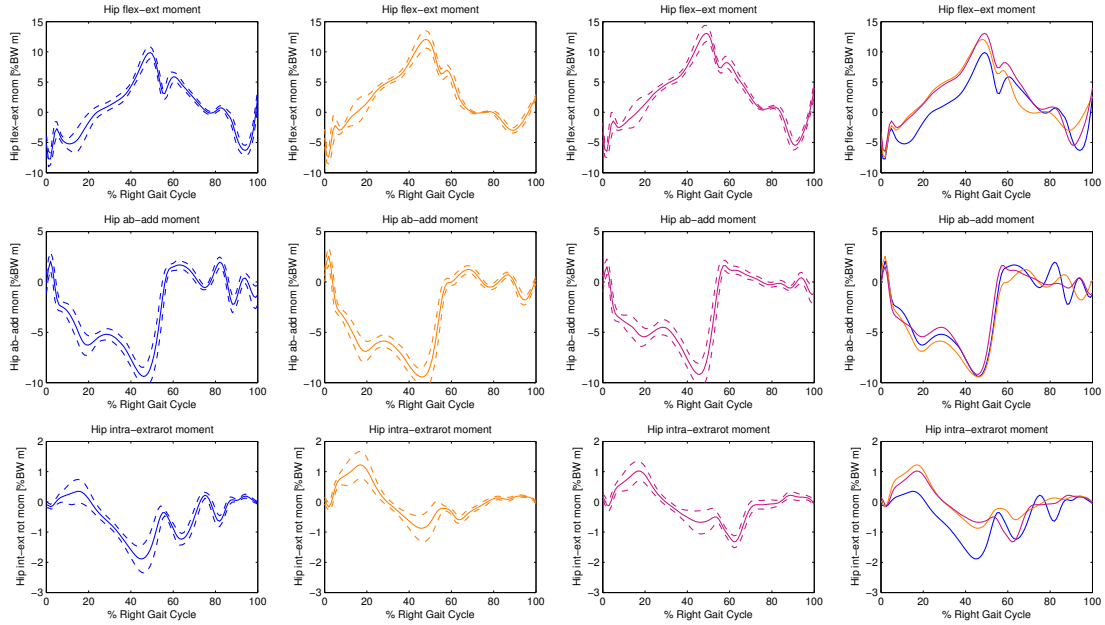|	gait2392	LLLM	LLLM2
hip flexion-extension moment [%Bw m]	[-7.73 9.89]	[-7.39 12.06]	[-6.45 13.06]
hip ab-adduction moment [%Bw m]	[-9.39 2.05]	[-9.44 2.55]	[-9.18 1.63]
hip intra-extra rotation moment [%Bw m]	[-1.89 0.35]	[-0.87 1.22]	[-1.32 1.02]
knee flexion-extension moment [%Bw m]	[-4.38 3.43]	[-3.34 7.52]	[-4.05 6.77]
ankle dorsi-plantar flexion moment [%Bw m]	[-9.11 1.76]	[-7.62 2.39]	[-7.51 1.83]

Figure 4.26: On the rows the average hip joint flexion-extension, ab-adduction and intra-extra rotation moments (solid line) with relative standard deviations (dashed line) obtained using the three models under study: gait2392, LLLM, LLLM2.In last column the mean values obtained with the three models have been overlapped to ease the visual comparison.

Joint Reaction Analysis results

The resultant of the hip contact forces computed using the three models is shown in Figure 4.27. As for subjects SF1 and SM4, mean orientation and magnitude of the resultant components in the sagittal, frontal and transversal planes were extracted at the two peak instants (Figures 4.29 and 4.30). Regarding the orientation of HCF at the first peak shown in Figure 4.29, it can be observed that on the sagittal the orientation of the predictions do not significantly differ. From the frontal and transversal plane plots it can be inferred that the LLLM2 HCF prediction is the most medially oriented followed by LLLM and gait2392. At the second peak, instead, the prediction appear very close to one another on all the planes. Finally, from the boxplots of the distribution of the two peak magnitudes of predicted HCFs over the entire set of walking trials (Figure 4.28), it can be observed that while at the first peak LLLM and LLLM2 predict similar median HCFs magnitudes (respectively $202\%BW$ and $207\%BW$), gait2392 prediction is $70\%BW$ higher. At the second peak, instead, the lowest median HCF ($441\%BW$) is predicted by LLLM; LLLM2 and gait2392 predicted HCFs are respectively $175\%BW$ and $161\%BW$ higher. It is worth noticing the higher number of outliers with respect to other subjects, thus confirming the low consistency of the walking in this experimental session.
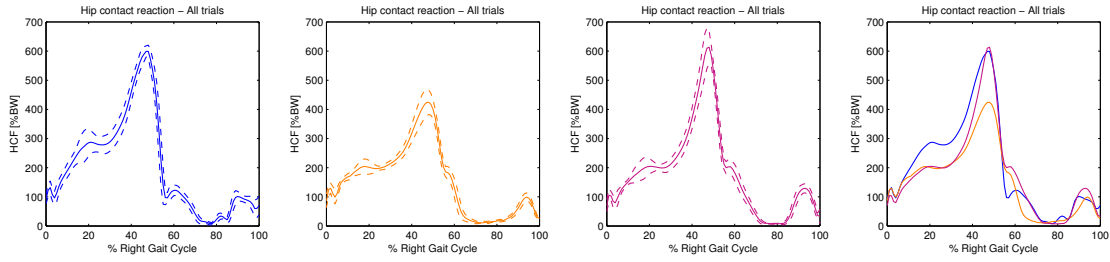
Figure 4.27: Average hip contact forces resultant through the gait cycle with relative standard deviations. On each column is shown the resultant obtained using one of the three models under study: gait2392, LLLM, LLLM2. In last column the mean values obtained with the three models have been overlapped to ease the visual comparison.

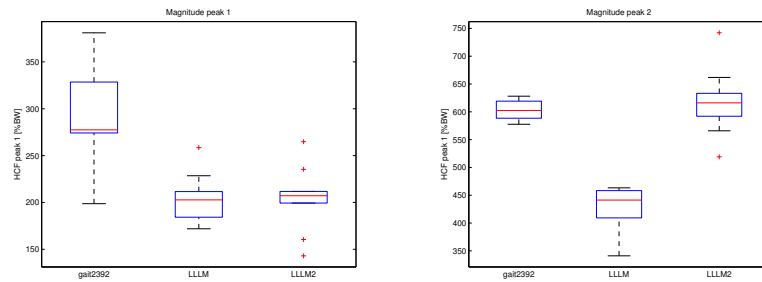**Figure 4.28:** Boxplots showing the distribution of the magnitudes of predicted HCF (with gait2392, LLLM and LLLM2 models) at the two main peak instants.

Figure 4.29: Average orientation (± standard deviation in dashed line) and magnitude of the components of HCF in the sagittal, frontal and transversal plane **at the first peak**. Computed using gait2392, LLLM, LLLM2. Positive orientations of X,Y and Z components correspond respectively to posterior-anterior, distal-proximal and medio-lateral direction.

Static Optimization results

Being available the EMG signals recorded during the walking trials of subject SM7, it is possible to compare EMGs (normalized by the highest value extracted
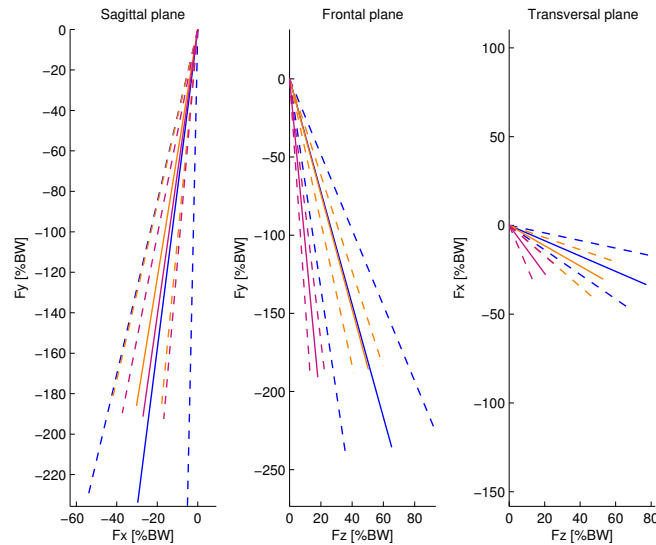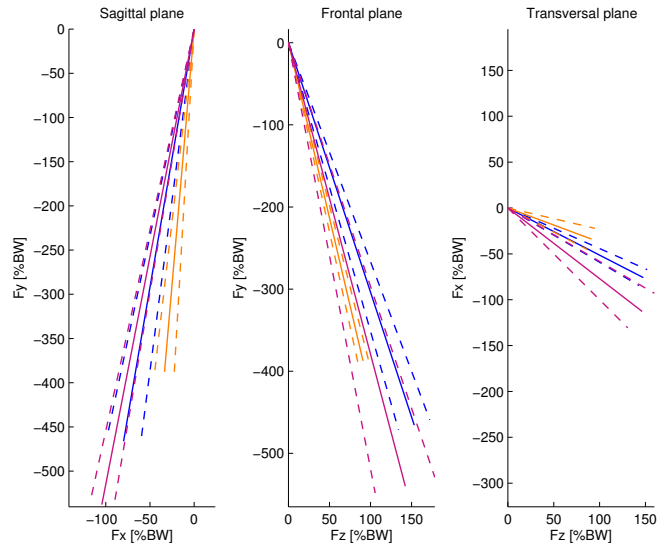
Figure 4.30: Average orientation (± standard deviation in dashed line) and magnitude of the components of HCF in the sagittal, frontal and transversal plane **at the second peak**. Computed using gait2392, LLLM, LLLM2. Positive orientations of X,Y and Z components correspond respectively to posterior-anterior, distal-proximal and medio-lateral direction.

from maximum voluntary contraction tasks) with muscle bundles activation. The latter (output of OpenSim Static Optimization tool) is computed as the predicted muscle force divided by the maximum isometric force. In Figures 4.31 and 4.32 are reported, as an example, predicted muscle activation plotted against EMG respectively from the second and the seventh walking trial. It must be brought to attention that the quality of EMG recordings of the *rectus femoris*, *tensor fascia latae* and *soleus* was poor and, therefore, EMG signals given in [Perry,1992] were used as reference EMGs for those muscles. In order to measure the similarity between EMG and each model's muscle activation prediction, their cross-correlation was computed (Table 5.4). For muscles represented with multiple bundles, the overall muscle activation to be cross-correlated with the EMG was computed as the sum of bundles activations.

(a) Rectus femoris*

(b) Vastus lateralis

(c) Vastus medialis

(d) Semitendinosus

(e) Biceps femoris long head

(f) Tensor fascia latae*

(g) Gastrocnemius medialis

(h) Gastrocnemius lateralis

(i) Soleus*

(j) Tibialis anterior

Figure 4.31: EMG signals (shaded gray area) against gait2392, LLLM, LLLM2 predicted muscle bundles activations for **walking trial 2**.

(a) Rectus femoris*

(b) Vastus lateralis

(c) Vastus medialis

(d) Semitendinosus

(e) Biceps femoris long head

(f) Tensor fascia latae*

(g) Gastrocnemius medialis

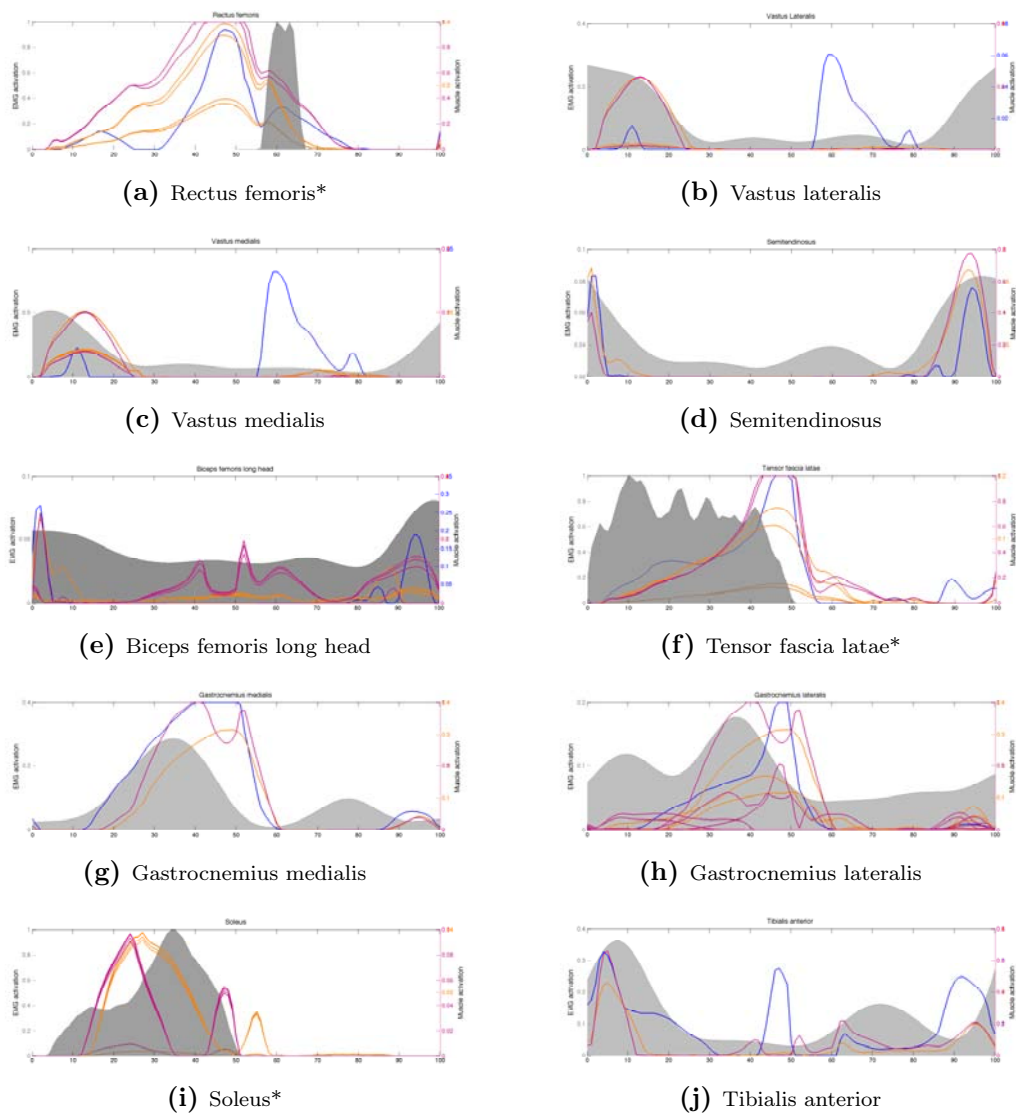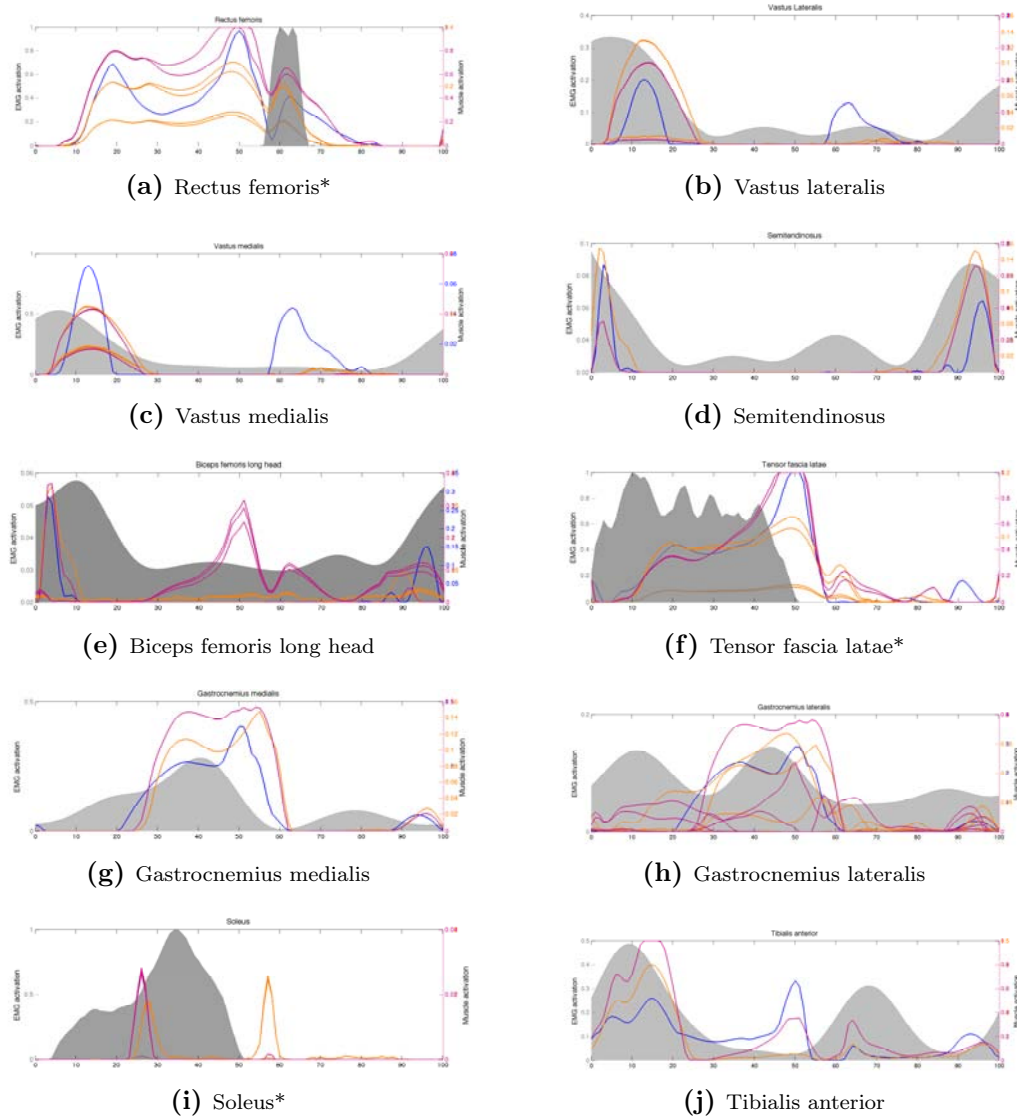**(h)** Gastrocnemius lateralis

(i) Soleus*

(j) Tibialis anterior

Figure 4.32: EMG signals (shaded gray area) against gait2392, LLLM, LLLM2 predicted muscle bundles activations for **walking trial 7**.

Table 4.4: Mean cross-correlation (between EMG and muscle activation predicted with each of the three models) $\pm$ standard deviation computed over 10 trials.

Cross correlation R	gait2392	LLLM	LLLM2
$R_{\text{rectus femoris}}$*	0.70 $\pm$ 0.06	0.78 $\pm$ 0.03	0.89 $\pm$ 0.02
$R_{\text{rastus lateralis}}$	0,41 $\pm$ 0,16	0.77 $\pm$ 0.06	0.76 $\pm$ 0.06
$R_{\text{rastus medialis}}$	0.40 $\pm$ 0.13	0.72 $\pm$ 0.13	0.7 $\pm$ 0.14
$R_{\text{semitendinosus}}$	0.6 $\pm$ 0.07	0.71 $\pm$ 0.32	0.64 $\pm$ 0.05
$R_{\text{biceps femoris}}$	0.52 $\pm$ 0.07	0.84 $\pm$ 0.02	0.7 $\pm$ 0.09
$R_{\text{tensor fascia latae}}$*	0.34 $\pm$ 0.02	0.35 $\pm$ 0.03	0.3 $\pm$ 0.02
$R_{\text{gastrocnemius medialis}}$	0,81 $\pm$ 0.04	0.69 $\pm$ 0.05	0.76 $\pm$ 0.04
$R_{\text{gastrocnemius lateralis}}$	0.71 $\pm$ 0.05	0.78 $\pm$ 0.07	0.74 $\pm$ 0.07
R_{soleus}*	0.41 $\pm$ 0.18	0.43 $\pm$ 0.05	0.3 $\pm$ 0.11
$R_{\text{tibialis anterior}}$	0.78 $\pm$ 0.08	0.78 $\pm$ 0.09	0.75 $\pm$ 0.09
mean(R):	(0.5686)	(0.6865)	(0.6502)

4.4 Discussion

With respect to the inverse kinematics results presented for each subject, it is worth commenting on the evident differences in the ranges of joints kinematics. This inconsistency is due to two factors. Firstly, while LLLM and LLLM2 model implement for each body segment the reference system recommended in [Wu,2002], neither the definition of segments reference systems nor the order of successive rotations (necessary to define for the hip joint coordinates) of gait2392 have been specified in [Delp,1990] and may differ from the previous ones. Secondly, the three models under study describe differently the foot kinematics: gait2392 accounts for ankle, subtalar and metatarsophageal joints kinematics; LLLM, for the reasons described in 1.3, accounts only for the ankle kinematics; finally LLLM2 includes both the ankle and subtalar joints. These discrepancies yielded different results ranges but the actual movement has been visually checked to be overall consistent through the different models to exclude abnormalities. Moreover, it should be taken into consideration that each model has a different initial pelvic tilt that inevitably affects the hip flexion-extension angle. This is another cause of the apparent inconsistency between the models results.

The aforementioned slight differences in computed joint kinematics minimally affected also the inverse dynamics results. In particular, being the hip joint at the top of the kinetic chain, all small differences noticed between the models at the ankle and at the knee result at the hip as amplified. However, it can be observed that large range discrepancies in the joints kinematics entailed small differences

in the joint moments, thus intuitively confirms the overall exactness of inverse kinematics results irrespective of the used model. Another small source of variance in the inverse dynamics results could be the different mass distribution that each scaled-model was subjected to: as explained in 3.2 each segment was scaled of the same factor with which its size was scaled, factor which is different among the models.

Regarding the joint reaction analysis, from Figure 4.33 a visual comparison can be drawn between the mean magnitude of hip contact forces (HCFs) computed over the set of three subjects (SF1, SM4 and SM7) with each of the models under study and the experimental HCFs ranges from [Bergmann,2001]. The set of subjects with instrumented hip involved in the study had the following characteristics: age 62 $\pm$ 11, years 51-78, BMI 29.0 $\pm$ 2.65. Bergmann's data range of values (gray filled area) was extracted from HIP98 dataset (www.orthoload.com) by averaging the upper and lower bounds of HCFs from all subjects' normal walking trials. In Figure 4.34(a) and (b) the boxplots of HCFs magnitudes respectively at the first and second peak are shown. At the first peak all models median predictions lie in the experimental range, whereas at the second peak our simulations confirmed the issue reported also in [Wesseling,2014]: all the models tend to overestimate the second peak magnitude corresponding to the push-off time instant. However, it must be reported that for two of the four subjects of Bergmann's dataset a visible second peak was completely absent and, therefore they were not included in the boxplot of Figure 4.34(b).

To try to understand the lower magnitude reached by mean HCFs resultant computed with LLLM model with respect to other models, a muscle moment arm analysis was run. The moment arm r is a measure of the effectiveness with which a muscle contraction generates a torque about the joint it spannes and it can be computed as $r = dl/d\theta$ where dl is the change in the length of muscle path and $d\theta$ is the variation of the joint coordinate θ. To give an example, being θ the hip flexion angle, in correspondence of the extension (positive variation in θ) of the hip, we expect the moment arm r of an extensor muscle ($dl < 0$) to be negative. What we noticed is that in LLLM four of the six superior bundles of gluteus maximus act as flexors ($r > 0$) as shown in Figure 4.35.

To further analyze the peak predictions in comparison with HIP98 dataset, the mean orientations of HCFs at the two peaks were extracted from both the HIP98 data (also in this case, when looking at the second peak, only the two subjects showing a second peak in the HCFs were taken into consideration) and the HCFs obtained using the three models. From Figure 4.36 it can be observed the overall
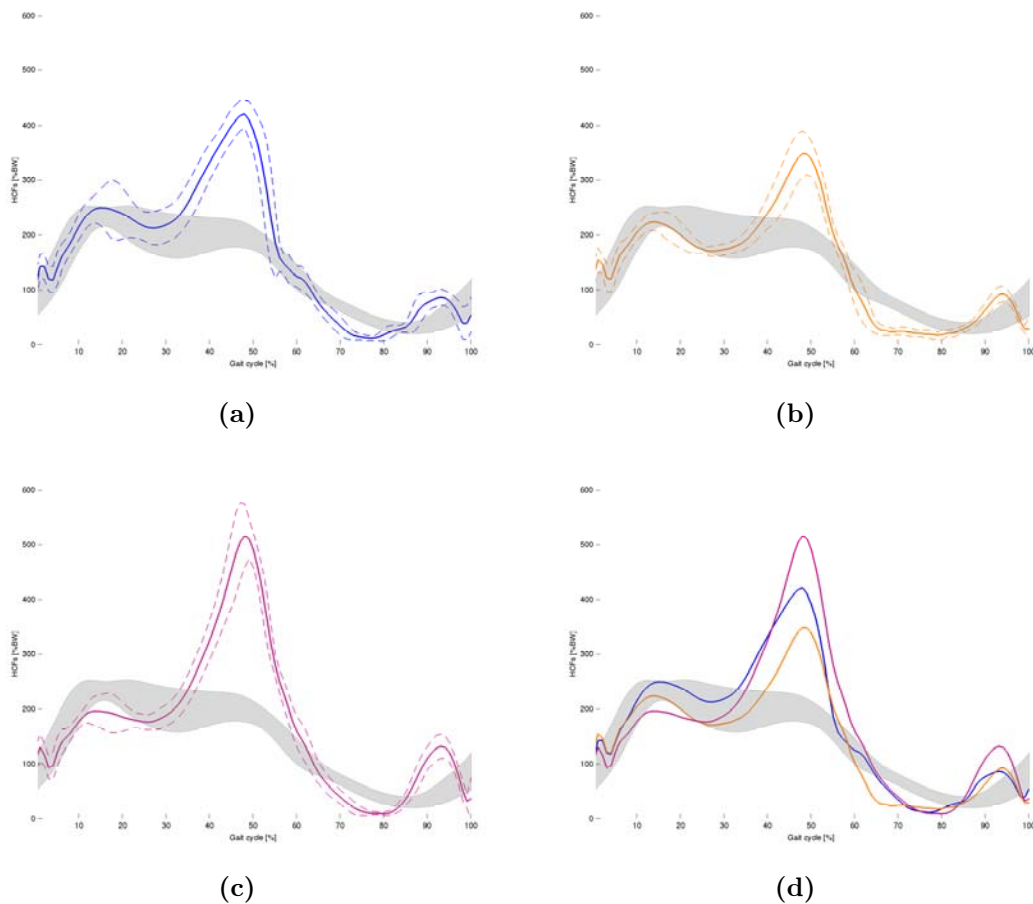
Figure 4.33: Average HCFs magnitudes (solid lines) with relative standard deviations (dashed lines) through the gait cycle predicted using gait2392 (a) LLLM (b), LLLM2 (c) plotted against experimental ranges (gray filled area) from HIP98. In (d) all the mean magnitudes have been plotted together to ease the visual comparison.
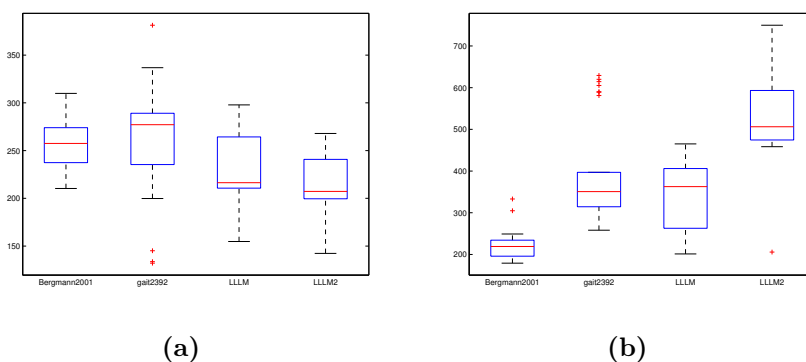

Figure 4.34: Boxplots showing the distribution of the magnitudes of experimental and predicted HCF (with gait2392, LLLM and LLLM2 models) at the first (a) and at the second peak (b).
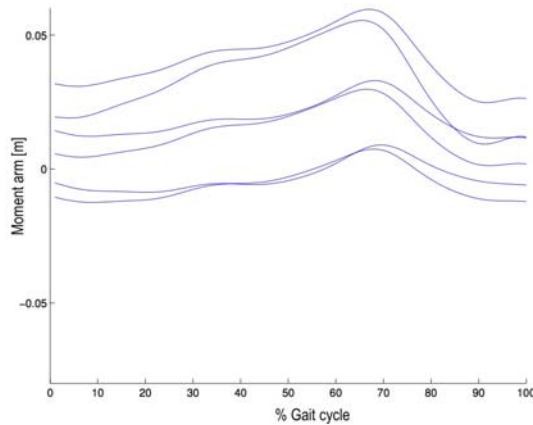
Figure 4.35: Gluteus maximus superior bundles moment arm trajectory through the gait cycle.

similarity of the orientation of the experimental HCFs and the predicted ones at the first peak, in particular for LLLM2. From Figure 4.37, instead, it is evident the totally incorrectness of the predicted HCFs orientations: while the predicted components turn out to be laterally oriented (positive direction of Z-component), the experimental components are instead medially oriented (negative direction of Z-component). Intuitively this may be due a wrong action of adductor muscles in that phase of the gait cycle. More specifically, probably more attention should be paid in the design of *ileo-psoas* path which is the adductor with the highest maximum isometric force.

To make a numerical comparison between the results of different models, the following indexes were computed:

- Root mean square error (RMSE) between the average HCFs predicted with the three musculoskeletal models and the average experimental HCFs,

- Cross-correlation (R) between the average HCFs predicted with the three musculoskeletal models and the average experimental HCFs,

- mean difference between average experimental first peak and all predicted first peaks (P1diff) –where a negative value means that the model is overestimating that magnitude and viceversa–,

- mean difference between average experimental second peak and all predicted second peaks (P2diff)

- angular distances between experimental and predicted HCFs on the frontal and the transversal plane at the first peak (P1angdist) –where a positive value yields an anticlockwise angular increase with respect to the experimental orientation and viceversa–,
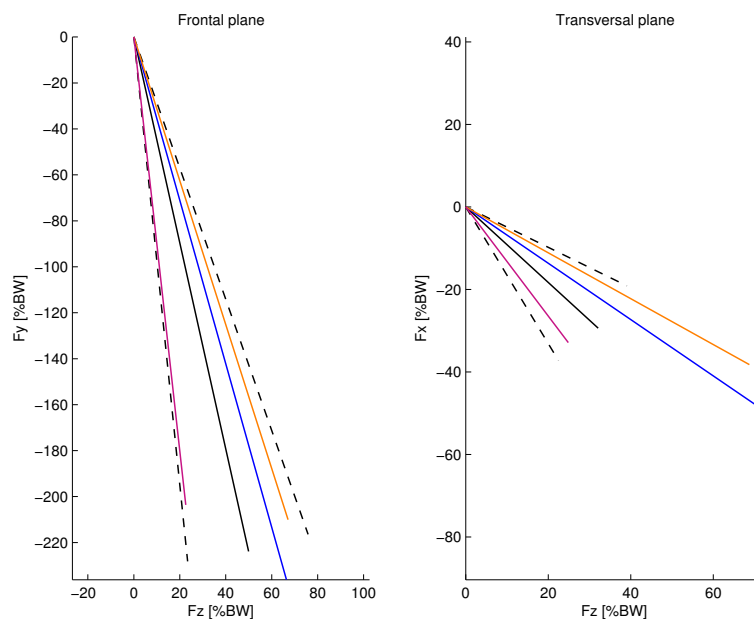
Figure 4.36: Average orientation and magnitude of the components of HCF in the frontal and transversal plane **at the first peak** computed from HIP98 dataset(mean±sd) and using gait2392, LLLM, LLLM2. Positive orientations of X,Y and Z components correspond respectively to posterior-anterior, distal-proximal and medio-lateral direction.
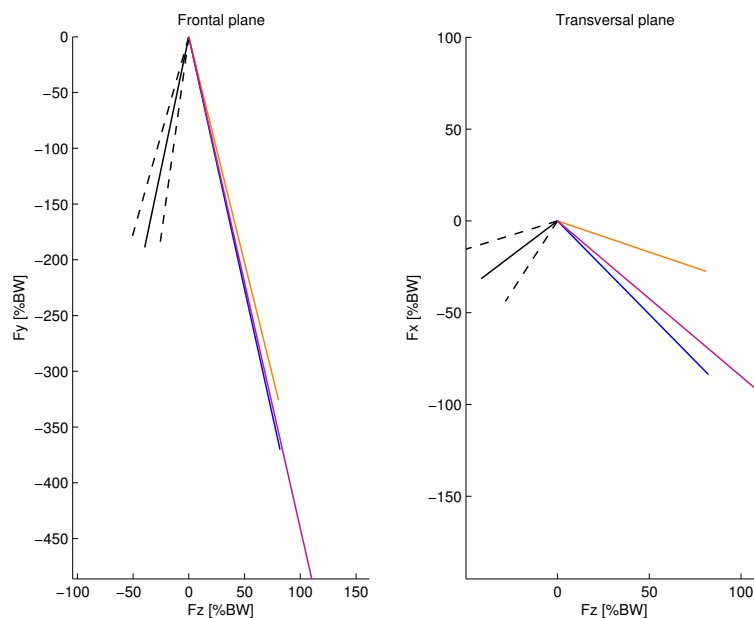

Figure 4.37: Average orientation and magnitude of the components of HCF in the frontal and transversal plane **at the second peak** computed from HIP98 dataset(mean±sd) and usinggait2392, LLLM, LLLM2. Positive orientations of X,Y and Z components correspond respectively to posterior-anterior, distal-proximal and medio-lateral direction.

- angular distances between experimental and predicted HCFs on the frontal and the transversal plane at the second peak (P2angdist).

From the results reported in Table 5.5 it can be observed that LLLM shows respectively the lowest RMSE and the highest cross-correlation coefficient R, while both gait2392 and LLLM2 predictions reach higher RMSE values and lower cross-correlation coefficient probably due to the extremely high overestimation of the second peak with respect to the experimental valued. It can also be stated that all the models give reasonable predictions of the first peak magnitude and orientation, but noone of them catches medial orientation of the resultant at the second peak.

Table 4.5: Indexes extracted to draw a numerical comparison between gait2392, LLLM and LLLM2.

	gait2392	LLLM	LLLM2
RMSE [%BW]	80.94	52.03	105.69
R	0.95	0.96	0.90
P1diff [%BW]	-3.92	24.32	40.76
P2diff [%BW]	-174.14	-124.94	-301.2
P1angdist on frontal pl. [°]	+8	+10	-10
P1angdist on transv pl. [°]	+11	+17	-11
P2angdist on frontal pl. [°]	+25	+26	+25
P2 angdist transv pl. [°]	+100	+127	+107

Finally, it is worth briefly commenting on the static optimization results of subject SM7. Even if from Table 4.4, given the highest mean cross-correlation between its muscles activation and EMG recordings, it could be inferred that LLLM is the model which yields a muscle activation pattern closest to reality, it should be taken into account that EMG recordings were not available for the gluteal muscles (the main difference between LLLM and LLLM2), therefore to be realistic, this kind of assessment should be repeated with a complete set of EMG recordings.

Chapter 5

Stair climbing task: results and discussion

In this chapter all the results obtained following the methods described in Chapter 3 will be presented separately for each subject performing the stair climbing task. For each subject the resulting coordinate trajectories, the moments at the joints and, finally, the hip joint contact forces will be shown. For subject SM7, also the qualitative comparison between muscle activation and EMG signals will be shown.

5.1 Subject SF1

The subject SF1 (female, weight: $54.1Kg$, height: $165.5cm$) has performed the stair climbing trials with an average speed of $0.55m/s$ computed as the stride length (shown in Figure 5.1) divided by the stride time (time between the two consecutive right heel strikes).

Inverse Kinematics results

The coordinate trajectories for ankle, knee and hip joints computed with the three musculoskeletal models are shown in Figures 5.2, 5.3 and 5.4.
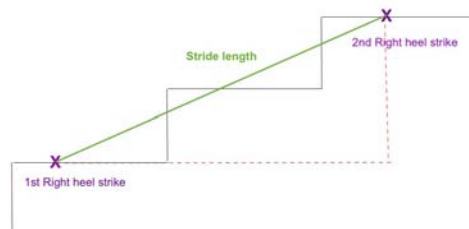

Figure 5.1: The stride length for the stair climbing task was computed as the length of the segment linking the two right heel strike positions.
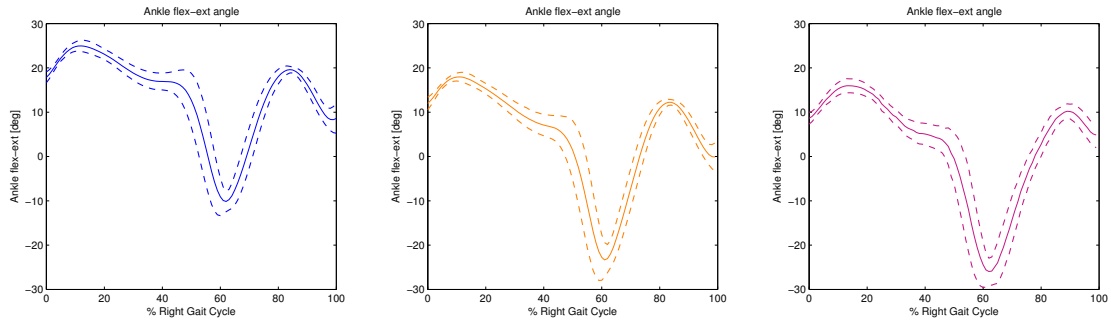
Figure 5.2: Average ankle joint dorsi-plantar flexion angle trajectory (solid line) through the gait cycle with relative standard deviations (dashed line) obtained using gait2392, LLLM, LLLM2.
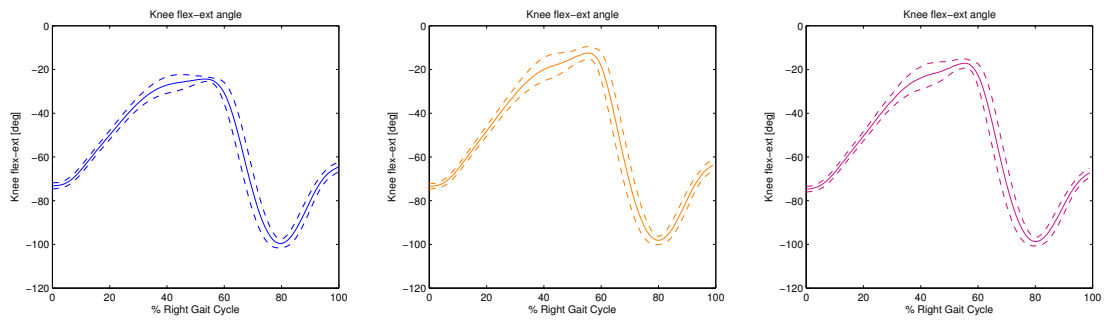

Figure 5.3: Average knee joint flexion-extension angle trajectory (solid line) through the gait cycle with relative standard deviations (dashed line) obtained using gait2392, LLLM, LLLM2.
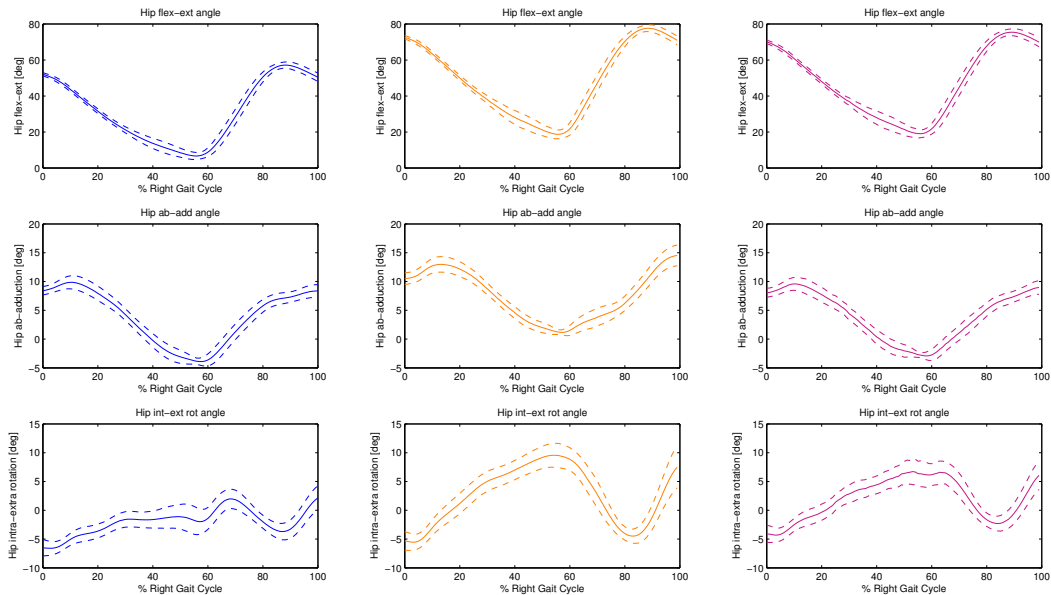

Figure 5.4: On the rows the average hip joint flexion-extension, ab-adduction and intra-extra rotation angles trajectories (solid line) through the gait cycle with relative standard deviations (dashed line) obtained using the three models under study: gait2392, LLLM, LLLM2.

Inverse Dynamics results

The moments acting at the ankle, knee and hip joint are shown in Figures 5.5, 5.6 and 5.7. Observing the results – and in particular the ranges reported in Table 5.4–, it can be stated that, apart from hip flexion moment computed with gait2392, the other resulting moments are almost independent from the model used to perform the evaluation.
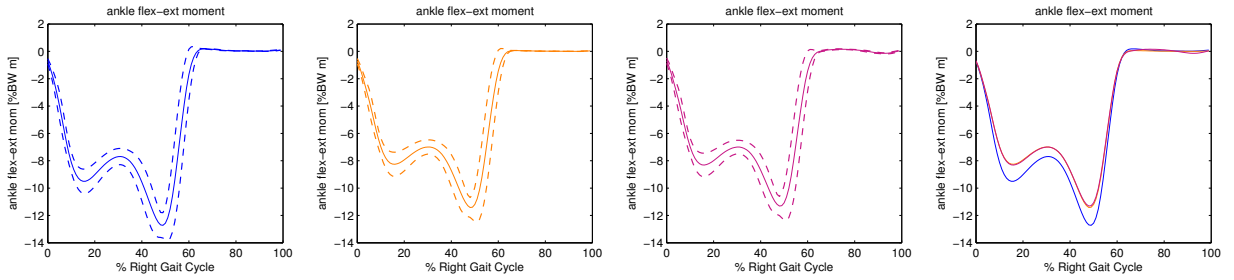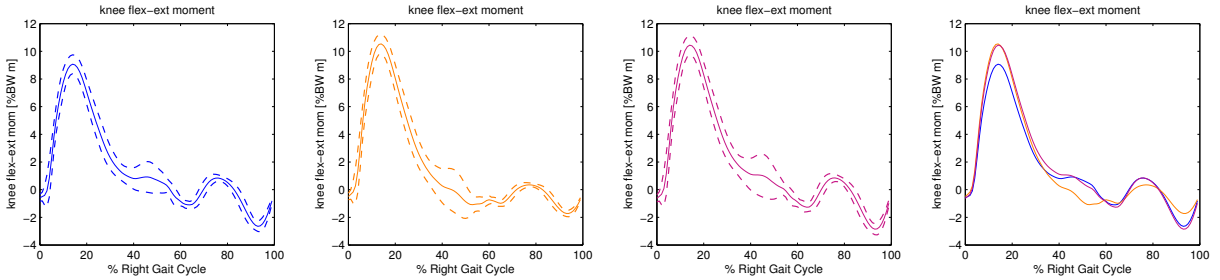

Figure 5.5: Average ankle joint dorsi-plantar flexion moments (solid line) with relative standard deviations (dashed line) obtained using the three models under study: gait2392, LLLM, LLLM2.

Figure 5.6: Average knee joint dorsi-plantar flexion moments (solid line) with relative standard deviations (dashed line) obtained using the three models under study: gait2392, LLLM, LLLM2.

Table 5.1: Ranges [min max] reached by the moments acting on the hip, knee and ankle when computed with the three different models

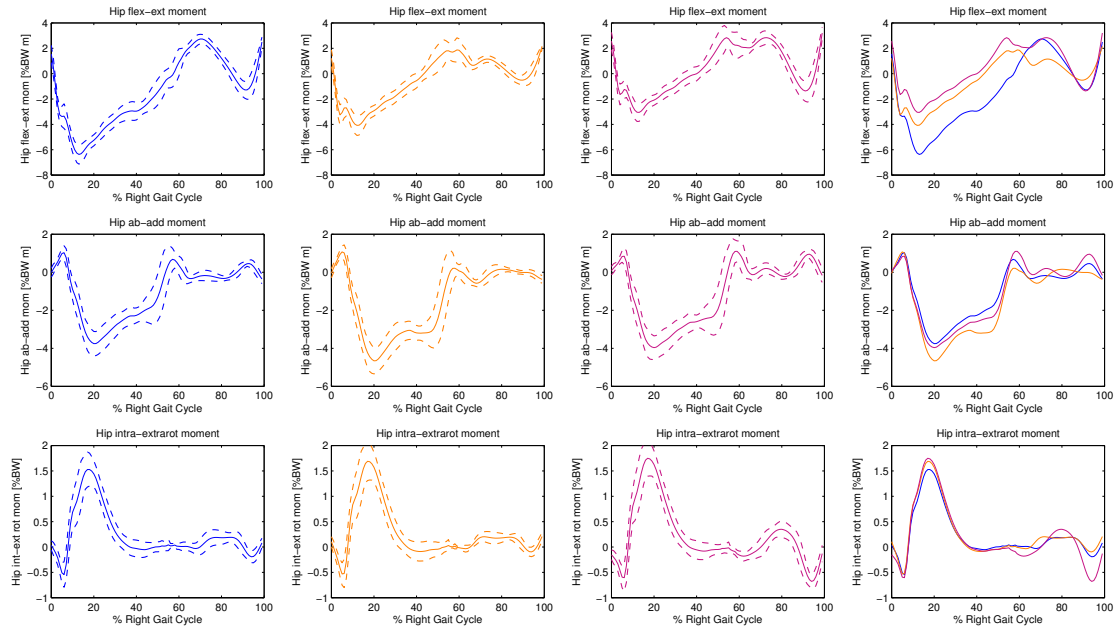|	gait2392	LLLM	LLLM2
hip flexion-extension moment [%Bw m]	[-6.37 2.73]	[-4.08 2.1581]	[-3.06 3.21]
hip ab-adduction moment [%Bw m]	[-3.76 1.03]	[-4.66 1.07]	[-3.97 1.11]
hip intra-extra rotation moment [%Bw m]	[-0.54 1.53]	[-0.53 1.69]	[-0.68 1.75]
knee flexion-extension moment [%Bw m]	[-2.65 9.07]	[-1.72 10.53]	[-2.85 10.44]
ankle dorsi-plantar flexion moment [%Bw m]	[-12.72 0.18]	[-11.42 0.05]	[-11.31 0.15]

Figure 5.7: On the rows the average hip joint flexion-extension, ab-adduction and intra-extra rotation moments (solid line) with relative standard deviations (dashed line) obtained using the three models under study: gait2392, LLLM, LLLM2.In last column the mean values obtained with the three models have been overlapped to ease the visual comparison.

Joint Reaction Analysis results

The resultant of hip contact forces (HCFs) computed using the three models is shown in Figure 5.8. As for the walking trials, mean orientation and magnitude of the resultant components in the sagittal, frontal and transversal planes were extracted are reported in Figures 5.10 and 5.11. Finally, in the boxplots of Figure 5.9 is examined the distribution of the magnitudes of predicted HCF (with the three models) at the two peaks over the entire set of walking trials.

It can be observed that while median HCFs predicted by gait2392 and LLLM reach respectively 268 and 257%BW at the first peak, LLLM2 prediction reaches the lower value of 222%BW. The differences among the models predictions is smaller at the second peak where gait2392, LLLM and LLLM2 reach respectively a median value of 170%BW, 175%BW and 155%BW.

Regarding the orientation of HCF at the first peak (Figure 5.10), it is evident that main differences occur in the frontal and transversal plane, where LLLM2 predicts the most medially oriented HCF followed by gait2392 and LLLM. At the second peak again the main differences occur in the frontal and transversal plane where observations previously made are confirmed.
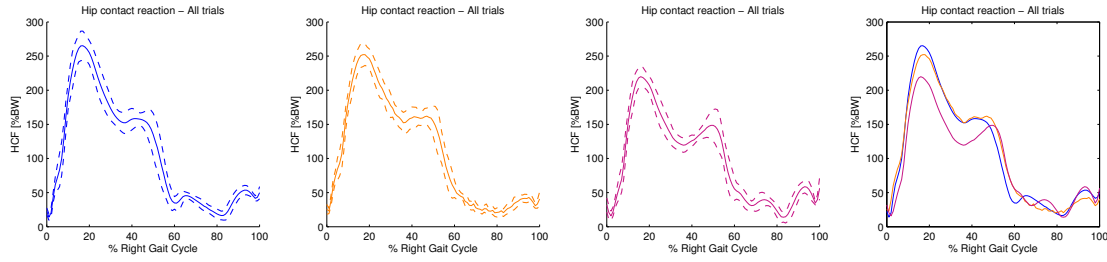
Figure 5.8: Average hip contact forces resultant through the gait cycle with relative standard deviations. On each column is shown the resultant obtained using one of the three models under study: gait2392, LLLM, LLLM2. In last column the mean values obtained with the three models have been overlapped to ease the visual comparison.

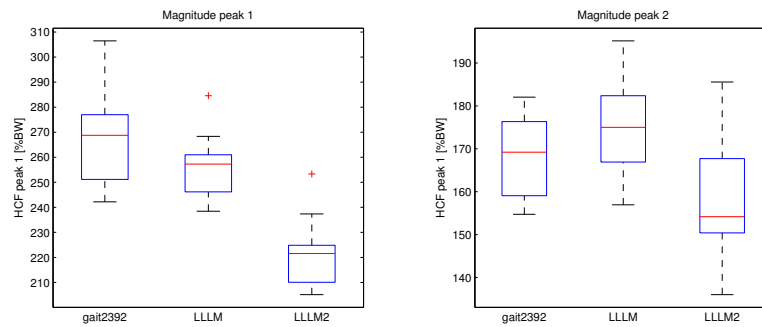**Figure 5.9:** Boxplots showing the distribution of the magnitudes of predicted HCF (with gait2392, LLLM and LLLM2 models) at the two main peak instants.
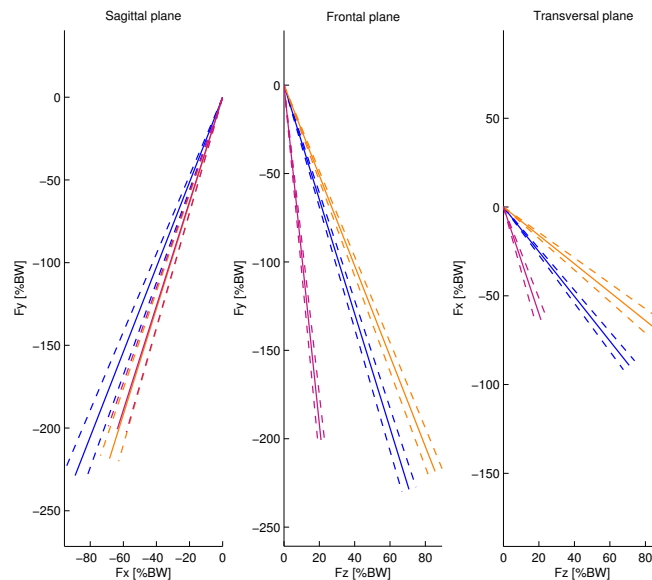

Figure 5.10: Average orientation (± standard deviation in dashed line) and magnitude of the components of HCF in the sagittal, frontal and transversal plane **at the first peak**. Computed using gait2392, LLLM, LLLM2. Positive orientations of X,Y and Z components correspond respectively to posterior-anterior, distal-proximal and medio-lateral direction.

Figure 5.11: Average orientation (± standard deviation in dashed line) and magnitude of the components of HCF in the sagittal, frontal and transversal plane **at the second peak**. Computed using gait2392, LLLM, LLLM2. Positive orientations of X,Y and Z components correspond respectively to posterior-anterior, distal-proximal and medio-lateral direction.
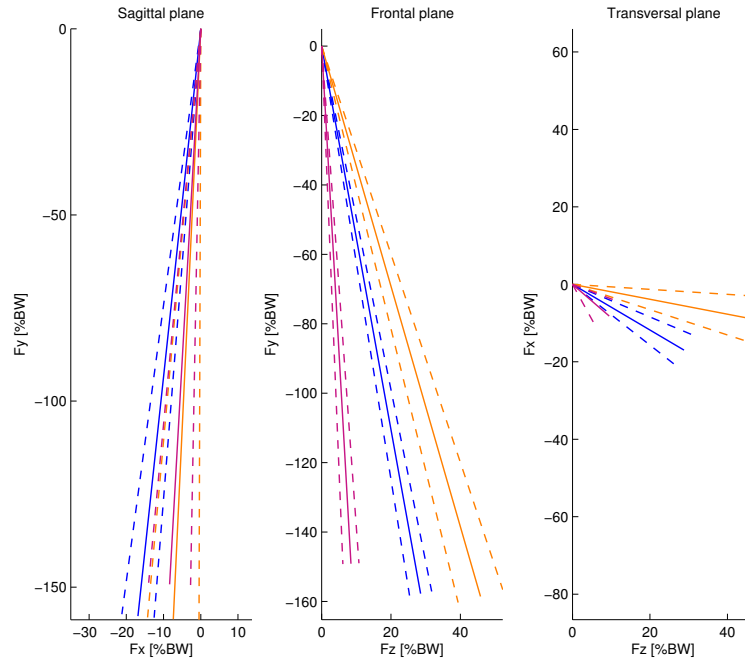
5.2   Subject SM4

The subject SM4 (male, weight: $84.5Kg$, height: $192cm$) has performed the stair climbing trials with an average speed of $0.53m/s$ computed as previously explained.

Inverse Kinematics results

The coordinate trajectories for ankle, knee and hip joints computed with the three musculoskeletal models are shown in Figures 5.12, 5.13 and 5.14. It must be noted for this subject, with respect to SF1 inverse kinematics results, the higher standard deviation ok ankle dorsi-plantar angle trajectory, probably due to a less natural way of walking of subject SM4 through the trials (less repeatability). As for the walking trials, the joint angles trajectories computed with the different models match by means of trends and do not match by means of amplitudes.
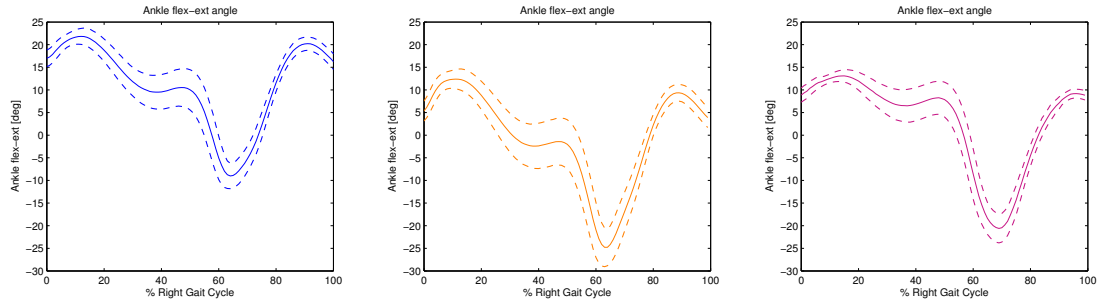
Figure 5.12: Average ankle joint dorsi-plantar flexion angle trajectory (solid line) through the gait cycle with relative standard deviations (dashed line) obtained using the three models under study: gait2392, LLLM, LLLM2.
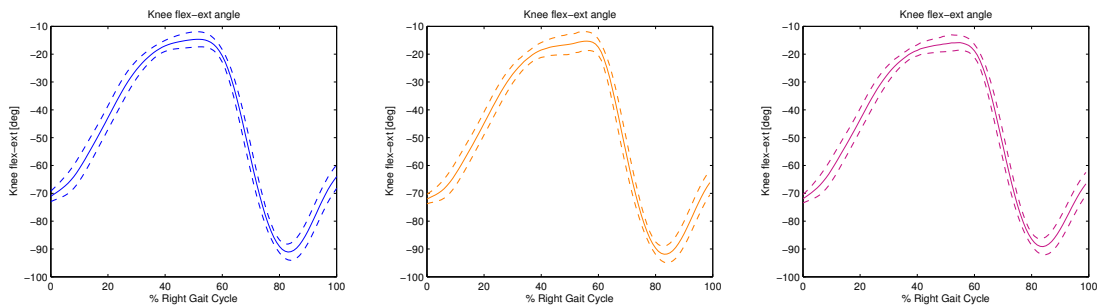

Figure 5.13: Average knee joint flexion-extension angle trajectory (solid line) through the gait cycle with relative standard deviations (dashed line) obtained using the three models under study: gait2392, LLLM, LLLM2.
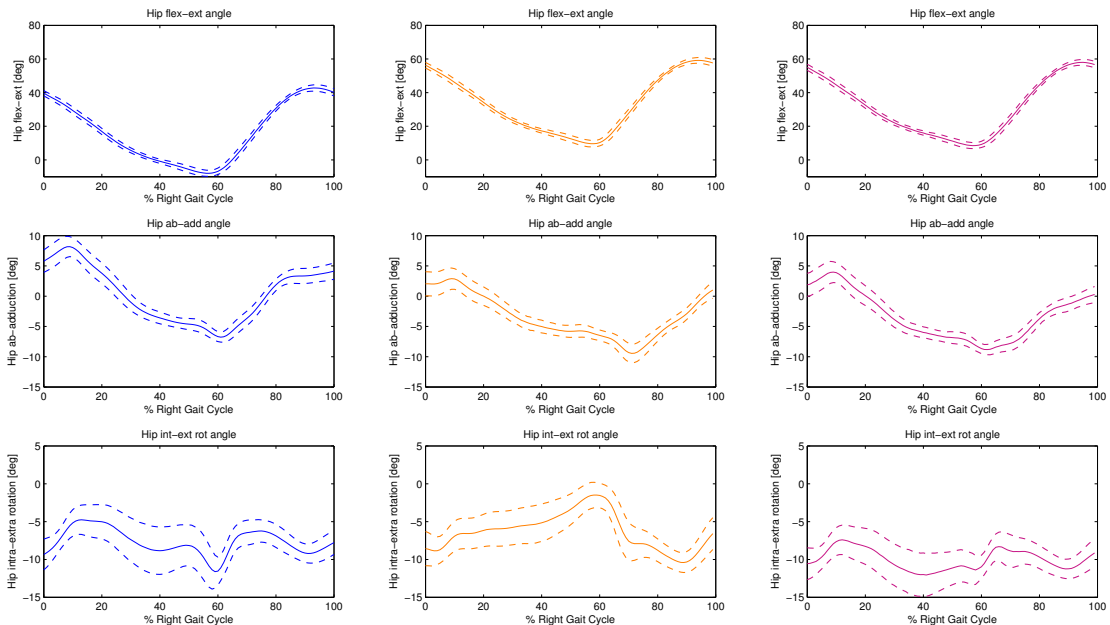

Figure 5.14: On the rows the average hip joint flexion-extension, ab-adduction and intra-extra rotation angles trajectories (solid line) through the gait cycle with relative standard deviations (dashed line) obtained using gait2392, LLLM, LLLM2.

Inverse Dynamics results

The moments acting at the ankle, knee and hip joint are shown in Figures 5.15, 5.16 and 5.17. Observing the results, it can be stated that the greatest differences between the models occur for the flexion extension moments of ankle, knee and hip were especially gait2392 reaches values of $2\%BWm$ lower than LLLM2 and $1\%BWm$ lower than LLLM. An interpretation to these results will be given in the Discussion section.
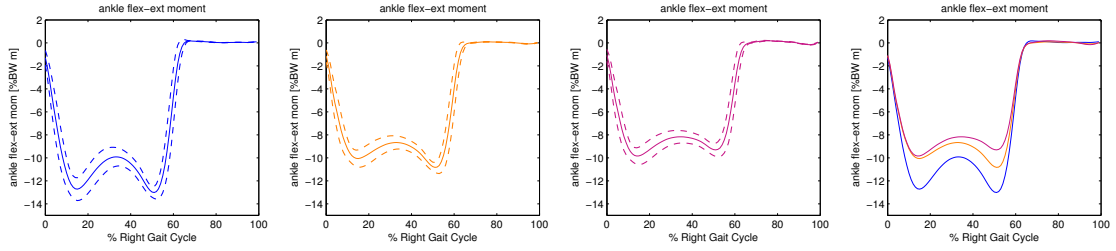

Figure 5.15: Average ankle joint dorsi-plantar flexion moment through the gait cycle with relative standard deviations. On each column is shown the result obtained using the three models under study: gait2392, LLLM, LLLM2.
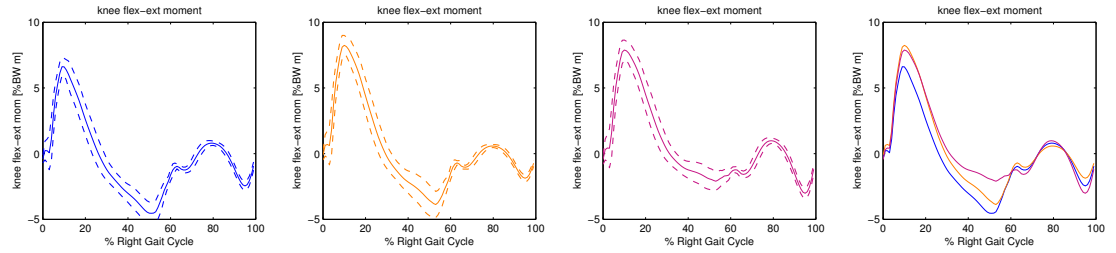

Figure 5.16: Average knee joint flexion-extension moment through the gait cycle with relative standard deviations. On each column is shown the result obtained using gait2392, LLLM, LLLM2.

Table 5.2: Ranges [min max] reached by the moments acting on the hip, knee and ankle when computed with the three different models

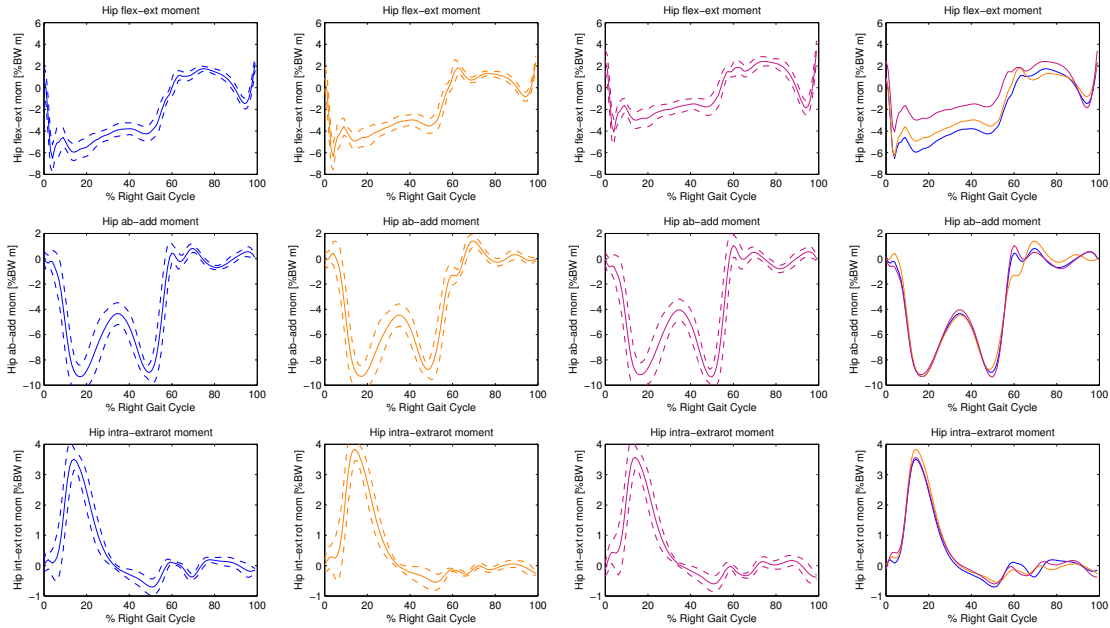|	gait2392	LLLM	LLLM2
hip flexion-extension moment [%Bw m]	[-6.53 2.29]	[-6.36 2.33]	[-4.09 3.4]
hip ab-adduction moment [%Bw m]	[-9.33 0.81]	[-9.31 1.39]	[-9.35 1.04]
hip intra-extra rotation moment [%Bw m]	[-0.71 3.51]	[-0.55 3.83]	[-0.6 3.57]
knee flexion-extension moment [%Bw m]	[-4.54 6.62]	[-3.87 8.25]	[-3.01 7.89]
ankle dorsi-plantar flexion moment [%Bw m]	[-13.01 0.17]	[-10.82 0.09]	[-9.84 0.19]

Figure 5.17: On the rows the average hip joint flexion-extension, ab-adduction and intra-extra rotation moments (solid line) with relative standard deviations (dashed line) obtained using the three models under study: gait2392, LLLM, LLLM2.In last column the mean values obtained with the three models have been overlapped to ease the visual comparison.

Joint Reaction Analysis results

The resultants of hip contact forces (HCFs) computed using the three models are shown in Figure 5.18. In the boxplots of Figure 5.19 is examined the distribution of the magnitudes of predicted HCF (with the three models) at the two peaks over the entire set of walking trials: it can be observed that while at the second peak the median predictions of HCF are all in a range of $30\%BW$, at the first peak gait2392 prediction exceeds LLLM and LLLM2 predictions respectively of $70\%BW$ and $190\%BW$. Regarding the orientation of HCFs, mean orientation and magnitude of the resultant components in the sagittal, frontal and transversal planes extracted at the two peak instants are shown in Figures 5.20 and 5.21. At the first peak (Figure 5.20), main differences occur on the frontal and transversal plane, where LLLM2 predicts the most medially oriented HCF followed by gait2392 and LLLM. At the second peak, instead, the gait2392 frontal plane component is the most posteriorly oriented while LLLM and LLLM2 predictions do not differ significantly. On the frontal plane, LLLM2 gives again the most medially oriented component.
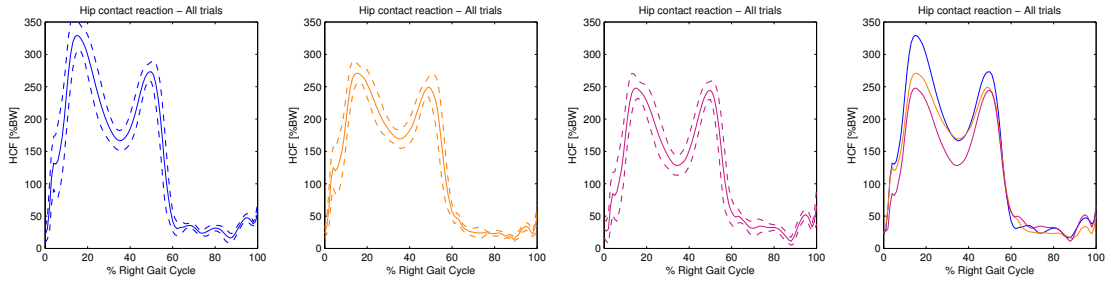
Figure 5.18: Average hip contact forces resultant through the gait cycle with relative standard deviations. On each column is shown the resultant obtained using one of the three models under study: gait2392, LLLM, LLLM2. In last column the mean values obtained with the three models have been overlapped to ease the visual comparison.
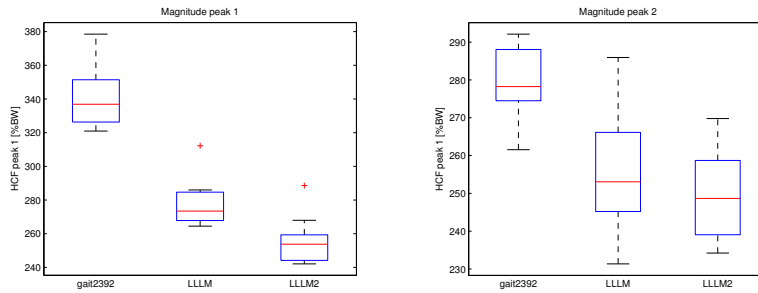
Figure 5.19: Boxplots showing the distribution of the magnitudes of predicted HCF (with gait2392, LLLM and LLLM2 models) at the two main peak frames.

Figure 5.20: Average orientation (± standard deviation in dashed line) and magnitude of the components of HCF in the sagittal, frontal and transversal plane at the first peak computed using gait2392, LLLM, LLLM2. Positive orientations of X,Y and Z components correspond respectively to posterior-anterior, distal-proximal and medio-lateral direction.

Figure 5.21: Average orientation (± standard deviation in dashed line) and magnitude of the components of HCF in the sagittal, frontal and transversal plane at the second peak computed using gait2392, LLLM, LLLM2. Positive orie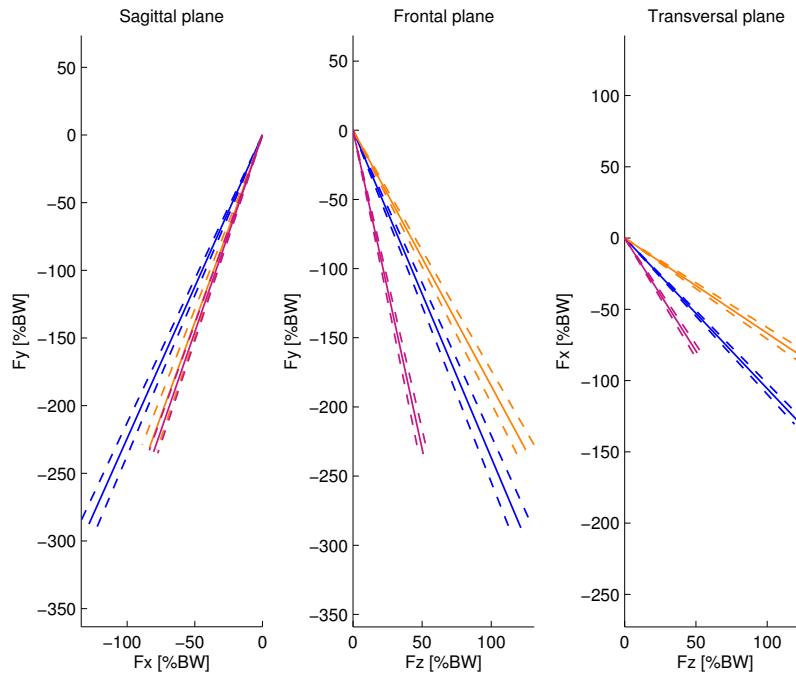ntations of X,Y and Z components correspond respectively to posterior-anterior, distal-proximal and medio-lateral direction.
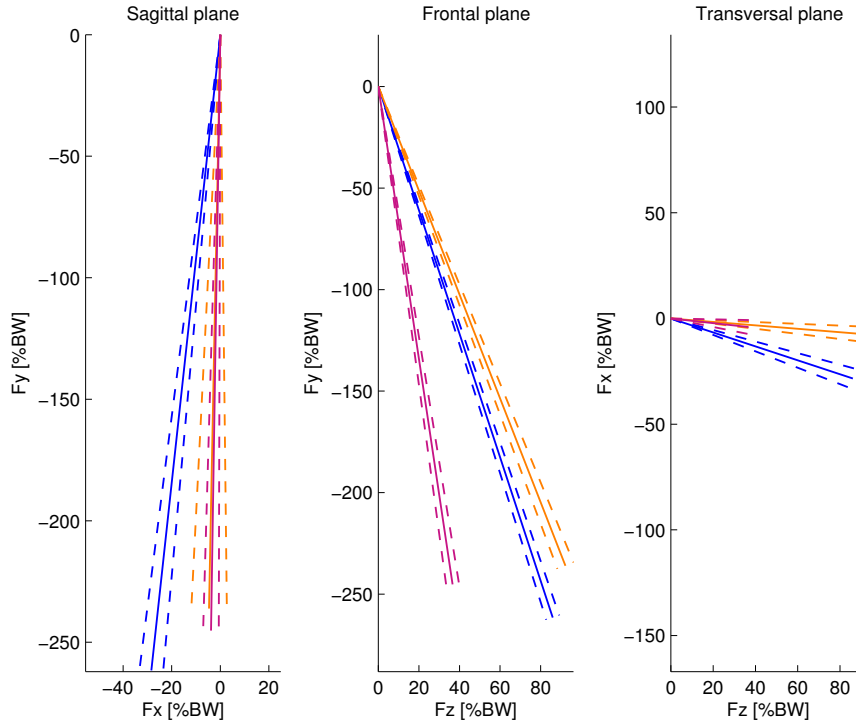
5.3 Subject SM7

The subject SM7 (male, weight: $90.8Kg$, height: $186cm$), whose experimental session has been described in Chapter 2, has performed the stair climbing trials with an average speed of $0.49m/s$. It is worth stressing that the subject was particularly compelled in the stair ascending by the limited dimensions of the steps, causing a not completely consistent gait pattern among the ten trials.

Inverse Kinematics results

The coordinate trajectories for ankle, knee and hip joints computed with the three musculoskeletal models are shown in Figures 5.22, 5.23 and 5.24. Also for subject SM7, there is a high standard deviation for ankle dorsi-plantar angle trajectory – as for SM4–probably due to a less natural way of climbing the stairs through the trials (less repeatability).
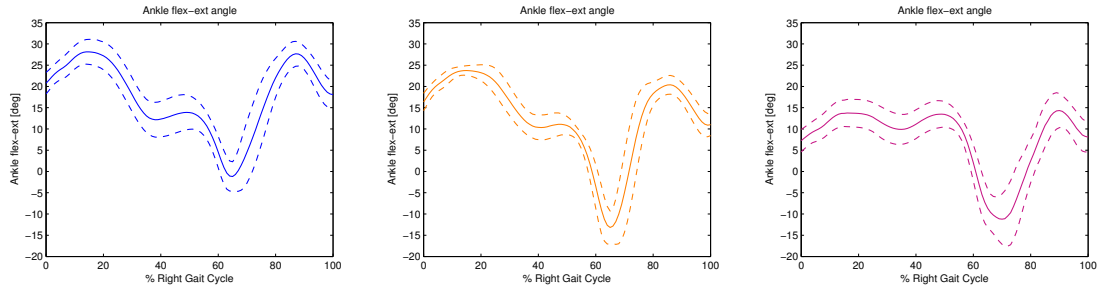
Figure 5.22: Average ankle joint dorsi-plantar flexion angle trajectory (solid line) through the gait cycle with relative standard deviations (dashed line) obtained using the three models under study: gait2392, LLLM, LLLM2.

Figure 5.23: Average knee joint flexion-extension angle trajectory (solid line) through the gait cycle with relative standard deviations (dashed line) obtained using the three models under study: gait2392, LLLM, LLLM2.

Figure 5.24: On the rows the average hip joint flexion-extension, ab-adduction and intra-extra rotation angles trajectories (solid line) through the gait cycle with relative standard deviations (dashed line) obtained using gait2392, LLLM, LLLM2.

Inverse Dynamics results

The moments acting at the ankle, knee and hip joint are shown in Figures 5.25, 5.26 and 5.27. It can be observed that, with respect to the ankle joint moment results shown for the other subjects (Figure 5.5 and Figure 5.15), for subject SM7 there is a wider distribution of the results yielding standard deviation up to $1.71\%BWm$, $1.51\%BWm$ $1.42\%BWm$ respectively for gait2392, LLLM and LLLM2. It is worth noticing the difference between gait2392 and the other models in the results of knee and hip flexion-extension moments where the blue lines that represent them are downward shifted of almost $4\%BWm$.
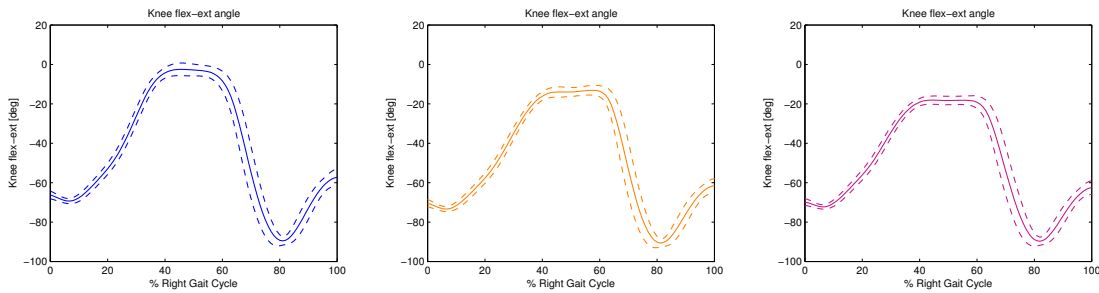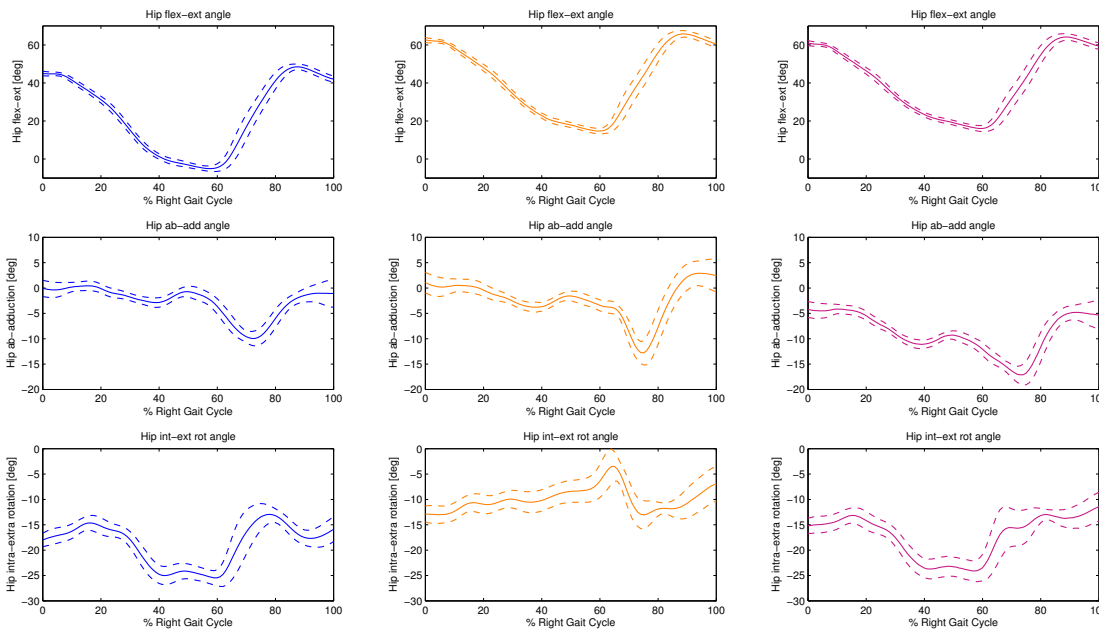

Figure 5.25: Average ankle joint flexion-extension moment through the gait cycle with relative standard deviations. On each column is shown the result obtained using gait2392, LLLM, LLLM2.

Figure 5.26: Average knee joint flexion-extension moment through the gait cycle with relative standard deviations. On each column is shown the result obtained using gait2392, LLLM, LLLM2.

Table 5.3: Ranges [min max] reached by the moments acting on the hip, knee and ankle when computed with the three different models

	gait2392	LLLM	LLLM2
hip flexion-extension moment [%Bw m]	[-5.74 2.80]	[-2.89 2.46]	[-2.74 4.36]
hip ab-adduction moment [%Bw m]	[-10.83 0.5]	[-11.22 1.41]	[-10.74 0.50]
hip intra-extra rotation moment [%Bw m]	[-1.42 6.14]	[-0.38 6.25]	[-0.81 5.57]
knee flexion-extension moment [%Bw m]	[-3.61 10.32]	[-1.51 13.02]	[-2.15 11.95]
ankle dorsi-plantar flexion moment [%Bw m]	[-7.07 0.15]	[-6.29 0.05]	[-5.23 0.18]
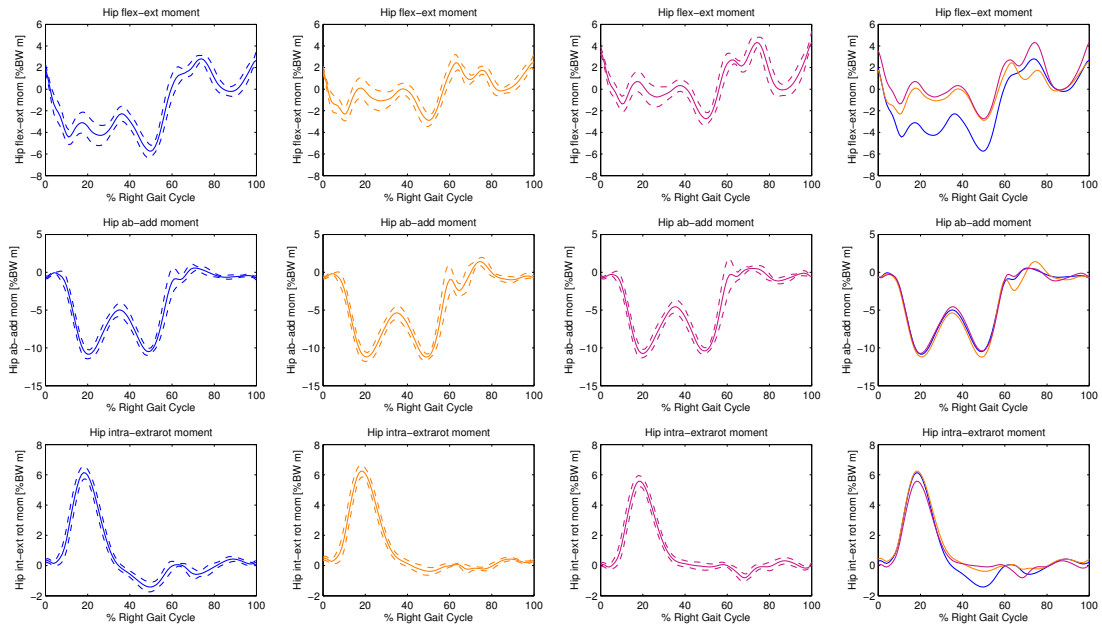
Figure 5.27: On the rows the average hip joint flexion-extension, ab-adduction and intra-extra rotation moments (solid line) with relative standard deviations (dashed line) obtained using the three models under study: gait2392, LLLM, LLLM2. In the last column the mean values obtained with the three models have been overlapped to ease the visual comparison.

Joint Reaction Analysis results

The resultant of hip contact forces (HCFs) computed using the three models is shown in Figure 5.28. Boxplots of Figure 5.29 examine the distribution of the magnitudes of predicted HCF (with the three models) at the two peaks over the entire set of walking trials. It can be observed that while at the first peak LLLM and LLLM2 predict similar mean HCF magnitudes (respectively $273\%BW$ and $315\%BW$), gait2392 prediction is $120\%BW$ higher. At the second peak this situation is confirmed, yielding amplitudes of $255\%BW$, $286\%BW$ and $409\%BW$ respectively for LLLM, LLLM2 and gait2392. Mean orientation and magnitude of the resultant components in the sagittal, frontal and transversal planes were extracted at the two peak instants and are shown in Figures 5.30 and 5.31)

Regarding the orientation of HCF at the first peak shown in Figure **??**, it can be observed that on the sagittal plane the orientation of the predictions does not significantly differ. From the frontal and transversal plane plots it can be inferred that the LLLM2 HCF prediction is the most medially oriented followed by LLLM and gait2392. At the second peak, gait2392 prediction appears as the most posteriorly oriented while LLLM2 is the most medially oriented.
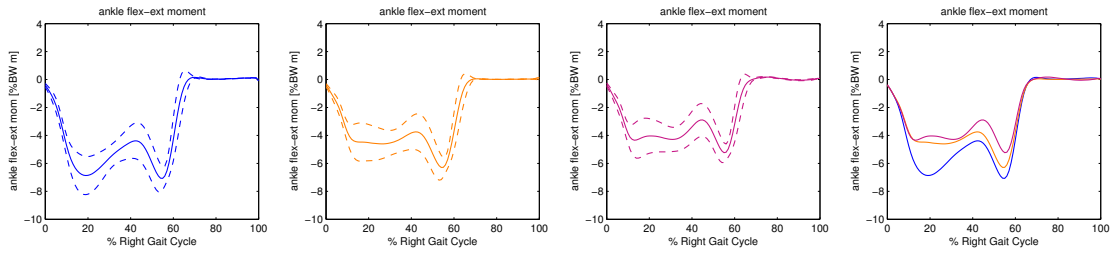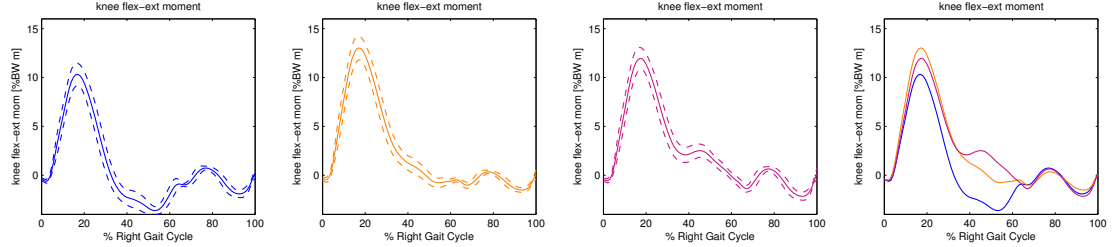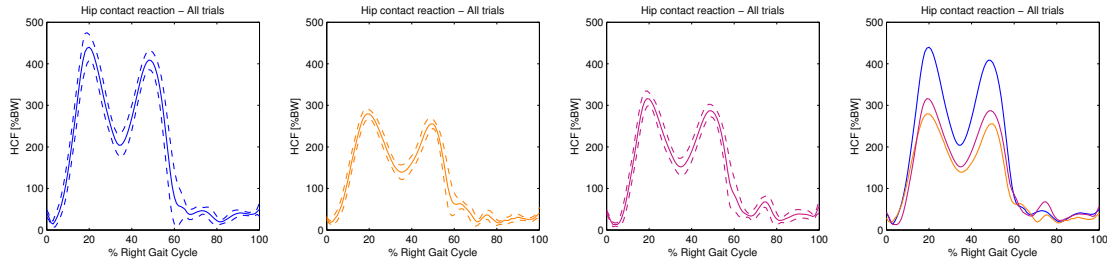
Figure 5.28: Average hip contact forces resultant through the gait cycle with relative standard deviations. On each column is shown the resultant obtained using one of the three models under study: gait2392, LLLM, LLLM2
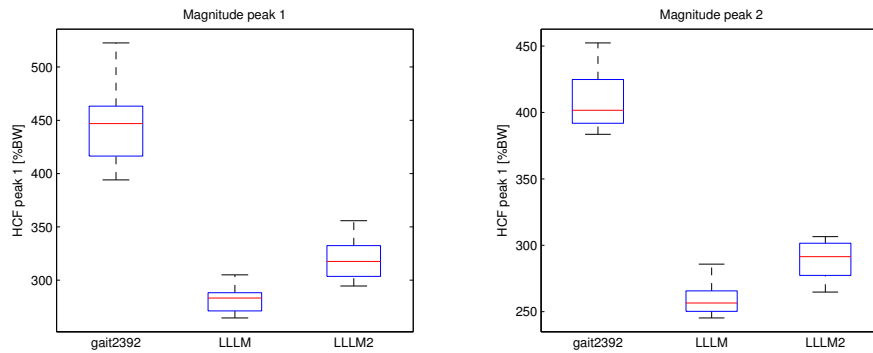
Figure 5.29: Boxplots showing the distribution of the magnitudes of predicted HCF (with gait2392, LLLM and LLLM2 models) at the two main peak instants.
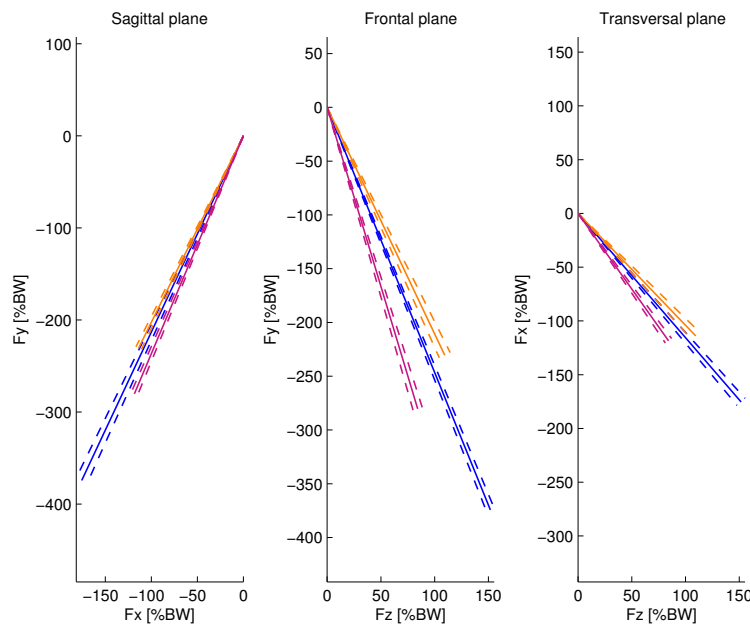
Figure 5.30: Average orientation (± standard deviation in dashed line) and magnitude of the components of HCF in the sagittal, frontal and transversal plane at the first peak. Computed using gait2392, LLLM, LLLM2. Positive orientations of X,Y and Z components correspond respectively to posterior-anterior, distal-proximal and medio-lateral direction.
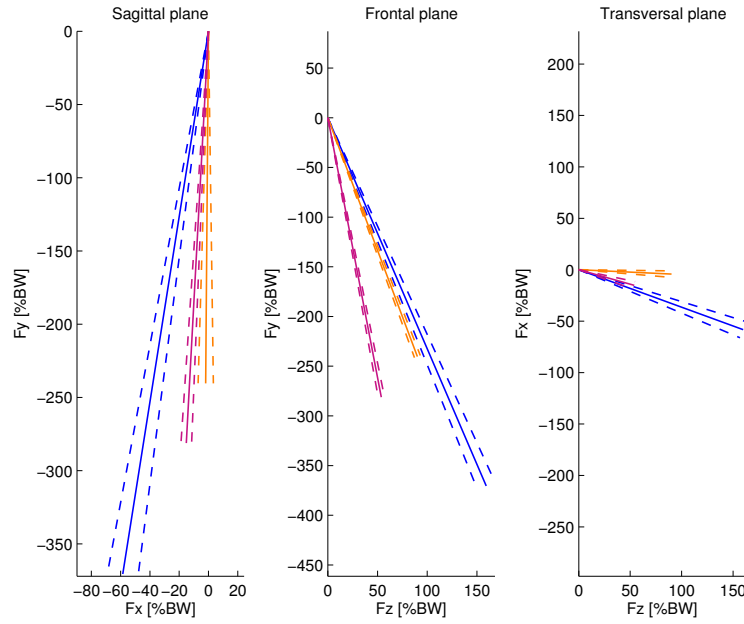
Figure 5.31: Average orientation (± standard deviation in dashed line) and magnitude of the components of HCF in the sagittal, frontal and transversal plane at the second peak. Computed using gait2392, LLLM, LLLM2. Positive orientations of X,Y and Z components correspond respectively to posterior-anterior, distal-proximal and medio-lateral direction.

Static Optimization results

Being available the EMG signals recorded during the stair climbing trials of subject SM7, it is possible for this subject to compare EMGs (normalized by the highest value extracted from maximum voluntary contraction tasks) with muscle bundles activation, output of OpenSim Static Optimization tool, computed as the predicted muscle force divided by the maximum isometric force. In Figures 5.32 and 5.33 are reported, as an example, predicted muscle activation plotted against EMG respectively from the second and the seventh stair climbing trial. It must be brought to attention that, being the quality of EMG recordings of the *rectus femoris*, *tensor fascia latae* and *soleus* poor are shown without reference EMG signal. In order to measure the similarity between EMG and each model's muscle activation prediction, their cross-correlation was computed (Table 5.4) but aforementioned muscles – of which it was impossible to retrieve reference EMGs of stair climbing trials– were not included. For muscles represented with multiple bundles, the overall muscle activation to be correlated with the EMG was computed as the sum of bundles activations.

(a) Rectus femoris*

(b) Vastus lateralis

(c) Vastus medialis

(d) Semitendinosus

(e) Biceps femoris long head

(f) Tensor fascia latae*

(g) Gastrocnemius medialis

(h) Gastrocnemius lateralis

(i) Soleus*

(j) Tibialis anterior

Figure 5.32: EMG signals (shaded gray area) against gait2392, LLLM, LLLM2 predicted muscle bundles activations for **walking trial 2**.

Table 5.4: Mean cross-correlation (between EMG and muscle activation predicted with each of the three models) $\pm$ standard deviation computed over 10 trials.

Cross correlation R	gait2392	LLLM	LLLM2
$R_{\text{Vastus lateralis}}$	0,52 $\pm$ 0,15	0.58 $\pm$ 0.13	0.54 $\pm$ 0.06
$R_{\text{Vastus medialis}}$	0.84 $\pm$ 0.04	0.93 $\pm$ 0.01	0.89 $\pm$ 0.14
$R_{\text{Semitendinosus}}$	0.42 $\pm$ 0.1	0.59 $\pm$ 0.06	0.38 $\pm$ 0.05
$R_{\text{Biceps femoris}}$	0.34 $\pm$ 0.04	0.66 $\pm$ 0.04	0.57 $\pm$ 0.09
$R_{\text{Gastrocnemius medialis}}$	0.81 $\pm$ 0.06	0.77 $\pm$ 0.07	0.77 $\pm$ 0.04
$R_{\text{Gastrocnemius lateralis}}$	0.68 $\pm$ 0.06	0.91 $\pm$ 0.02	0.89 $\pm$ 0.07
$R_{\text{Tibialis anterior}}$	0.52 $\pm$ 0.08	0.57 $\pm$ 0.07	0.70 $\pm$ 0.09
mean(R):	(0.59)	(0.72)	(0.68)

(a) Rectus femoris*

(b) Vastus lateralis

(c) Vastus medialis

(d) Semitendinosus

(e) Biceps femoris long head

(f) Tensor fascia latae*

(g) Gastrocnemius medialis

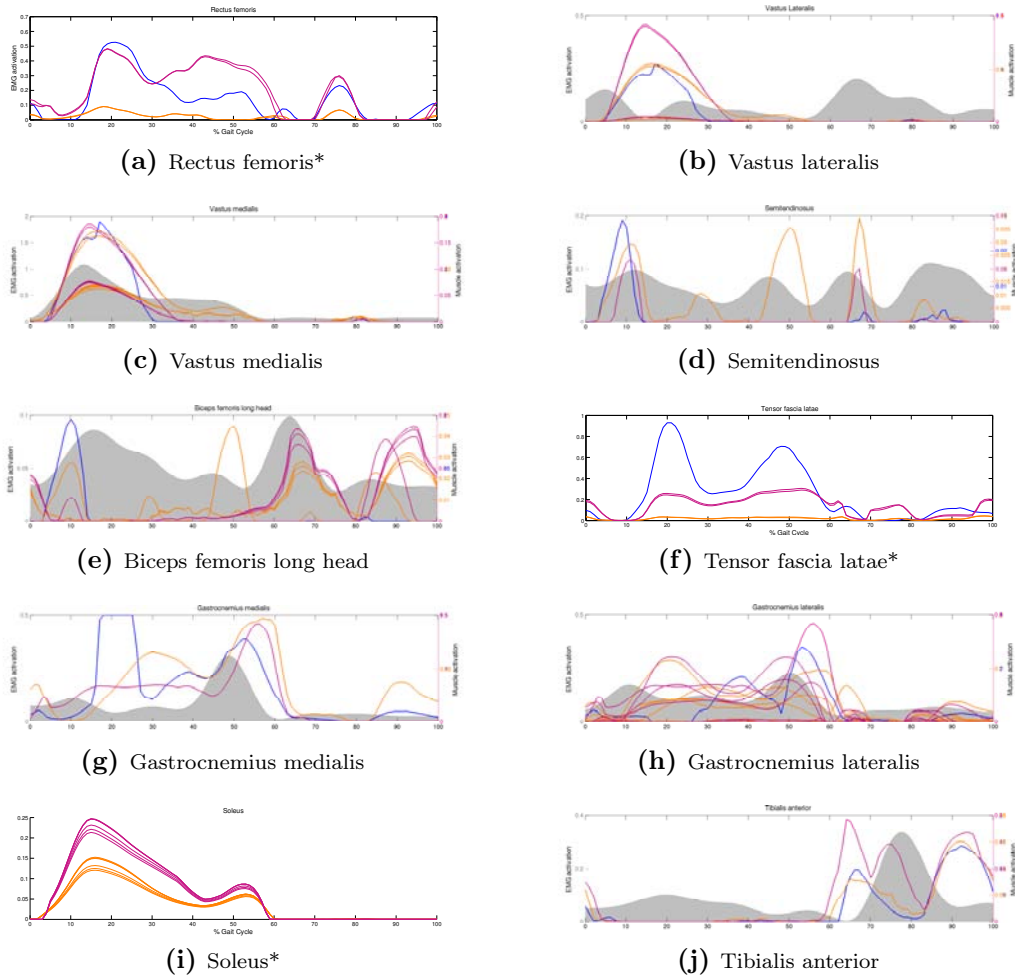**(h)** Gastrocnemius lateralis

(i) Soleus*

(j) Tibialis anterior
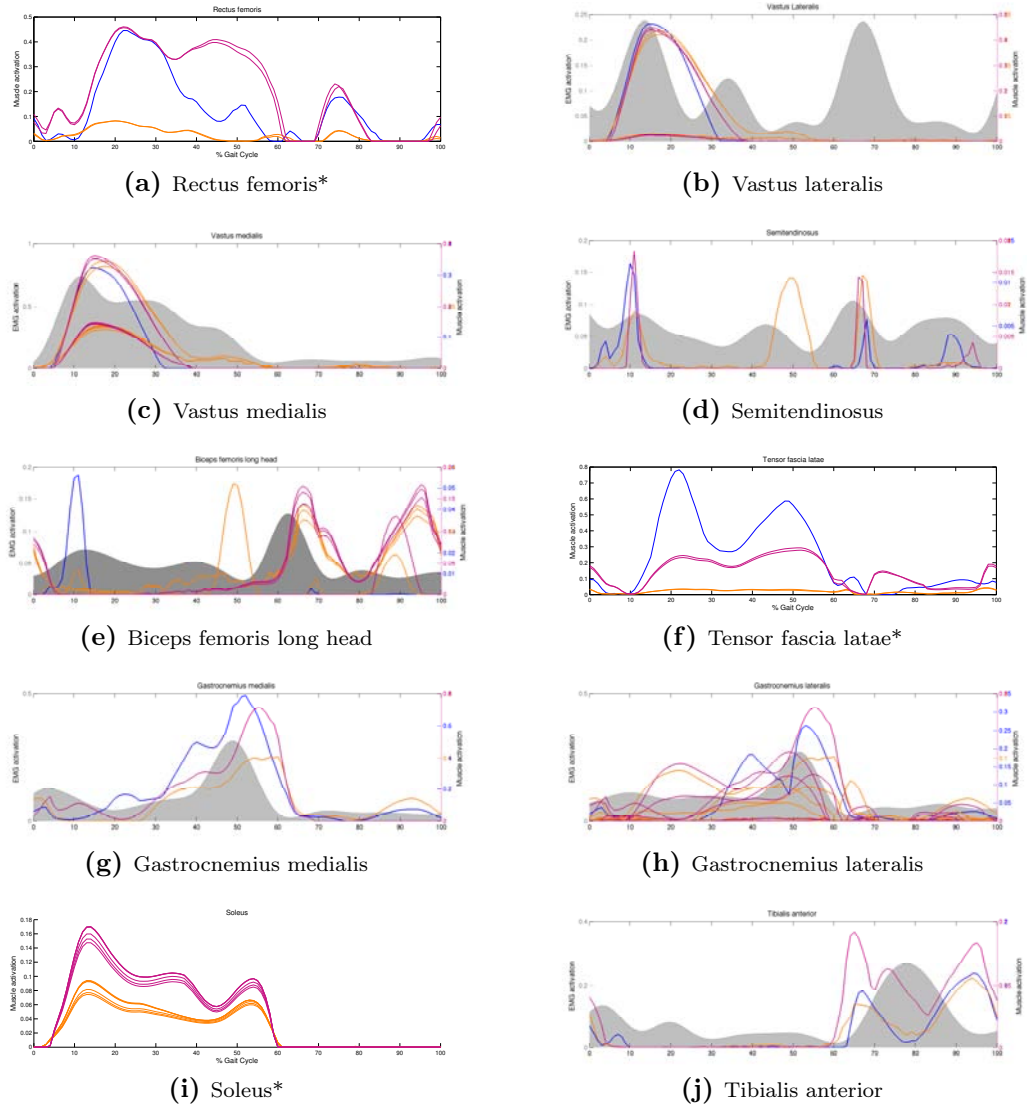
Figure 5.33: EMG signals (shaded gray area) against gait2392, LLLM, LLLM2 predicted muscle bundles activations for **walking trial 7**.

5.4   Discussion

Also for the stair climbing task, considerations needs to be made on the differences in inverse kinematics and inverse dynamics results. As previously stated in Section 4.4, inconsistencies between the models can be due mainly to three factors: the different foot kinematics described by the models, the different definition of segments embedded reference system and finally possible offsets due to different initial pelvic coordinates. All these small discrepancies yielded discrepancies in the resulting joint moments, and in particular at the hip joint (top of the kinematics chain).

In Figures 5.34 it can be observed a higher correspondence, with respect to

the walking trials, between experimental ranges and HCFs predictions averaged over all subjects and all stair trials. Bergmann's data range of values (gray filled area) was extracted from HIP98 dataset by averaging the upper and lower bounds extracted from all subjects' HCFs at stair ascending trials. In Figure 5.35(a) and (b) the boxplots of HCFs magnitudes respectively at the first and second peak are shown. More specifically, it can be observed that, while gait2392 overestimates both peaks magnitudes, LLLM and LLLM2 median peak magnitudes always lie in the experimental ranges.
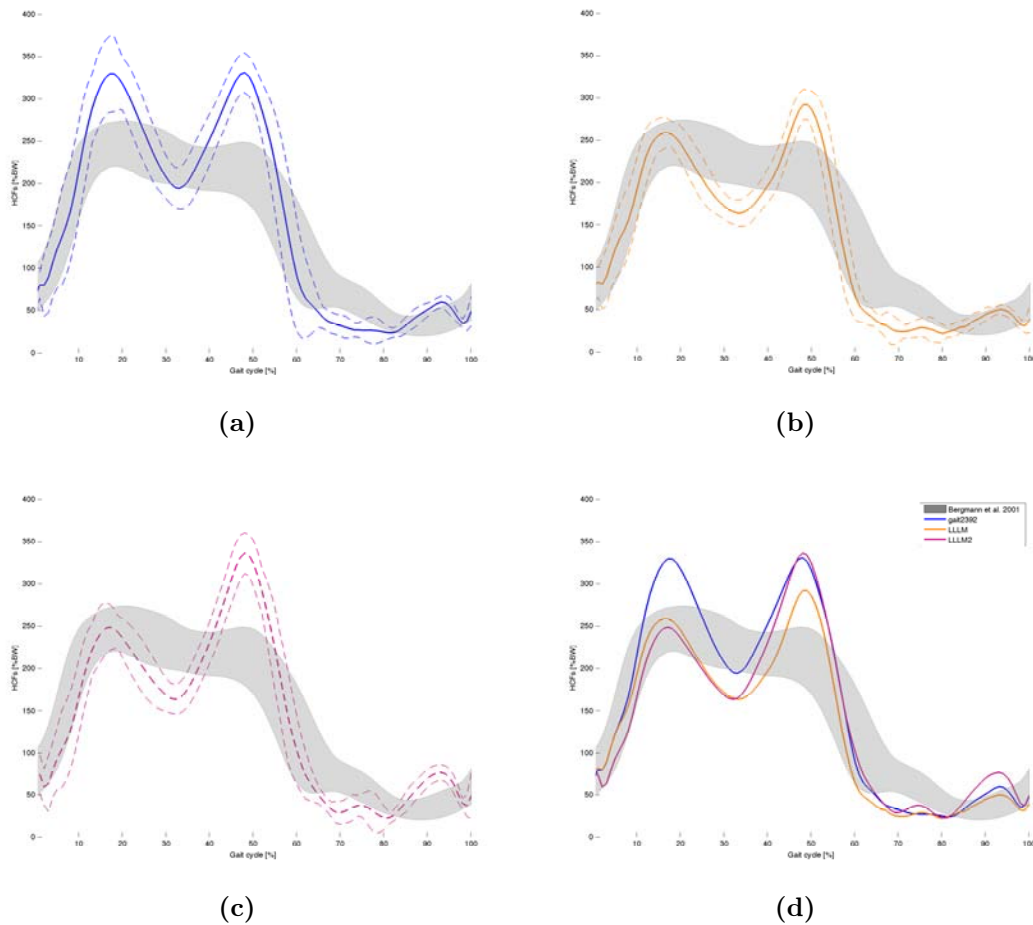
Figure 5.34: Average HCFs magnitudes (solid lines) with relative standard deviations (dashed lines) through the gait cycle predicted using gait2392 (a) LLLM (b), LLLM2 (c) plotted against experimental ranges (gray filled area) from HIP98. In (d) all the mean magnitudes have been plotted together to ease the visual comparison.

To further analyze the peak predictions in comparison with HIP98 dataset, the mean orientations of HCFs at the two peaks were extracted from both the experimental trials and the HCFs obtained using the three models under study. At the first peak (Figure 5.36) the experimental orientation is very close to LLLM2 prediction on the frontal plane, but it results more anteriorly oriented (positive

(a)   (b)

Figure 5.35: Boxplots showing the distribution of the magnitudes of experimental and predicted HCF (with gait2392, LLLM and LLLM2 models) at the first (a) and at the second peak (b).

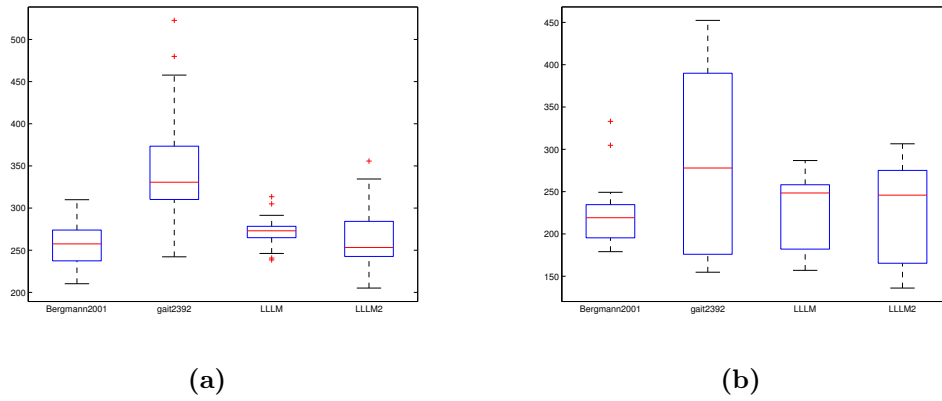direction of X-component) than all the predictions. At the second peak (Figure 5.37) it appears evident that all the models fail to catch the orientation of the experimental medio-lateral component, predicting as laterally oriented both the frontal and transversal components.

To make a numerical comparison between the results of different models, the same indexes introduced in 4.4 were computed also for the HCFs resultants of stairs climbing trials. In this case all the models yielded al almost equivalent RMSE and cross-correlation R, but observing the resulting P1diff and P2diff, it is clear that gait2392 overestimates both peak magnitudes. Between LLLM and LLLM2, by considering also the direction on frontal and transversal plane both at the first and second peak, it can be said that LLLM2 better predicts HCFs in terms of in magnitude and direction when compared to measured values of force.

Table 5.5: Indexes extracted to draw a numerical comparison between gait2392, LLLM and LLLM2.

	gait2392	LLLM	LLLM2
RMSE [%BW]	37.74	36.73	42.80
R	0.97	0.98	0.98
P1diff [%BW]	-66.86	-2.33	1.32
P2diff [%BW]	-47.76	2.24	4.24
P1angdist on frontal pl. [°]	+8	+12	-2
P1angdist on transv pl. [°]	-19	-10	-32
P2angdist on frontal pl. [°]	+26	+28	+16
P2 angdist transv pl. [°]	+105	+122	+106

Concerning the static optimization results of subject SM7 the highest mean

Figure 5.36: Average orientation and magnitude of the components of HCF in the frontal and transversal plane **at the first peak**. Computed using HIP98 dataset(mean±sd), gait2392, LLLM, LLLM2. Positive orientations of X,Y and Z components correspond respectively to posterior-anterior, distal-proximal and medio-lateral direction.

cross-correlation value between EMG recordings and predicted muscle activation is reached by LLLM. In comparing LLLM and LLLM2 static optimization results, it has to be taken into account that the gluteal muscles, that in LLLM2 have been designed in a more physiological way, have not been recorded and therefore have not been included in the results.
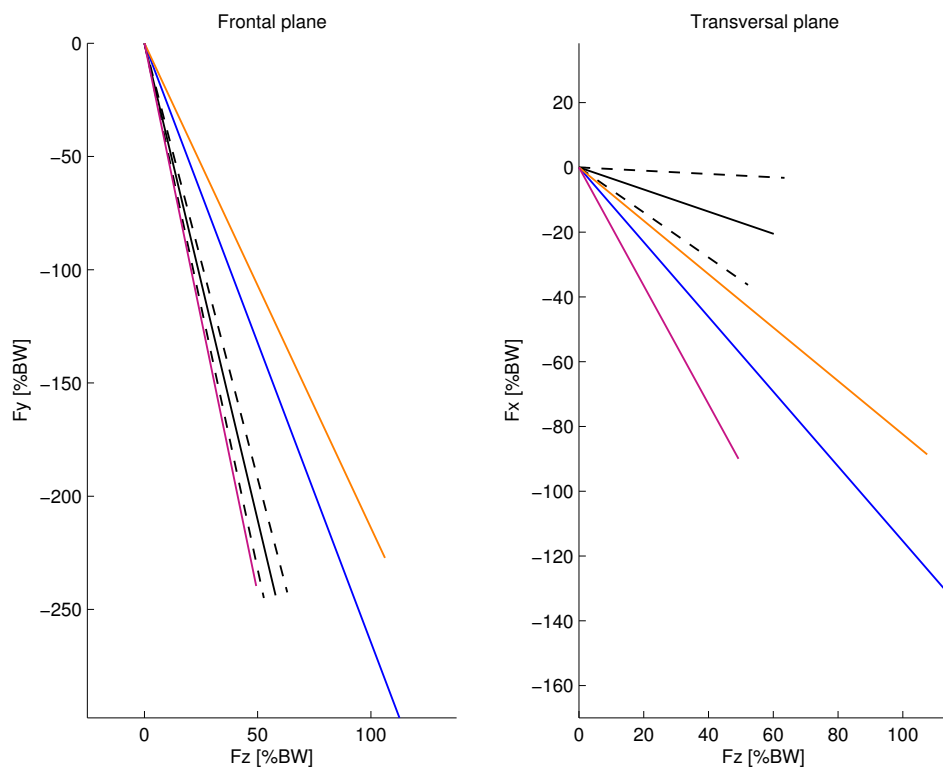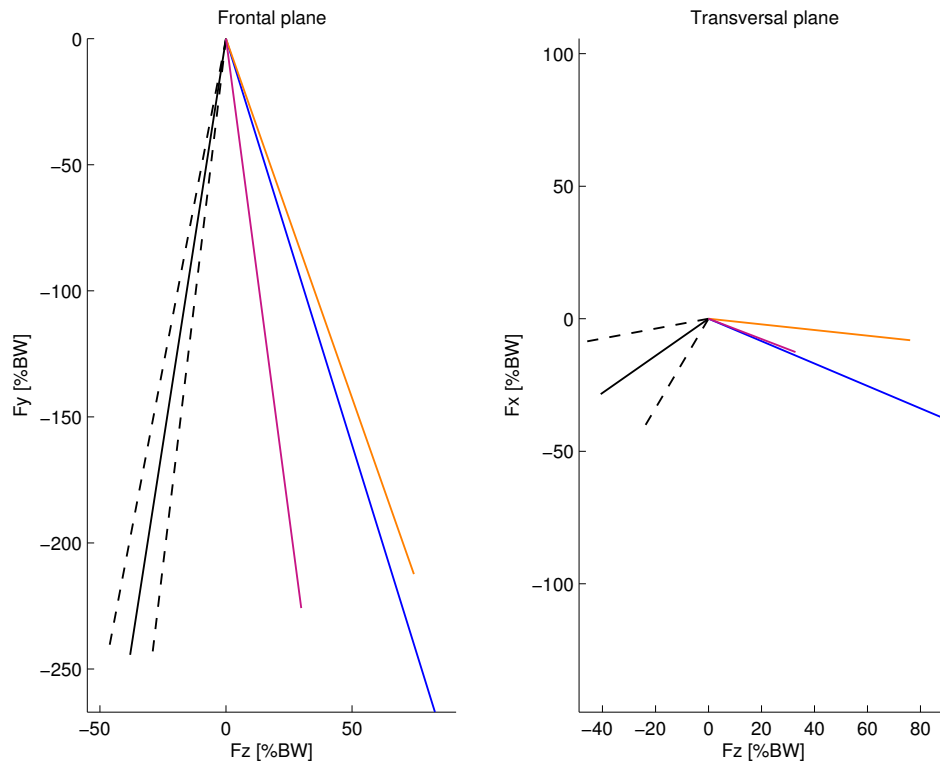
Figure 5.37: Average orientation and magnitude of the components of HCF in the frontal and transversal plane **at the second peak**. Computed using HIP98 dataset(mean±sd), gait2392, LLLM, LLLM2. Positive orientations of X,Y and Z components correspond respectively to posterior-anterior, distal-proximal and medio-lateral direction.

Chapter 6

Conclusions

The aim of this study was to assess the performances of gait2392, LLLM and LLLM2 musculoskeletal models by answering to the research question : which of the three models better predicts muscle activations and hip contact forces?

With these purposes, dynamic simulations of walking and stair climbing trials of one subject (SM7) were run to make a qualitative comparison between predicted muscle activations and collected electromyographic signals. For both daily living activities LLLM musculoskeletal model resulted ad the model predicting the muscle activations that best correlate with recorded EMG signals, even though it should be highlighted that few but important muscles such as muscles from the gluteal complex and adductors were not included in the assessment.

Regarding the hip contact forces predictions, HCF predicted using the three models under study through dynamic simulations of walking and stair climbing trials of three subjects, have been compared with experimental data from HIP98 dataset in terms of magnitude and orientation. Results show that both LLLM2 and gait2392 for the walking simulations predict totally unrealistic magnitudes at the second peak (push-off), therefore, to predict general HCFs (without any distinction between activities to be simulated), LLLM is the most reliable among those under study.

Limitations of this study include: the discussed discrepancies between joint resulting angles due to model offsets and different segment reference systems and the incomplete (and sometimes not accurate) set of EMG recordings needed for the qualitative validation. It is also to be noted that HIP98 dataset used as a reference is referred to old patients with instrumented prostheses while SF1, SM4 and SM7, subject whose gait/stair ascent was simulated, were young and healthy subject.

Further work will be necessary to enhance the accuracy of these models in the prediction of hip joint contact forces by improving, for example, factors previously

cited as limitations. Future developments will go towards the analysis of other daily activities such as sit to stand and towards the application to finite element models implementing bone remodelling algorithms. A truly reliable musculoskeletal model is necessary when thinking of clinical and surgical applications and for the study and treatment of bone structure pathologies.

Bibliography

[Alonso,2004] Alonso, F. J., Del Castillo, J.M., Pintado, P., *An automatic filtering procedure for processing biomechanical kinematic signals*, Lecture Notes in Computer Science, 3337, pp. 281-291, 2004.

[Anderson,1999] Anderson F.C., Pandy M.G., *A dynamic optimization solution for vertical jumping in three dimensions.*,Computer Methods in Biomechanics and Biomedical Engineering 2:201-231, 1999

[Anderson and Pandy,1999] Anderson, F. C.,Pandy, M. G., *A Dynamic Optimization Solution for Vertical Jumping in Three Dimensions*, Computer Methods Biomechanics and Biomedical Engineering, 2, 201-23,1999.

[Barre,2014] Barre, A., Armand, S., *Biomechanical ToolKit: Open-source framework to visualize and process biomechanical data*, Computer Methods and Programs in Biomedicine, 114 (2014),pp. 80–87.

[Bergmann,2001] Bergmann, G., Deuretzbacher, G., Heller, M., Graichen, F., Rohlmann, A., Struss, J., Duda, G.N., *Hip contact forces and gait patterns from routine activities*, Journal of Biomechanics 34 (2001), 859-871.

[Buchanan,2004] Buchanan, T.S., Lloyd, D.G., Manal, K., and Besier, T. F., *Neuromusculoskeletal Modeling: Estimation of Muscle Forces and Joint Moments and Movements From Measurements of Neural Command*, J Appl Biomech. 2004 November ; 20(4): 367–395.

[Carhart,2000] Carhart, M. R., *Biomechanical Analysis of Compensatory Stepping: Implications for Paraplegics Standing Via FNS*, Ph.D Dissertation, Arizona State University, 2000.

[Crowninshield,1981] Crowninshield, R.D., Brand, R.A, *?A physiologically based criterion of muscle force prediction in locomotion*, Journal of Biomechanics, Vol.34, No. 11, pp. 793-801, 1981.

[Delp,1990] Delp, S. L., Loan, J. P. , Hoy, M. G., Zajac, F. E., Topp, E. L. and Rosen, J. M., *An interactive graphics-based model of the lower extremity to study orthopaedic surgical procedures*, IEEE Trans. Biomed. Eng. 37:757–767, 1990.

[Delp,1995] Delp, S.L., Loan, J.P., *A graphics-based software system to develop and analyze models of musculoskeletal structures*, Comput. Biol. Med., vol. 25, pp. 21–34, 1995.

[Delp,2007] Delp, S.L., Anderson, F.C., Arnold, A.S., Loan, P., Habib, A., John, C.T., Guendelman, E., and Thelen, D.G., *OpenSim: Open-Source Software to Create and Analyze Dynamic Simulations of Movement*, IEEE transactions on biomedical engineering, Vol. 54, No. 11, November 2007.

[Dempster,1955] Dempster, W. T., *Space requirements of the seated operator*, Wright-Patterson Air Force Base. Dayton, OH,1955.

[Dumas,2007] Dumas, R., Cheze, L., Verriest, J.P., *Adjustments to McConville et al. and Young et al. body segment inertial parameters*, Journal of Biomechanics 40 (2007) 543–553.

[Friederich,1990] Friederich, J.A. and Brand, R.A., *Muscle fiber architecture in the human lower limb*, J. Biomech., vol. 23, pp. 91-95, 1990.

[Golyandina,2001] Golyandina, N., Nekrutkin, V., Zhigljavsky, A.A., *Analysis of time series structure: SSA and related techniques*, Chapman&hall/CRC, 2001

[Grood,1983] Grood, E.S., Suntay, W.J., *A joint coordinate system for the clinical description of three-dimensional motions: application to the knee.*Journal of Biomechanical Engineering 105, 136–144, 1983.

[Hermens,1999] Hermens, H.J., Freriks, B., Merletti, R., H´agg, G., Stegeman, D., Blok, J. , et al., *SENIAM 8: European recommendations for surface electromyography*, ISBN: 90-75452-15-2, Roessingh Research and Development.

[Inman,1976] Inman, V.T., *The Joints of the Ankle*, Baltimore, Williams & Wilkins, 1976.

[Klein Horsman,2007] Klein Horsman, M. D., Koopman, H. F., van der Helm, F. C., Prose, L. P. and Veeger, H. E., *Morphological muscle and joint parameters for musculoskeletal modelling of the lower extremity*, Clinical Biomechanics 22, 239-247,2007.

[LLoyd,2003] Lloyd, D.G., Besier, T.F. *An EMG-driven musculoskeletal model to estimate muscle forces and knee joint moments in vivo*, Journal of Biomechanics 36 (2003), 765–776.

[Lu,1999] Lu, T.W., O Connor, J.J, *Bone position estimation from skin marker co-ordinates using global optimisation with joint constraints* Journal of Biomechanics 32 (1999),129—134.

[Lund,2012] Lund, M. E., de Zee, M., Andersen, M. S., and Rasmussen, J., *On validation of multibody musculoskeletal models*,Journa of Engineering in Medicine 226(2), 82–94, 2012.

[Modenese,2011] Modenese L., Phillips, A.T.M, Bull, A.M.J., *An open source lower limb model: Hip joint validation*, Journal of Biomechanics 44 (2011) 2185–2193

[Modenese,2013] Modenese, L., *Hip contact force prediction using a musculoskeletal model of the lower limb*, IImperial College London, London, 2013.

[Perry,1992] Perry,J., Burnfield, J.M., *Gait analysis : normal and pathological function*, Thorofare, NJ: Slack, 1992.

[Phillips,2012] Phillips, A. T. M., *Structural Optimisation: Biomechanics of the Femur*, Proceedings of the ICE - Engineering and Computational Mechanics 165, 147–154, 2012.

[Phillips,2015] Phillips, A.T.M, Villette, C.C., Modenese, L. *Femoral Bone Mesoscale Structural Architecture Prediction using Musculoskeletal and Finite Element Modelling*, International Biomechanics, http://www.tandfonline.com/10.1080/23335432.2015.1017609, 2015.

[Rasmussen,2001] Rasmussen, J., Damsgaard, M., Voigt, M., *Muscle recruitment by the min/max criterion: a comparative numerical study*, Journal of Biomechanics 34 (2001), pp. 409–415.

[Van del Helm,1991] Van der Helm, F. C. and Veenbaas, R., *Modelling the mechanical effect of muscles with large attachment sites: application to the shoulder mechanism*, Journal of Biomechanics 24, 1151-1163, 1991.

[Viceconti,2008] Viceconti, M., Clapworthy, G. and Van Sint Jan, S., *The Virtual Physiological Human - a European initiative for in silico human modelling*, The Journal of Physiological Sciences 58, 441-446, 2008.

[Wesseling,2014] Wesseling, M., Derikx, L. C.,de Groote, F., Bartels, W., Meyer, C., Verdonschot, N., Jonkers, I., *Muscle Optimization Techniques Impact the Magnitude of Calculated Hip Joint Contact Forces*,Wiley Online Library (wileyonlinelibrary.com). DOI 10.1002/jor.22769.

[Wickiewicz,1983] Wickiewicz, T. L., Roy, R. R., Powell, P. L., and Edgerton, V. R., *Muscle architectuie of the human lower limb* Clin. Orthop. Rei. Res., vol. 179, pp. 275-283, 1983.

[Winter,1974] Winter, D.A., Sidwall, H.G., Hobson, D. A., *Measurement and reduction of noise in kinematics of locomotion*, Journal of Biomechanics, vol. 7, Issue 2, pp. 157-159,1974.

[Wu,1995] Wu, G. and Cavanagh, P.R., *ISB recommendations for standardization in the reporting of kinematic data*, Journal of Biomechanics, Vol. 28, No. 10, pp. 1257-1261, 1995

[Wu,2002] Wu, G., Siegler, S., Allard, P., Kirtley, C., Leardini, A., Rosenbaum, D., Whittle, M., D'Lima, D. D., Cristofolini, L., Witte, H., Schmid, O., Stokes, I., *ISB recommendation on definitions of joint coordinate system of various joints for the reporting of human joint motion—part I: ankle, hip, and spine*, Journal of Biomechanics 35 (2002), pp. 543-548.

[Yamaguchi,1989] Yamaguchi, G. T. and Zajac, F. E., 1989. A planar model of the knee joint to characterize the knee extensor mechanism. Journal of Biomechanics 22, 1-10.